曲痕折纸的弹性能量响应

Elastic Energy Behaviours of Curved-crease Origami

一级学科：机械工程

学科专业：机械工程

作者姓名：李庭玮

指导教师：陈焱　教授

天津大学机械工程学院

二〇二〇年七月

摘 要

折纸是一门中国的传统艺术，其能够将平面材料通过折叠转换成三维结构。曲线折痕折纸是一种特殊类型的折纸，其使用曲线折痕图案通过非刚性折叠使平面材料具有不同的三维结构。近年来，由于其特殊的结构以及力学性能，曲痕折纸在工程和建筑领域中也有广泛的应用。本文通过考虑材料弹性弯曲能量响应和折纸可展性约束之间的相互作用，得到了一系列曲痕折纸图案，并且系统性的研究了弹性弯曲曲痕折纸的设计和应用。

首先，本文通过将大弹性弯曲变形的一维弹性曲线引入曲痕折纸的镜像生成过程中，提出了一种曲痕折纸曲面的精确描述方法，即曲痕折纸的弹性曲面生成法。通过该方法得到了一种被称为弹性曲面折纸的新的几何结构，它能够精确地描述弹性弯曲曲面折纸的主要表面曲率和可展性（即可以展开成一个平面）特征。为了证明这一点，我们对实物模型进行了三维扫描和表面误差分析，结果表明理论解与实物模型（厚度为2 mm）之间的表面误差小于实物模型厚度的50%。此外，本文也对这种设计曲痕折纸的方法的局限性进行了探究，比如最大压缩系数的推导问题、折展运动数值模拟精度的研究等。

其次，本文根据曲痕折纸的几何参数，通过折纸结构局部截面的力学特性得到其整体的力学特性，提出了一种新的方法，能够在曲痕折纸柔顺机构中得到可编程的力-位移响应。只有当折纸图案的局部横截面不受折痕影响时，上述转化才能实现，根据这一特点，我们可以通过改变折纸结构的几何参数，得到其不同的力-位移响应。

最后，通过预先嵌入折痕的方式，本文提出了一种控制薄壁管状结构弹性屈曲形状的新方法，这也是曲痕折纸的一种新的应用。该方法将薄壁结构的失效模式预设为和直圆管的钻石失效模式相类似的形式。通过对一系列实物模型的实验，我们证明了可以通过添加曲线折痕，将薄壁结构的失效形式引导至预设的模式。经过测量，实物模型的表面变形与理论解十分接近。本文还对屈曲过程的驱动机理进行了研究，并且发现通过嵌入可控曲痕折纸可以得到具有双稳态的薄壁管状结构。

综上所述，本文为折纸工程领域的研究做出了突出贡献，深入研究了曲痕折纸的几何关系和潜在工程应用。

关键词： 弹性曲线理论，曲痕折纸，柔顺机构，弹性弯曲应变能，屈曲形状控制，薄壁圆管

ABSTRACT

This thesis systematically explored the design and utilisation of elastically-bent curved-crease origami. This was achieved by developing a set of curved-crease patterns with consideration of the interaction between material elastic bending energy behaviours and origami developability constraints. The thesis makes the following contributions.

First, an exact analytical surface representation of a curved-crease pattern was developed by introducing the 1D elastica solution for large elastic bending deformation into the mirror reflection curved-crease origami generation process. The new geometry, deemed elastica surface origami, is capable of concisely and accurately capturing the principal surface curvature and developability characteristics of elastically-bent curved-crease origami. A surface error analysis of 3D scanned physical prototypes was used to validate the analytical geometries, which were shown to be highly accurate to within 50% of the 2mm sheet thickness for a range of elastica surface profiles. Limitations of the curved-crease generation method were also explored including the derivation of a maximum compressibility limit; investigation of accuracy of numerical folding motion simulation; and an investigation of a free edge distortion behaviour which occurred in certain origami forms.

Second, an elastica-derived bending strain energy formulation was used to generate a customizable force-displacement response in curved-crease compliant mechanisms. This new method was presented by translating the local cross section deployment mechanics to a global frame of reference set according to the design parameters of the curved-crease origami unit geometry. A valid local-global translation and force-displacement response was found when the cross section deformations with and without developability constraints were suitably close to each other. This key feature enabled a range of predictable non-linear force-displacement responses to be realised through the alternation of pattern edge angle, edge length, and tessellated forms.

Third, a new application of curved-crease origami was developed for control over the shape of an elastically-buckled thin-walled cylinder, using pre-embedded crease lines. The failure mode was pre-determined as a stabilised high-order elastica surface, which manifests via a diamond buckling mode, similar to imprecise failure modes known to occur in cylinders of this type. A set of prototypes were tested and showed that the buckling process can be guided to a range of designed failure modes. The deformed surface was measured and shown to have a near-exact correspondence to the analytical geometric description. Finally, the investigation into the driving mechanics of the buckling process was closely explored. It was found that the controllable buckling process exhibited a bistable transition from a higher strain energy tubular state to a lower strain energy curved-crease state.

Overall, this thesis has made a significant contribution to the research field of origami

engineering and large deformation non-linear mechanics. It offers a strong research platform for curved-crease origami ranging from the fundamental geometrical relations to potential engineering applications.

KEY WORDS: Elastica, curved-crease origami, compliant mechanism, elastic bending strain energy, buckling shape control, thin-walled cylinder

Contents

摘 要 · · · · · I

ABSTRACT · · · · · I

Contents · · · · · V

List of Figures · · · · · IX

List of Tables · · · · · XIII

List of Symbols and Abbreviations · · · · · XV

Chapter 1 Introduction · · · · · 1

1.1 Background · · · · · 1

1.2 Aim and Scope · · · · · 2

1.3 Layout · · · · · 2

Chapter 2 Literature Review · · · · · 5

2.1 Origami Geometry · · · · · 5

2.1.1 Origami-inspired Structures · · · · · 5

2.1.2 Origami Patterns · · · · · 5

2.1.3 Developable Surfaces · · · · · 9

2.2 Modelling of Curved-crease Origami · · · · · 12

2.2.1 Geometric Methods for Folded Forms · · · · · 13

2.2.2 Numerical Methods for Folded Forms · · · · · 15

2.2.3 Numerical Folding Simulations · · · · · 17

2.3 Large Elastic Bending · · · · · 19

2.3.1 Elastica Curves · · · · · 19

2.3.2 Modelling Tools for Elastica Curves · · · · · 22

2.4 Summary · · · · · 22

Chapter 3 Modelling of Curved-crease Origami using Elastica Curves · · · · · 25

3.1 Curved-crease Origami Creation · · · · · 25

3.1.1 Elastica Curves and Non-zero Principal Curvature of a 3D Surface 25

3.1.2 Geometry Construction Method · · · · · 27

3.1.3 Contact Limit State · · · · · 28

3.2 Experimental Analysis · · · · · 29

3.2.1 Method · · · · · 29

3.2.2 Single-crease Reflection · · · · · 32

3.2.3 Constructed State · · · · · 35

3.2.4 Surface Tessellation · · · 36
3.3 Combined Numerical-elastica Formulations · · · 37
3.3.1 Folding Sequence · · · 37
3.3.2 Free Edge Effect · · · 39
3.4 Limitation of the Proposed Modelling Method · · · 43
3.4.1 Motivation · · · 43
3.4.2 Elastica Surface with Non-uniform Bending Stiffness · · · 44
3.4.3 Non-localised Free Edge Effect · · · 46
3.5 Conclusion · · · 49
Chapter 4 Curved-crease Origami Folding Mechanics · · · 55
4.1 Folding Mechanics of Curved-crease Origami · · · 55
4.1.1 Elastic Bending Strain Energy of a Beam · · · 55
4.1.2 Comparison of Lower and Upper Bound Energy Behaviours · · · 57
4.1.3 Elastica Surface Curved-crease Origami · · · 58
4.1.4 Experimental Validation of Energy Behaviours · · · 60
4.1.5 Further Details of PRBM Calculation · · · 62
4.1.6 Comparison of Cross Section Profiles · · · 63
4.2 Parametric Investigation of Force-displacement Responses · · · 67
4.2.1 Translation of Local Deployment Mechanics · · · 67
4.2.2 Edge Angle Effect · · · 70
4.2.3 Edge Length Effect · · · 70
4.2.4 Modular Tessellation · · · 70
4.3 Customizable Force-displacement Responses · · · 72
4.4 Conclusion · · · 73
Chapter 5 Curved-crease Origami Applications in Elastic Buckling of Tubes · · · 77
5.1 Introduction · · · 77
5.1.1 Motivation · · · 77
5.1.2 Tubular Buckling and Origami Tubes · · · 77
5.2 Geometric Design · · · 79
5.2.1 Target State Curved-crease Origami Creation · · · 79
5.2.2 Transformation of Curved to Straight-crease Diamond Pattern · · · 81
5.3 Experimental Analysis · · · 82
5.3.1 Method · · · 82
5.3.2 Buckling Modes and Force-displacement Responses · · · 82
5.3.3 Deformed Surface Analysis · · · 85
5.4 Behaviour Analysis · · · 86
5.4.1 Elastic Bending Energy of Deformed and Undeformed States · · · 86
5.4.2 Lobe Transition Characterisation · · · 88

5.4.3 Lobe Transitional Energy Behaviour · · · 89
5.4.4 Limitation in Numerical Modelling · · · 91
5.5 Conclusion · · · 92
Chapter 6 Conclusion · · · 93
6.1 Summary of Findings · · · 93
6.1.1 Modelling of Curved-crease Origami using Elastica Curves · · · 93
6.1.2 Curved-crease Origami Folding Mechanics · · · 94
6.1.3 Curved-crease Origami Applications in Elastic Buckling of Tubes · 94
6.2 Summary of Contributions · · · 95
6.3 Potential Applications · · · 95
6.4 Future Work · · · 96
References · · · 99
中文大摘要 · · · 117
Publications during Candidature · · · 123
Acknowledgements · · · 125

List of Figures

Fig. 1-1 Curved-crease origami applications 2

Fig. 2-1 Origami-inspired structures 6
Fig. 2-2 Origami patterns and their design components 7
Fig. 2-3 4-degree patterns and their folded forms 8
Fig. 2-4 6-degree patterns and their tubular folded forms 9
Fig. 2-5 Types of curved-fold 9
Fig. 2-6 Principal curvatures of a smooth surface 10
Fig. 2-7 Gaussian curvature of smooth surfaces 11
Fig. 2-8 Generation of fundamental types of developable surface 11
Fig. 2-9 Assembly of smooth developable surfaces sharing a common developability constraint 12
Fig. 2-10 Curved-crease surfaces assembled from fundamental developable surfaces 13
Fig. 2-11 Curved-crease origami creation using the mirror reflection method . . . 14
Fig. 2-12 Curved-crease origami creation from base rigid-foldable patterns . . . 15
Fig. 2-13 Folding simulation of a rigid-foldable curved-crease Miura pattern . . . 17
Fig. 2-14 Curved-crease origami folding simulation using PRBM 19
Fig. 2-15 Elastica curves for different boundary constraint conditions 20
Fig. 2-16 Elastica curves for a simply-support slender beam with uniform bending stiffness 20
Fig. 2-17 Modelling tools for elastica curves 22

Fig. 3-1 Creation of elastica surface curvature 26
Fig. 3-2 Parametrizations of curved-crease geometries 27
Fig. 3-3 Geometry construction procedures for target folded curved-crease origami 29
Fig. 3-4 Curved-crease origami creation from freeform straight-crease origami base patterns 30
Fig. 3-5 Definition of contact limit state 31
Fig. 3-6 Curved-crease contact limit state 31
Fig. 3-7 Experimental analysis method 33
Fig. 3-8 Surface error measurement of a simple deformed sheet 34
Fig. 3-9 Surface error measurement of single-crease reflection 34
Fig. 3-10 Surface error measurement of constructed state geometries 35
Fig. 3-11 Constructed state surface error measurement results 36

Fig. 3-12 Design procedures of a curved-crease Arc pattern generated with a second-mode elastica curve . . . 37
Fig. 3-13 Surface error measurement of second-mode elastica surface . . . 37
Fig. 3-14 Numerical simulation of folding sequence of elastica generated surface 39
Fig. 3-15 Surface error measurement of numerical folding simulation . . . 40
Fig. 3-16 Folded state surface error measurement results . . . 41
Fig. 3-17 Surface geometry with skewed free edges . . . 41
Fig. 3-18 Surface error measurement between elastica generated surface and physical prototype with skewed edges . . . 42
Fig. 3-19 FE simulation method for a skewed shell . . . 43
Fig. 3-20 Surface error measurement between finite element simulation and physical prototype with skewed edges . . . 44
Fig. 3-21 Curved-crease Arc-Miura pattern geometry with skewed free edges . . 45
Fig. 3-22 Surface error measurement of single-crease reflection free edge effect . 45
Fig. 3-23 FE simulation of curved-crease origami . . . 46
Fig. 3-24 Bending deformations of Type 1 and Type 2 strip . . . 47
Fig. 3-25 Simulation result of numerical-elastica . . . 48
Fig. 3-26 Surface error measurement of Type 1 and Type 2 shell . . . 49
Fig. 3-27 Design procedures of curved-crease origami using Type 1 and 2 elastica curves . . . 50
Fig. 3-28 Surface error measurement Type 1 origami . . . 51
Fig. 3-29 Surface error measurement Type 2 origami . . . 52
Fig. 3-30 Surface error measurement result of Type 1 and Type 2 geometries . . 52
Fig. 3-31 Cross section analysis of Type 1 and 2 origami. . . . 53

Fig. 4-1 Bending behaviour of a simple curved surface with an arc of uniform radius cross section profile . . . 57
Fig. 4-2 Geometric construction of an initial curved-crease origami . . . 58
Fig. 4-3 Upper bound energy behaviour of arc surface origami . . . 59
Fig. 4-4 Energy behaviours of elastica surface origami . . . 60
Fig. 4-5 FE simulation method for the hinge region of curved-crease origami . . 61
Fig. 4-6 Energy behaviour of a physical curved-crease origami during folding motion . . . 62
Fig. 4-7 Material tensile test result of PET . . . 62
Fig. 4-8 PRBM and IPRBM . . . 64
Fig. 4-9 Tangent angle measurement . . . 65
Fig. 4-10 Developability-constrained tangent angle calculation . . . 66
Fig. 4-11 Local-global translation of curved-crease origami mechanics. . . . 67
Fig. 4-12 Experimental analysis of local-global mechanics translation . . . 69
Fig. 4-13 Free edge effect of curved shells . . . 69
Fig. 4-14 Global force-displacement investigation of edge angle effect . . . 71
Fig. 4-15 Global force-displacement investigation of edge length effect . . . 71

Fig. 4-16 Global force-displacement investigation of modular tessellation 72
Fig. 4-17 Customizable force-displacement responses 74

Fig. 5-1 Buckling shape control by using pre-embedded straight-crease diamond pattern 79
Fig. 5-2 Design procedures for tubular curved-crease origami 81
Fig. 5-3 Transformation of curved and straight-crease diamond pattern 82
Fig. 5-4 Buckling mode classification 84
Fig. 5-5 Summary of buckling mode result comparison 84
Fig. 5-6 Target state surface analysis of $m2n5$ pattern 86
Fig. 5-7 Correlation between strain energy, displacement, and buckling modes . 87
Fig. 5-8 Force-displacement comparisons for all curved-crease specimens . . . 89
Fig. 5-9 Constructing surface from DIC data points using MATLAB Curve Fitting Tool 90
Fig. 5-10 Lobe transition behaviour during elastic buckling for CC and SC patterns 91
Fig. 5-11 Illustration of controllable buckling modes 92

List of Tables

Tab. 4-1 Compariosn of energy behaviours of elastica and arc surface origami . 60

Tab. 5-1 Design parameters and buckling mode comparison for patterned cylinders with curved and straight-crease patterns 83

Tab. 5-2 Experimental result of different types of buckling behaviours for curved-crease patterns 88

List of Symbols and Abbreviations

Symbols

a_1	Transverse side length of Arc pattern geometry (short).
a_2	Transverse side length of Arc pattern geometry (long).
b	End opening distance of a curve.
b_1	Incline side length of Arc pattern geometry.
b/L	Curve design parameter.
c_1	Length of the transformation region on Arc pattern geometry (transverse, short).
c_2	Length of the transformation region on Arc pattern geometry (transverse, long).
d_1	Length of the transformation region on Arc pattern geometry (longitudinal).
h	Height of a curve.
h'	Height of a curve during deformation.
h^*	Height of a higher order curve.
k	Position of control vertices of line segments.
k_s	Spring stiffness.
l_D	Target displacement of a patterned cylinder.
l_s	Spring effective length.
m	Quantity parameter used to evaluate elliptic functions.
m, n	Number of longitudinal and circumferential lobes.
s	Position of a given section of the beam along the length.
s_k	Length of line segments.
t	Material thickness.
w	Width of a surface.
w_a	Edge length of a split surface.
w_b	Edge length of a split an inverted surface.
w_k	Length parameter to describe the skewness of the boundary edges.
x, y	Cartesian coordinate system for 2D curves.
x_k, y_k	Coordinates of Edge curve 1.
z	Position of the fibre of the beam section in thickness.
D	Diameter of a thin-walled cylinder.
D/t	Diameter-to-thickness ratio.
E	Young's modulus.

$E(m)$	Complete elliptic integral of the second kind.
EI	Flexural rigidity value.
F	Value of the two opposing horizontal end forces holding an elastica curve.
H	Global height of an undeformed curved-crease origami.
H'	Global height of a curved-crease origami during folding motion.
I	Second moment of area.
K	Gaussian curvature.
$K(m)$	Complete elliptic integral of the first kind.
L	Length of a curve.
L/D	Length-to-diameter ratio.
M	Bending moment.
S	Number of rigid division.
T_x, T_y, T_z	Number of tessellations in X, Y, and Z direction.
U	Strain energy.
U_1	Strain energy of undeformed lobes.
U_2	Strain energy of deformed lobes.
U_{BEND}	Bending strain energy.
U_{PRBM}	Strain energy obtained form PRBM.
X, Y, Z	Global reference system of curved-crease origami.
α	Slant angle design parameter of straight-crease diamond pattern.
α_d	Dihedral angle at initial state.
α'_d	Dihedral angle during folding motion.
ΔU	Difference between upper and lower energy behaviours.
$\Delta x, \Delta y$	Nodal translations of Edge curve 1.
$\Delta\theta$	Tangent angle difference.
η_A	Primary edge angle of an undeformed curved-crease origami.
η'_A	Edge angle of a curved-crease origami during folding motion.
η_B	Edge angle design parameter at initial state.
η'_B	Edge angle design parameter during folding motion.
η_Z	Secondary edge angle of an undeformed curved-crease origami.
γ_k	Angles between a line segment and the y-axis at the initial state.
$\gamma_k^{'}$	Angles between a line segment and the y-axis at an intermediate folded state.
κ	Plane curvature.
κ'	Plane curvature of a deformed curve.
κ_1, κ_2	Plane curvature in principal directions.
κ_{2D}	Radii of curvature of the crease pattern.
κ_x	Lobes curvatures along horizontal (x) direction.

κ_y	Lobes curvatures along vertical (y) direction.
ν	Poisson's ratio .
ϕ	Sector angle of Arc pattern geometry.
ϕ_k	Lateral sector angle.
ρ	Radii of curvature.
ρ'	Radii of curvature of deformed beam element.
σ	Stress value.
θ	Tangent angle of the curve at a given location.
Θ	Tangent angle of the elastica curve at the initial location.
θ_{MA}	Plane edge angle of tubular curved-crease origami.
θ_{MB}	Plane edge angle design parameter of tubular curved-crease origami.
ε	Strain of a deformed beam element.

Abbreviations

ANA	Analytical
CAD	Computer-aided design
CC	Curved-crease
CCBT	Curved-crease bending translation
DIC	Digital image correlation
DOF	Degree of freedom
EXP	Experimental
FE	Finite element
IPRBM	Interpolated-pseudo-rigid-body-model
PET	Polyethylene terephthalate
PQ	Planar quadrilateral
PRBM	Pseudo-rigid-body-model
SC	Straight-crease

Chapter 1 Introduction

1.1 Background

Curved-crease origami is a class of origami patterns which have a curved fold that imparts a non-zero principal curvature into a thin sheet during a non-rigid folding. They are noted for their striking and beautiful folded forms and as such, they are widely employed as decorative or aesthetic components, including as packaging and sculptures.

A new generation of performative applications is emerging which seeks to adopt the beauty of curved-crease surfaces for novel engineering and architectural applications. These include compliant and lamina-emergent mechanisms [1–3], self-assembling devices [4], energy-absorption components [5, 6], façade and shading components [7–9], folded shell components [10, 11], and deployable and thin-walled structures [12–18]. Some of these applications are demonstrated in Fig. 1-1.

Curved-crease applications have all been enabled by preceding work in mathematics, modelling, and simulation of curved-line folding. However, *modelling* techniques are limited. Recent concise geometric descriptions of curved-crease origami do not account for elastic or plastic bending energy and thus present variations to the precise folded fabrication [9]. Other modelling methods typically require numerical discretisation of a target curved surface to allow developability constraints to be enforced at pattern vertices. The discretised surface can approximate a physical surface through relaxation for minimum bending energy, however such methods are cumbersome and their accuracy is largely unknown. Therefore, the core objective of this thesis is to develop a new analytical modelling method that can concisely and accurately capturing both developability and bending behaviours of a curved-crease origami surface.

Furthermore, curved-crease origami has a great potential to be utilised as a compliant mechanism, as they share many of their key characteristics, including sophisticated folding behaviour and strain energy storage capability [19]. However, *folding behaviours* of curved-crease origami are poorly understood. Existing methods utilises a pseudo-rigid approximation of a curved-crease surface for simulating its folding motion [20, 21], and subsequently incorporate material properties to capture the folding mechanics. These methods simply enforce the rigid-foldability without the consideration of surface minimum bending behaviour, hence their accuracy is largely unknown. Therefore, further investigation is needed to explore the interaction between material bending behaviours and origami developability constraints during folding.

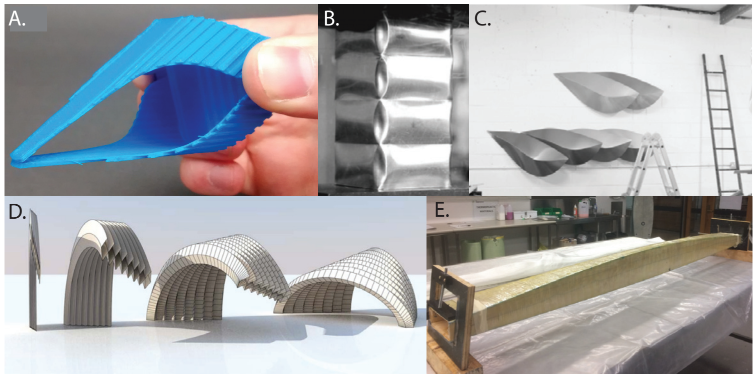

Fig. 1-1 Curved-crease origami applications. (A) Compliant mechanism [3]. (B) Energy-absorption component [6]. (C) Façade component [8]. (D) Deployable structure [13]. (E) Thin-walled structure [18]. Images reproduced with permission.

1.2 Aim and Scope

The aim of the thesis is to propose new curved-crease origami representations with the consideration of material bending behaviours. It will do this by exploring the intersection of curved-crease origami geometries and large elastic bending mechanics, following a central argument that *a 1D elastica solution for large elastic bending deformation can link to a better design solution for curved-crease origami*. The focus of the thesis is on embedding curvature, representing sheet elastic bending behaviours, into the design geometry to give accurate representations of curved-crease origami for different objectives [14, 22]. These include modelling of target folded forms, simulation of folding behaviours, and accurate response of physical phenomenons. This thesis is limited to the consideration of Miura-derivative and Yoshimura-derivative curved-crease patterns, as they are commonly used fundamental origami patterns.

1.3 Layout

The thesis structure consists of five chapters as follows:

- Chapter 2 highlights the significance of the thesis by outlining current knowledge in areas of key relevance. These include a brief overview of origami-inspired engineering, modelling of curved-crease folded forms, and simulation of curved-crease folding behaviours. Furthermore, the theory of *elastica* will also be introduced.
- Chapter 3 utilises a specific type of elastica solution to develop an analytical geometric construction method for curved-crease origami which can concisely and accurately capture the bending behaviours, namely *elastica surface generation of curved-crease origami*. An experimental approach is used for validating the accuracy of analytical geometries. The proposed analytical method is then combined with existing numerical approaches to capture the behaviour of several curved-

crease geometries with different boundary conditions.

- Chapter 4 explores the folding mechanics of curved-crease origami by considering first the minimum elastic bending behaviours of a curved surface, and subsequently considering the interactions between this surface and introduced origami developability constraints. A new *curved-crease bending translation* (CCBT) method to analytically describe the folding mechanics of a curved-crease origami is presented. This enables predictable non-linear force-displacement responses to be realised for curved-crease geometries with different geometric design parameters.
- Chapter 5 presents a new method to control the shape of a elastically buckled medium length thin-walled cylinder by using pre-embedded curved-crease origami patterns. The failure mode is pre-determined as a stabilised high-order elastica surface, which manifests via a diamond buckling mode. A set of prototypes are tested and show that the buckling process can be guided to pre-determined failure modes.
- Conclusions of key findings and discussion on future work are given in the final thesis chapter, Chapter 6.

Chapter 2 Literature Review

This chapter will present a background of previous research work in three areas of key relevance to the thesis scope. First, an overview of origami geometry will be presented. Second, available modelling methods for curved-crease origami will be listed. Finally, the fundamental mechanics of large elastic bending of slender beams will be reviewed.

2.1 Origami Geometry

2.1.1 Origami-inspired Structures

For the past several decades, *origami-inspired structures* have been increasingly studied and adopted across a wide range of scales and disciplines. Scales range from nano-scale DNA [23] to deployable space structures [24]. Disciplines demonstrated to have a high suitability for origami-inspired design include civil engineering [25, 26], biomedical engineering [27–29], aerospace engineering [30, 31], mechanical engineering [32, 33], material science [34, 35], artistic product design [36–38], and architectural design [39, 40].

Origami-inspired structures are popular, as the use of *folding* technique imparts sheet materials with many interesting and useful performance characteristics. These include deployability [41, 42], static load-carrying capability [43–45], and aesthetics. For example, subway maps [46], ballistic barriers [47], and solar arrays [24] can all be efficiently compacted into smaller volumes for storage and transportation, as shown in Fig. 2-1A-C, respectively; folded corrugations can be used to improve the structural stability and stiffness of timber plate structures [48], energy absorption tubes [49], and deployable structures [50], as shown in Fig. 2-1D-F, respectively; and beautiful sculptures [51, 52] and shell components [20] can all be folded from a single sheet, as shown in Fig. 2-1G-H and Fig. 2-1I, respectively.

A range of sheet materials is suitable for folding, such as timber [53, 54], metal [18, 55], plastic [56, 57], and composite sheets [58, 59]. These materials are incorporated with diverse origami patterns for generating different behaviours. An introduction of origami patterns is further discussed in the following section.

2.1.2 Origami Patterns

Origami patterns map all creases utilised in folded configurations as unfolded 2D diagrams [60, 61]. They can be described using the following terms [62]:

- A *crease* represents either a *mountain* or *valley* fold, corresponding to convex and

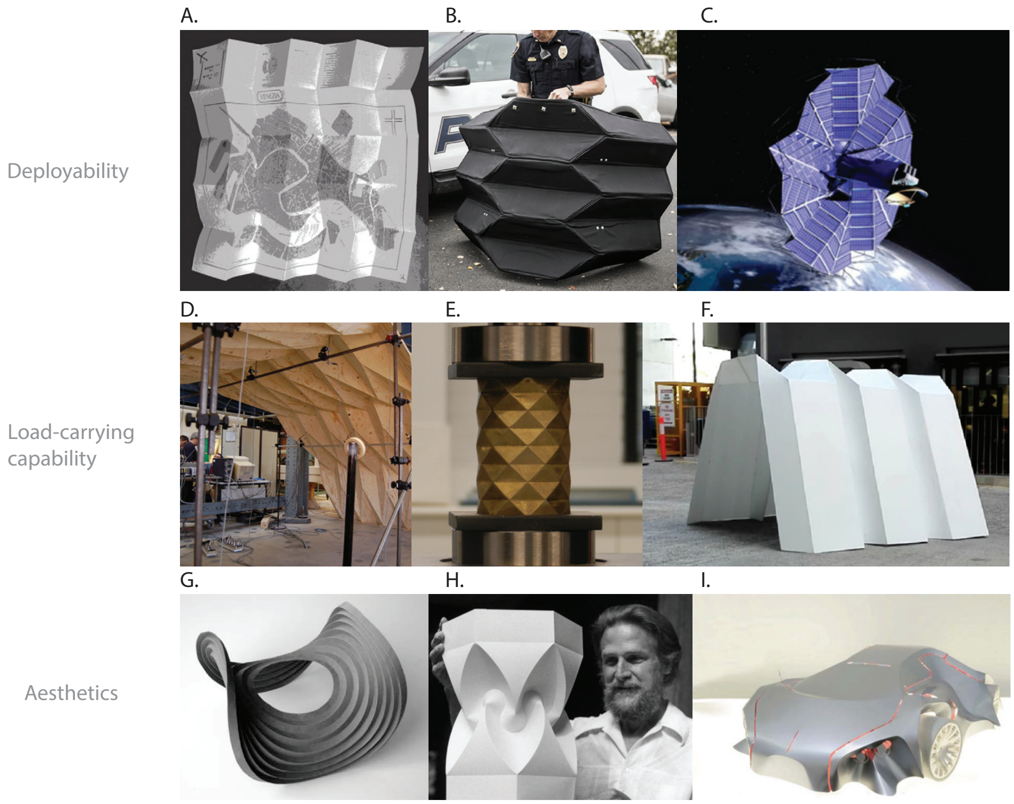

Fig. 2-1 Origami-inspired structures. (A) Foldable subway map [46]. (B) Deployable ballistic barrier [47]. (C) Origami solar array [24]. (D) Folded plate structure [48]. (E) Energy absorption tube [49]. (F) Folded accordion shelter [50]. (G) A reconstructed Bauhaus model [51]. (H) Hexagonal Column with Cusps [52]. (I) Gregory Epps' car design [20]. Images reproduced with permission.

concave folds, respectively.

- A *vertex* is a point intersected with two or more creases.
- The *degree* of vertex is the number of creases intersecting at the vertex.
- The *folded state* is the end or intermediate stage of a folding motion.

The geometry and mountain-valley assignment of creases are major design considerations in determining the shape of a folded state. For the purposes of this thesis, origami patterns are classified into two types based on the crease shape, *straight-crease origami* and *curved-crease origami*, as shown in Fig. 2-2A-2-2B, respectively.

2.1.2.1 Straight-crease Origami

Straight-crease origami are capable of generating complex 3D forms made up of polygonal facets connected with straight crease lines. They possess *developability*, that is the ability to be folded from a continuous flat sheet, for making planar materials a great use in engineering applications. The developability of a straight-crease origami is enforced with a vertex angle criterion, specifically that the summation of angles around each vertex must equals to 2π [63].

Straight-crease origami may also possess *rigid-foldability*, referring to the fact that

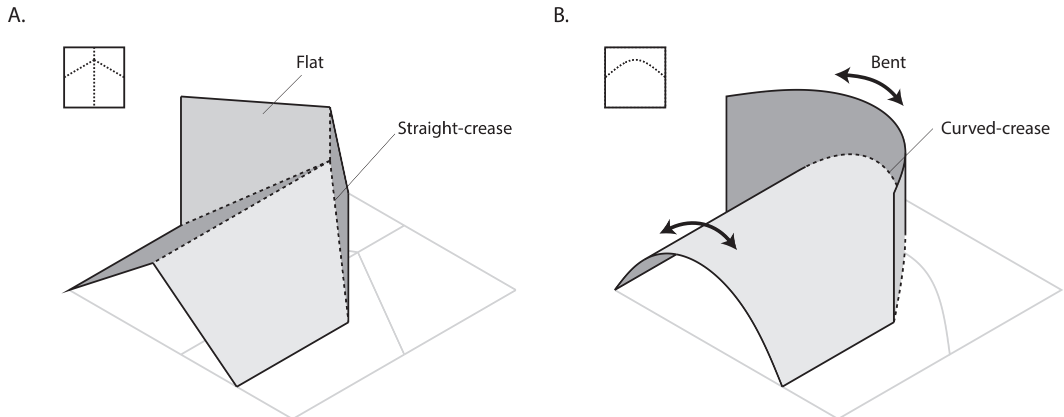

Fig. 2-2 Origami patterns and their design components. (A) Straight-crease origami. (B) Curved-crease origami.

facets do not stretch or twist during a *rigid folding* motion, hence enabling folding of rigid materials. Many methods have been developed for judging the rigid foldability of diverse straight-crease patterns. For example, Huffman [63] and Miura [64] employed the Gaussian curvature theory to study rigid-foldable origami using a 4-degree polyhedral vertex; Watanabe and Kawaguchi [65] showed that their diagram and numerical methods are sufficient to be applied on several 4 and 5-degree patterns according to their mountain–valley assignments; Tachi [66, 67] utilised his numerical algorithms for simulating the folding motion of one-DOF rigid-foldable origami based on the kinematic of 4-degree vertices; and many kinematic model-based methods are also available which consider origami patterns as the assembly of spherical linkages [41, 68–70].

Among many rigid-foldable patterns, the *Miura pattern* is a common 4-degree pattern due to its pattern simplicity and the one-DOF characteristic [64, 71]. Extensive research has been conducted for the Miura pattern and its derivatives, specifically in the field of geometric modelling and the investigation of kinematic and mechanical behaviours. For example, Wu [72] developed a set of geometrical relations for simulating folded shapes and folding motions of Miura, Arc, and Arc-Miura patterns; Gattas et al. [73] extended Wu's modelling approach to non-developable Miura pattern, non-flat foldable Miura pattern, and tapered Miura pattern; Klett and Drechsler [74] studied the tessellation of Miura pattern for their foldcores; and Ma et al. [75] explored graded Miura patterns for realising graded structural stiffnesses. Several of these patterns are further utilised in this thesis, including Miura, Arc, and Arc-Miura patterns, as shown in Fig. 2-3A-C, respectively.

Common 6-degree rigid-foldable patterns include the *Yoshimura pattern*, *Kresling pattern*, and *Waterbomb pattern*, as shown in Fig. 2-4A-C, respectively, which are all possessing a multi-DOF characteristic. Note that the Yoshimura and Kresling pattern are made up with the same base, where all vertices are intersected with four mountain creases and two valley creases; the Waterbomb pattern is the combination of two kinds of vertices, including vertices intersected with four mountain creases and two valley creases, and two mountain creases and four valley creases. Owing to the flexibility of thin sheets, these patterns can produce a non-rigid folding motion in their tubular forms, typically involving a multi-stability or nonlinear buckling behaviours [76–78]. For example, the Yoshimura pattern can be naturally formed in buckling of thin-walled cylinders under lateral compression [79–81], the tubular Kresling pattern can be deployed to multiple stable states [78, 82], and the Waterbomb pattern can form a tubular configuration with a non-uniform radius [83].

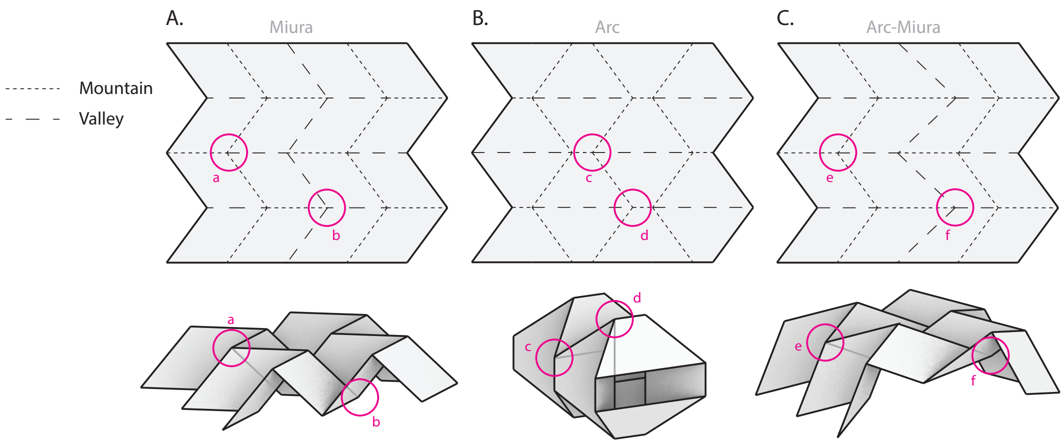

Fig. 2-3 4-degree patterns and their folded forms. (A) Miura pattern. (B) Arc pattern. (C) Arc-Miura pattern.

2.1.2.2 Curved-crease Origami

Curved-crease origami arise as a hybrid of sheet folding and bending. They use curved folds to impart surfaces with non-zero principal curvatures during their non-rigid folding motion. This striking feature has led to diverse interesting 3D shapes with developability. The developability of curved-crease origami can be evaluated using the Gaussian curvature theory, which will be further explained in the following section.

The folded state of a curved-crease origami is usually determined mechanically by minimising the total elastic energy from the sheet and the crease [84, 85]. This can result in two types of curved folds, including *non-planar curved-fold* and *planar curved-fold* [86, 87], as shown in Fig. 2-5A-B, respectively. If there is a torsion remaining within the crease, a non-planar curved-fold is formed; and if there is zero torsion within the crease, then a planar curved-fold is formed. A random curved-crease origami in fact can be a composition of both non-planar and planar curved folds, as demonstrated in [20].

Unlike straight-crease origami, curved-crease origami 'patterns' are not named with strict classification, but they are seen in many well-known historical aesthetic works, such as the 'Bauhaus model', 'Hexagonal Column with Cusps', and Gregory Epps' car design, as shown in Fig. 2-1G-I, respectively. These examples are also important figures representing the development of knowledge in curved-crease origami: the classic 'Bauhaus model' was long been designed using the trial and error method in the late 1920's [51]; the 'Hexagonal Column with Cusps' was designed with a mathematical definition in the 1970's, which

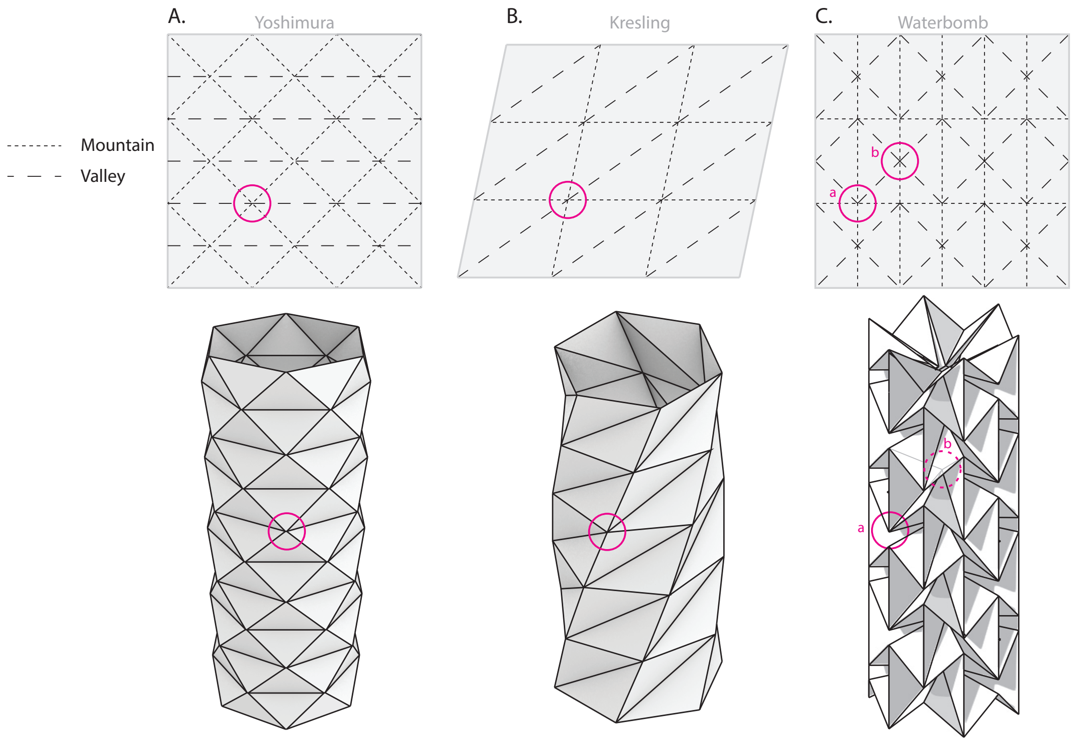

Fig. 2-4 6-degree patterns and their tubular folded forms. (A) Yoshimura pattern. (B) Kresling pattern. (C) Waterbomb pattern.

had a strong connection to a computational process [52]; and Gregory Epps' car design was designed to demonstrate the potential of future robotic manufacturing technologies [8, 20]. More examples can be found in a comprehensive history of curved-crease origami documented in [88].

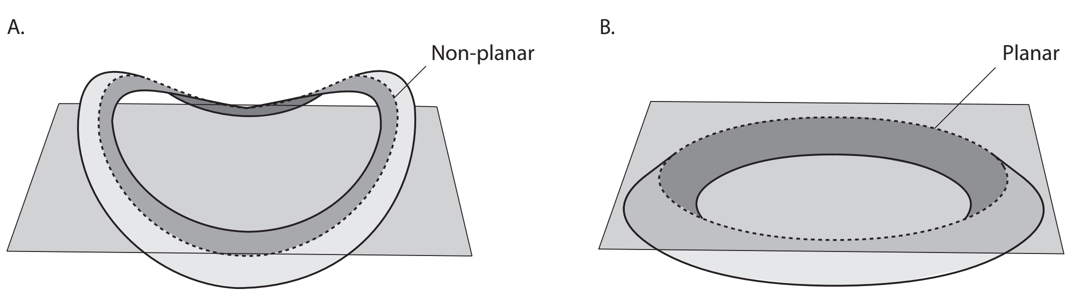

Fig. 2-5 Types of curved-fold. (A) Non-planar curved-fold. (B) Planar curved-fold.

2.1.3 Developable Surfaces

2.1.3.1 Gaussian Curvature of Surface

The *Gaussian curvature* (or total curvature) K is an intrinsic measure to describe the characteristic of a smooth surface [89]. It is calculated as the product of *principal curva-*

tures, κ_1 and κ_2, at a point on the surface:

$$K = \kappa_1 \kappa_2 \tag{2-1}$$

One way to find the point of principal curvatures is employing a moving Darboux frame (or normal plane) on the smooth surface, where the intersection will form a 2D curve and enables the evaluation of plane curvatures κ for finding κ_1 and κ_2, as shown in Fig. 2-6. Plane curvature at a point can be calculated as:

$$\kappa = \frac{1}{\rho} = \frac{d\theta}{ds} \tag{2-2}$$

where ρ is the radius of an imaginary osculating circle sharing the same tangent and curvature, also known as the radii of curvature. Using the osculating circle is a geometric way to represent the curvature. The physical way to understand the curvature is based on the change of the tangent angle $d\theta$ of the infinitesimal segment ds. Being a plane curvature, positive curvature refers to a concave feature, negative curvature refers to a convex feature, and zero curvature refers to a planar feature.

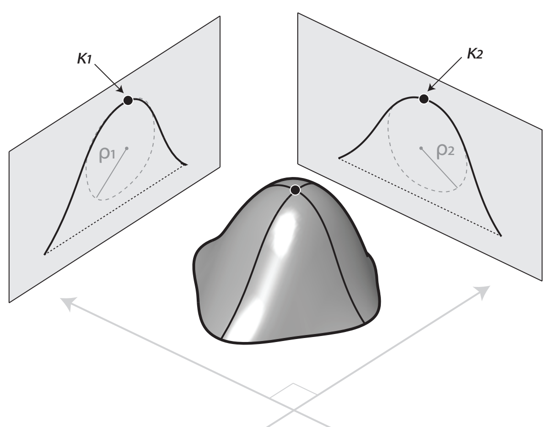

Fig. 2-6   Principal curvatures of a smooth surface.

The characteristic of a smooth surface can be determined based on the sign of the Gaussian curvature. If $K > 0$, a dome-like surface is formed with principal curvatures pointing toward the same direction, as shown in Fig. 2-7A. If $K = 0$, a smooth *developable surface* can formed with one principal curvature being zero and the remaining principal curvature being non-zero, as shown Fig. 2-7B (described further below). If $K < 0$, a saddle-like surface is formed with principal curvatures pointing toward opposite directions, as shown in Fig. 2-7C.

2.1.3.2 Fundamental Types of Developable Surface

There are three types of fundamental 3D developable surface. They are cylindrical, conical, and tangent developable surfaces [90–92]. Flat planes are also 2D developable surfaces as they are made up with zero principal curvatures. Smooth developable surfaces have

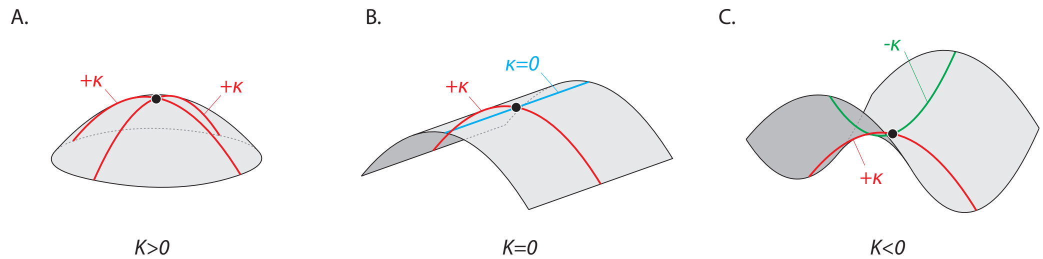

Fig. 2-7 Gaussian curvature of smooth surfaces. (A) $K > 0$: Dome-like surface. (B) $K = 0$: Developable surface. (C) $K < 0$: Saddle-like surface.

a key feature in that they can be unrolled to a flat plane without any distortion. Therefore, they are suitable to the modelling of surfaces which can be made out of sheet materials. Note that developable surfaces are a very small subset of all possible smooth surfaces, as most surfaces are non-developable and possessing a doubly curved form, that is $K \neq 0$, such as spheres and hyperboloid surfaces.

2.1.3.3 Generation of Developable Surfaces

Developable surfaces are *ruled surfaces* which can be generated by the continuous motion of a straight line moving along a space curve [93–95]. The space curve is called a *directrix* and the straight line is called a *generator* or *ruling* of the surface [12]. This definition can be used for manipulating the shape of a developable surface. For example, a cylindrical surface can be generated by a set of parallel rulings arranged in space, as shown in Fig. 2-8A; a conical surface can be generated by a set of non-parallel rulings meeting at an apex, as shown in Fig. 2-8B; and a tangent developable surface can be spanned by a set of rulings tangential to a space curve, as shown in Fig. 2-8C.

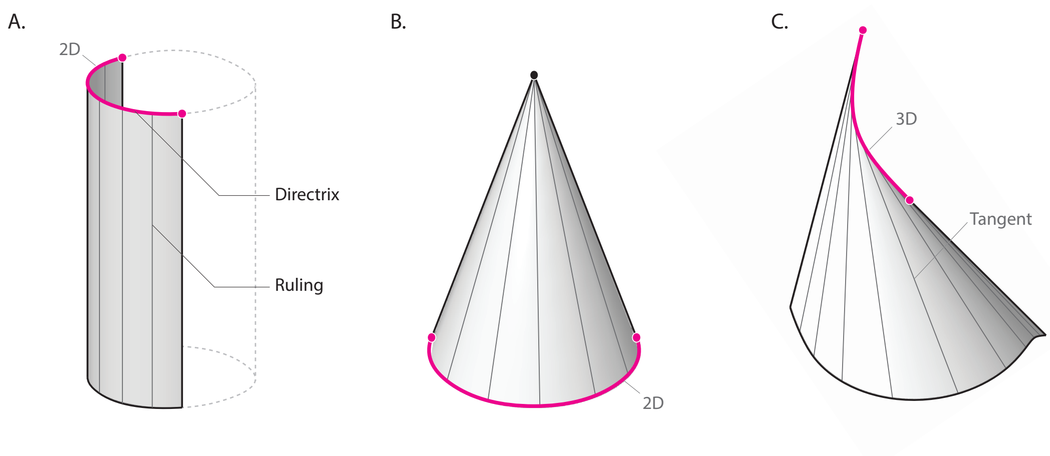

Fig. 2-8 Generation of fundamental types of developable surface. (A) Cylindrical surface. (B) Conical surface. (C) Tangent developable surface.

2.1.3.4 Origami Surfaces

Origami surfaces can be understood as a special extension of developable surfaces, as they are the assembly of two or more developable surfaces subjected to geometric constraints that preserve the *developability* across crease lines. For example, the Miura pattern is a developable surface made up with repetitive parallelogram planes; and a simple curved-crease surface can be obtained from two cylindrical surfaces sharing a common *developability constraint* [12, 96], as shown in Fig. 2-9.

A physical curved-crease pattern can be folded to different 3D minimum bending energy configurations depending on boundary constraint conditions. These folded configurations can be described as the assembly of different fundamental developable surfaces [63, 86]. If a planar curved fold is formed, it can be considered as the assembly of cylindrical or conical surfaces, where the crease is kept in a 2D plane [20], as shown in Fig. 2-10A-B, respectively. If a non-planar curved fold is formed, it can be considered as the assembly of tangent developable surfaces, where the crease is transformed to a 3D space curve [13], as shown in Fig. 2-10C.

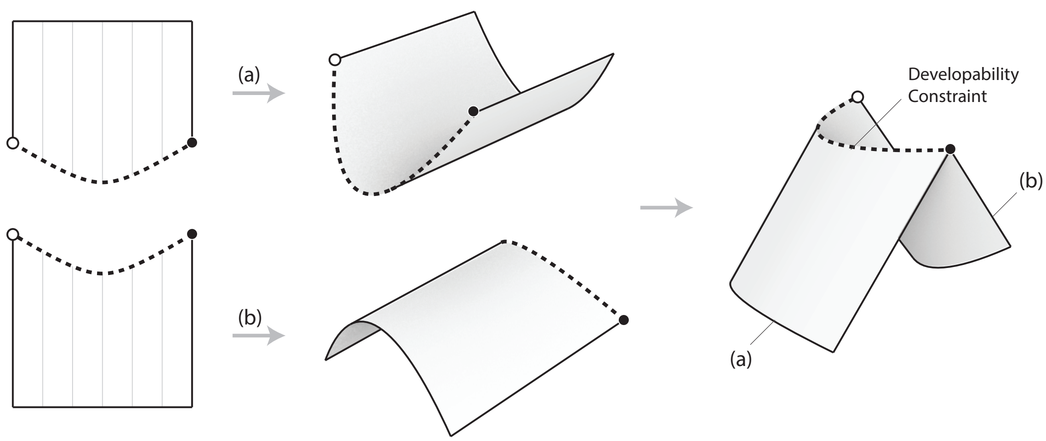

Fig. 2-9 Assembly of smooth developable surfaces sharing a common developability constraint. Figure from left to right: Flat sheet components, 3D developable surfaces, and curved-crease origami.

2.2 Modelling of Curved-crease Origami

Driven by new applications of curved-crease origami, recent research effort has been devoted to accurately model the folded form of curved-crease origami [57, 97]. By necessity, these all must capture two characteristics of curved-crease origami surfaces: enforcement of a constant zero Gaussian curvature for surface *developability* and evaluation of the non-zero principal curvature for surface *bending* behaviour.

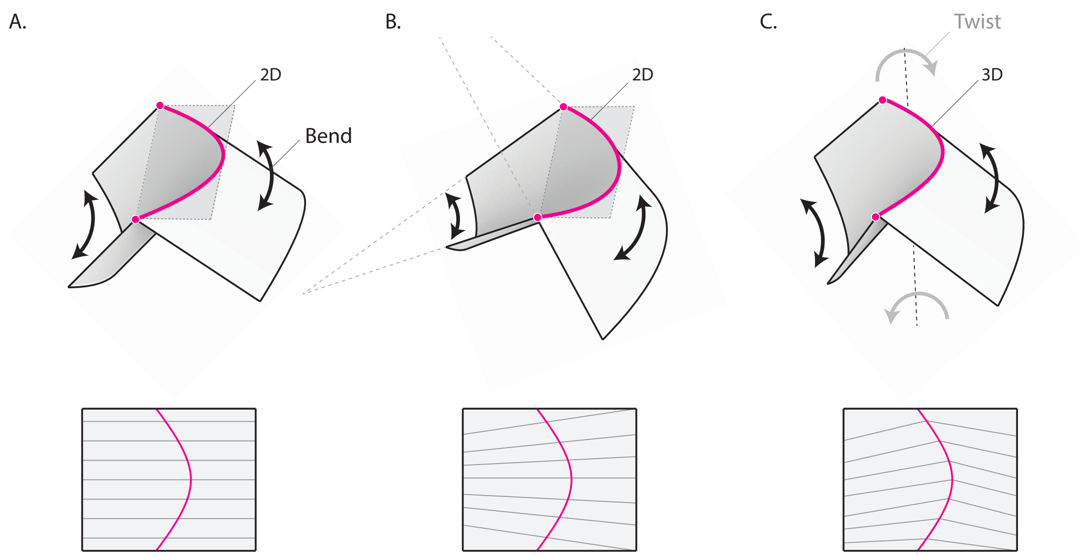

Fig. 2-10 Curved-crease surface assembled from (A) cylindrical surfaces, (B) conical surfaces, and (C) tangent developable surfaces.

2.2.1 Geometric Methods for Folded Forms

2.2.1.1 Transformation of Developable Surfaces

The *mirror reflection method* is one of the simplest geometric construction methods for generating curved-crease surfaces based on the transformation of smooth developable surfaces [87]. The transformation is done by intersecting a plane through a developable surface and obtaining the folded configuration by plane mirror reflection, as shown in Fig. 2-11A. The mirror reflection method is therefore capable of generating planar curved folds but not non-planar curved folds, as shown in Fig. 2-11B-C. This method was developed with a key theorem of that, *'A surface generated by applying mirror reflection to a part of an origami surface is also an origami surface'*. That is to say, rulings of the folded surface are also reflected about the flat mirror plane. Multiple reflections can thus generate a complicated origami surface with sequential planar curved folds, as shown in Fig. 2-11D. A key benefit of using the mirror reflection method is that the developability constraint of a curved-crease surface can be concisely obtained. This enabled Mitani [98] to develop a fast interactive computational modelling tool for 3D column-shaped curved-crease origami. However, existing utilisations of the mirror reflection method does not yet account for surface bending behaviours, hence the accuracy is largely unknown.

2.2.1.2 Transformation of Base Rigid-foldable Patterns

Gattas and You [21] proposed a curved-crease creation method which transformes a known straight-crease origami pattern into curved-crease variants. The Miura pattern and its derivatives were used as 'base' straight-crease patterns in their proposal. Analytical 'ellipses' are defined through sequential zigzag ridges of the base pattern for generating

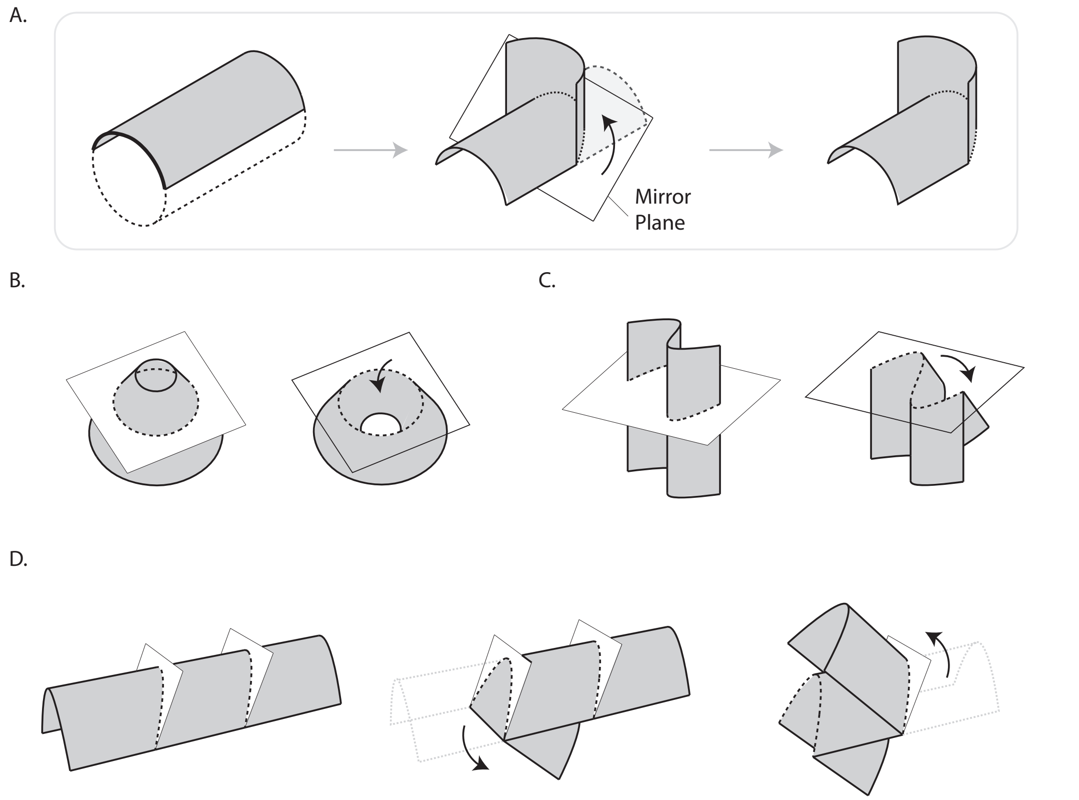

Fig. 2-11 Curved-crease origami creation using the mirror reflection method. Single-crease reflection from a (A) simple curved surface, (B) cone surface, and (C) extruded sine curve. (D) Multi-crease reflections from a simple curved surface.

edge curves of the curved-crease surface, as shown in Fig. 2-12A. Note that three zigzag points do not provide enough information to create an unique ellipse, a gradient parameter is defined in the ellipse creation procedure. Elliptical geometry is used, as the intersecting geometry of a mirror reflection plane and a cylindrical surface is an elliptical curve, as shown in Fig. 2-12B. This indicates that the curved-crease surface is designed to possess an 'arc surface' (cylindrical surface) as the non-zero principal curvature. This method is considered to extend and provide a parametric definition for the mirror reflection method, hence the developability condition is preserved during the transformation. Furthermore, Chandra et al. [99] developed a modelling tool for generating curved-crease tessellation of freeform geometries which is also based on the transformation of straight-crease patterns. The main advantage of these transformation methods is that they are capable of parametrizing and modelling curved-crease folded forms for a specified target volume. However, the limitation of these transformation methods is again that they do not yet consider any bending energy within the geometry, hence the correspondence between designed and manufactured geometry is approximate only, as demonstrated in [9].

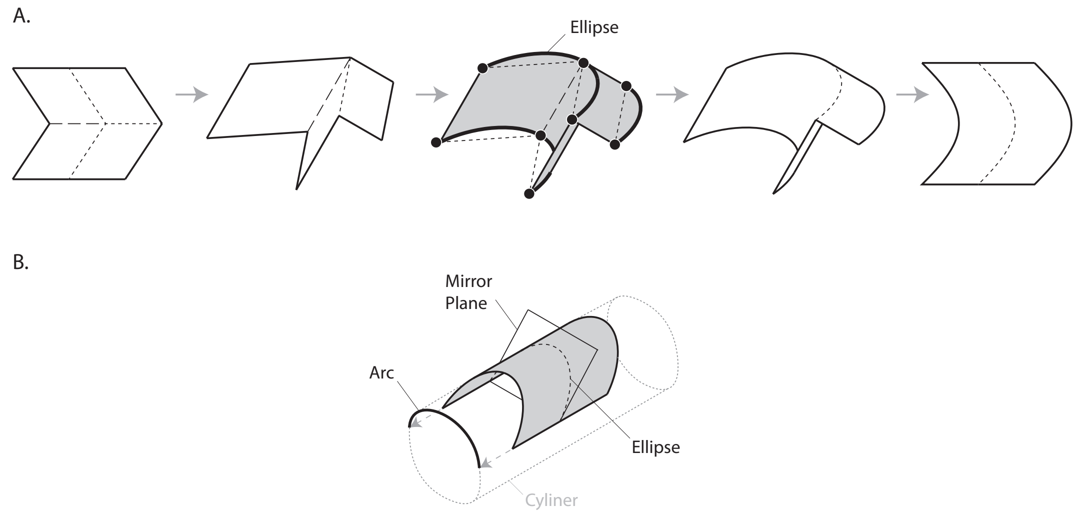

Fig. 2-12 Curved-crease origami creation from base rigid-foldable patterns. (A) Transformation procedure of a folded Miura pattern to its curved-crease variant. (B) The principle of the transformation method.

2.2.2 Numerical Methods for Folded Forms

Above analytical descriptions of curved-crease origami are suitable for simple planar curved folds. Numerical methods (or *discrete methods*) are employed for modelling more complex curved-crease surfaces, such as non-planar curved folds. These require the curved-crease surface to be numerically discretised to allow vertex developability constraints to be enforced at pattern vertices [20, 21, 100], with discrete rulings approximating either an *inexact* or *exact* bending behaviour. A *curved-crease approximation* can then be generated in a computational environment based on those identified rulings, by fitting a planar quadrangle (PQ) mesh to the curved surface [101, 102].

2.2.2.1 Inexact Bending Behaviour

Inexact methods approximate an observed curved crease surface but are simplified to avoid explicit consideration of material bending behaviours.

An inexact PQ mesh can be simply generated through tracing of a physical prototype [20]. This method is considered as a hybrid physical and digital design technique which is capable of providing reasonable approximation of material behaviours. The benefit of building physical prototypes is that designers can be inspired from the reaction of physical curved-crease behaviours and create a range of design possibilities. This method has also demonstrated that a curved-crease approximation can be recreated in different scales and materials by utilising the same PQ mesh assembly. However, designing a desired folded from can be a challenging task, as traditional origami trial and error relies on experience and time.

Gattas and You [21] showed that a pre-defined analytical curved-crease surface can be discretised into a PQ mesh assembly. The approximation was achieved by subdividing cylindrical and conical surfaces into rigid origami strips by following their ruling orientations, corresponding to non-tapered and tapered curved-crease Miura geometry in their proposal, respectively. Although they did not consider any bending behaviours in their pre-defined geometries and the discretisation process, they have demonstrated that a good curved-crease approximation can be achieved with finer divisor rulings, as demonstrated in their physical prototypes.

A higher resolution of curved-crease approximation can also be achieved computationally by smoothing a coarse PQ mesh input based on the framework of dynamic relaxation [96]. However, non-developable mesh assemblies are formed during the smoothing process, as the mesh quantity, size, and shape are progressively changed. This method thus uses a relaxation method for realising an optimised approximation of a curved-crease surface which is developable and possessing planar meshes.

A few computational methods are available to create an inexact curved-crease approximation by specifying surfaces rulings about a pre-defined curved fold using different discretisation algorithms [103, 104]. These methods are different to mesh-based methods, as they allow users to deal with smooth developable surfaces based on continuous curves and splines. The relationship between surface rulings and the shape of a folded configuration were closely considered in these methods, hence enabling interactive manipulation of curved-crease surfaces.

2.2.2.2 Exact Bending Behaviour

Exact methods combine geometric developability constraints with a consideration of material bending behaviours to give a stronger approximation of a curved-crease surface.

Kilian et al. [10] presented a quadratic discrete bending energy formulation for fitting the PQ mesh to a curved-crease surface using an optimisation based computer processes. Their method optimised for minimum discrete bending energy from curvature while enforcing developability at vertices. A physical model can be scanned and digitally reconstructed using their optimisation algorithm, which will then form a reasonable approximation of a folded sheet.

Solomon et al. [105] presented a subdivision-based modelling approach for transforming a specified straight-line ruling pattern to a curved developable surface. Their method first decomposes the input geometry into multiple developable patches. For smoothly bent regions, they subdivide rulings and relax them by minimizing a curvature-based bending energy while enforcing the exact developability. The smoothed region is hence developable and consists of finer rulings with the consideration of material behaviours.

Although these exact methods have captured the surface developability with the consideration of material behaviours, there are three ongoing challenges. First, the capacity of these approximation methods for accurately modelling a folded form is largely unknown, as validations do not yet exist. Second, these methods did not suggest the design process for defining the input surface. Third, these methods have not yet explored the *folding motion* of the generated model, which will be further discussed in the following section.

2.2.3 Numerical Folding Simulations

Modelling the folding motion of a curved-crease origami is an extremely challenging task, as the complexity of accurately capturing both surface developability and sheet bending behaviours is amplified when considering motion. Numerical methods were developed to simulate the folding behaviour of a known curved-crease surface, typically involving the use of *rigid-foldable curved-crease approximations* [20, 21]. These methods first require a pre-defined curved-crease surface to be numerically discretised into rigid mesh assembly using above inexact and exact methods. The generated model typically possesses 4-degree vertices and a single-DOF rigid-foldable characteristic. This then enables the compliant folding motion of a curved-crease origami to be approximated using a rigid folding motion. This technique has been successfully utilised in robotic constructions where the folding simulation is used as the instruction for manufacturing curved-crease components, as demonstrated in [8].

2.2.3.1 Rigid-foldable Curved-crease Miura Pattern

This thesis adopts the numerical folding simulation method developed by Gattas and You [21] for a unit curved-crease Miura pattern. The simulation method is briefly summarised here as it will be utilised in later chapters. Note that this method can also be used for other curved-crease patterns made up with multiple creases, if creases are spanning along the same direction and crossing common boundary edges.

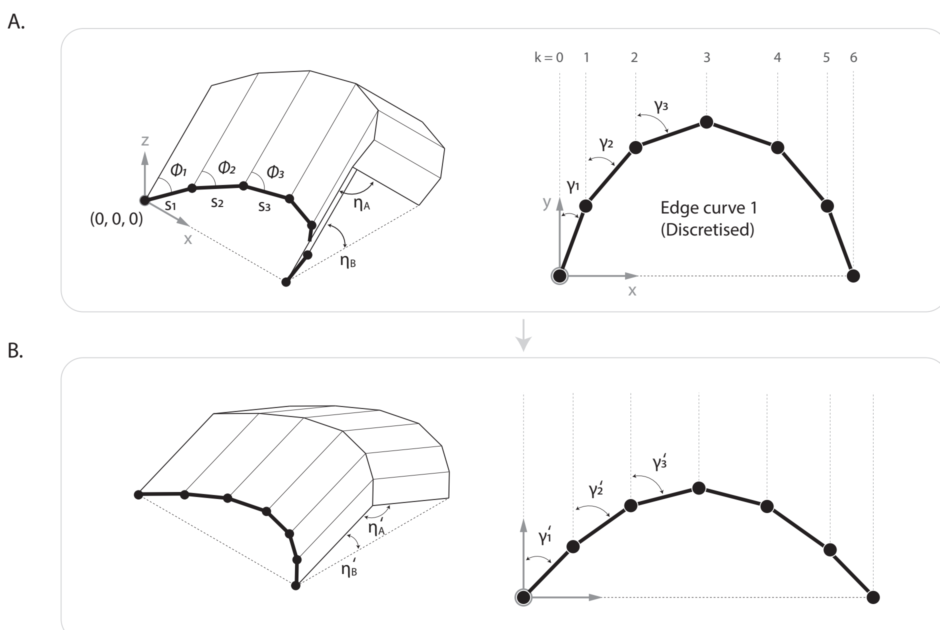

Fig. 2-13 Folding simulation of a rigid-foldable curved-crease Miura pattern. (A) Initial state. (B) Intermediated folded state.

First, the rigid-foldable PQ mesh assembly is created by subdividing the unit curved-crease Miura pattern into rigid origami strips connected along common longitudinal edges, as shown in Fig. 2-13A. The folding motion of each rigid strip can be characterised by a varying common edge angle, η_A, using the method described in [73]. That is to say, the change in shape of Edge curve 1 determines the complete motion of the rigid strips assembly.

At the initial state, Edge curve 1 can be described with control vertices in a Cartesian system $(+x_k, +y_k)$ from the origin, where subscript k denotes the vertex position, as shown in the sub-figure in Fig. 2-13A. Three design parameters about Edge curve 1 are specified, they are: length of line segments $[s] = s_1, s_2, s_3, ...s_k$, angles between line segments and the y-direction $[\gamma] = \gamma_1, \gamma_2, \gamma_3, ...\gamma_k$, and lateral sector angles $[\phi] = \phi_1, \phi_2, \phi_3, ...\phi_k$, which can be calculated as,

$$\phi_k = \cos^{-1}\left(\frac{\cos\eta_B}{\cos\gamma_k}\right) \tag{2-3}$$

where $\eta_B = (\pi - \eta_A)/2$ is the initial angle between the side length of the pattern and the base plane.

During intermediate folded states (Fig. 2-13B), $[s]$ and $[\phi]$ remain unchanged and the new $[\gamma'] = \gamma'_1, \gamma'_2, \gamma'_3, ...\gamma'_k$ can be calculated as

$$[\gamma'] = \cos^{-1}\left(\frac{\cos[\phi]}{\cos\eta'_B}\right) \tag{2-4}$$

where η'_B is determined by the current edge angle $\eta'_A = \pi - 2\eta'_B$. Knowing $[s]$ and $[\gamma']$ allows nodal translations $(\Delta x, \Delta y)$ of Edge curve 1 to be calculated for $k > 0$ (excluding the origin), where

$$\Delta x = [s]\sin[\gamma'] \tag{2-5}$$

$$\Delta y = [s]\cos[\gamma'] \tag{2-6}$$

Therefore, the shape of new Edge curve 1 at an intermediate folded state can be determined by joining the origin with displaced vertices $((x_{k>0} + \Delta x), (y_{k>0} + \Delta y))$. A folded PQ mesh assembly is then created by projecting the new Edge curve 1 to other edge curves, determined by η'_B and η'_A. Finally, the folding motion is simulated with multiple intermediate folded states being specified.

2.2.3.2 Compliant Behaviours of Curved-crease origami

Once the folding motion of a rigid-foldable curved-crease approximation is simulated, compliant mechanism theory using a pseudo-rigid-body-model (PRBM) can be employed as one suggested strategy for modelling its folding mechanics [106, 107]. The PRBM approach assumes that the elastic strain energy is stored only in creases, which act as torsional springs with an elastic stiffness, as shown in Fig. 2-14. The total strain energy U_{PRBM} is calculated as the summation of the energy stored in both longitudinal and transverse creases, calculated based on the change of crease line dihedral angles:

$$U_{PRBM} = \sum \frac{1}{2} k_s (\alpha'_d - \alpha_d)^2 \tag{2-7}$$

where k_s is the crease stiffness and α_d and $\alpha_d^{'}$ are dihedral angles at initial and deformed states, respectively.

If crease stiffness is assumed as zero, folding motion corresponds to a rigid-foldable straight-crease origami folding mechanism. If crease stiffness is calibrated to material bending stiffness, this then gives a more accurate representation of a compliant folding motion, but still enforces a rigid-foldable motion path [108].

PRBM has been demonstrated to be effective for modelling straight-creased compliant mechanisms [109, 110], but recent research suggests that minimum energy surface rulings will change as a curved surface folds [111]. It is therefore unknown if PRBM is valid for curved-crease compliant mechanisms and there are no experimental data sets or analytical solutions yet available to support such validation.

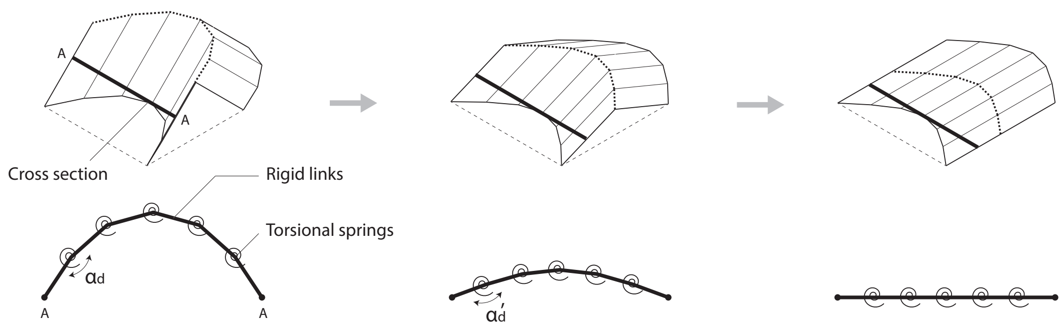

Fig. 2-14 Curved-crease origami folding simulation using PRBM.

2.3 Large Elastic Bending

This thesis shall apply large elastic bending theory to origami design. The fundamental theory of elastic bending mechanics is briefly summarised below.

2.3.1 Elastica Curves

Elastica curves are geometries that describe the large elastic deformation of a slender beam [112]. Early mathematical models describe the elastica geometries as one-dimensional curves and were subsequently shown in mechanics models to represent naturally stable bending forms, that is curves corresponding to minimum bending energy configurations and also postbuckling geometries [113–115]. They have been extensively studied for a range of boundary conditions and deformations (Fig. 2-15), with a typical elastica for a pinned-pinned beam with uniform bending stiffness (Fig. 2-16). The curve represents the centreline geometry of the deformed beam and possesses a non-uniform curvature, in contrast to the uniform curvature typically assumed for small beam deformations.

From structural mechanics, the relationship between beam curvature κ and deflection y is given by Equation 2-8. The non-linear denominator term arises from the large defor-

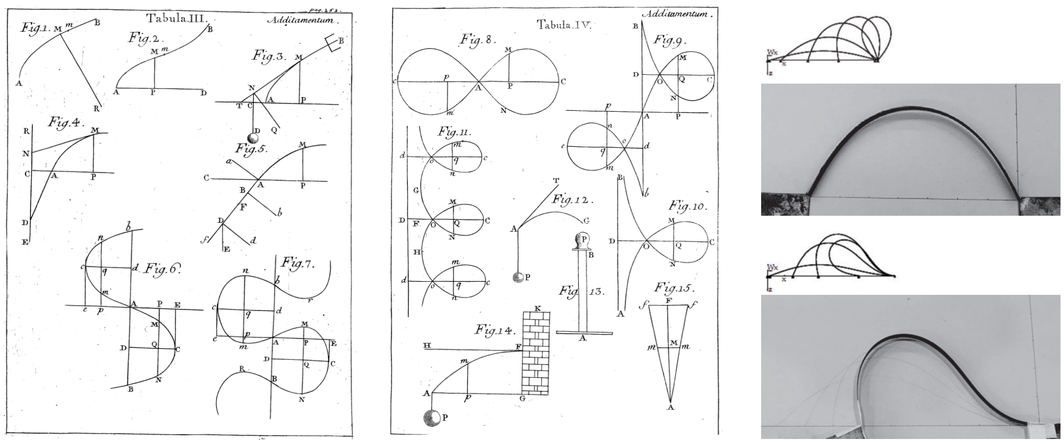

Fig. 2-15 Elastica curves for different boundary constraint conditions. Images on left are from [112]. Images on right are from [14] and curves generated from prototype deformation. Images reproduced with permission.

mation strain-displacement relation, which includes finite rotation of a beam element. The constitutive relationship is unchanged from linear theory, with curvature related to moment M and flexural rigidity value EI as shown.

$$\kappa = \frac{y''(x)}{\left(1 + y'(x)^2\right)^{\frac{3}{2}}} = \frac{M}{EI} \tag{2-8}$$

The elastica profile is obtained through integration of Equation 2-8, however retention of the denominator term makes this a complex task. The denominator term is usually neglected in engineering structures with assumed small beam deformations, however in large elastic deformation the term cannot be neglected. Mathematically, the solution for certain idealised cases can be achieved with Jacobian elliptic functions [116], however explicit solutions have also been derived, including for the case of one-dimensional simply-support beams. This thesis shall employ the explicit solution developed by Pacheco and Piña [117] and Valiente [118], which expresses the elastica curve in Cartesian coordinates and is published as a Visual Basic script online [119]. The solution is summarised as follows.

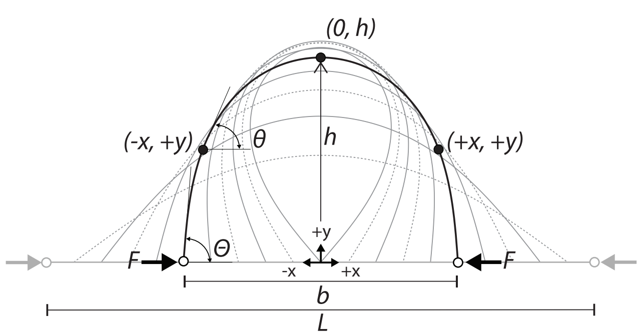

Fig. 2-16 Elastica curves for a simply-support slender beam with uniform bending stiffness.

The 1D rod shown in Fig. 2-16 has three length parameters: support distance after deformation b, beam height after deformation h, and beam length before deformation (arc length) L. These can be explicitly related to the *m parameter*, which is a quantity used to evaluate elliptic functions and generally employed such that $0 < m < 1$ [120]. Relations between the length and m parameters are [117]:

$$\frac{b}{L} = 2\frac{E(m)}{K(m)} - 1 \tag{2-9}$$

$$\frac{h}{L} = \frac{\sqrt{m}}{K(m)} \tag{2-10}$$

$$\frac{b}{h} = \frac{2E(m) - K(m)}{m} \tag{2-11}$$

where $K(m)$ is the complete elliptic integral of the first kind and $E(m)$ is the complete elliptic integral of the second kind. The m parameter can be additionally related to the tangent angle of the elastica curve at the initial (pinned support) location Θ with [118]:

$$\Theta = 2\sin^{-1}\left(\sqrt{m}\right) \tag{2-12}$$

A unique elastica curve can be defined in a Cartesian system $(\pm x, y)$ from Θ and m parameters. First, the vertical coordinate y and tangent angle θ are related with [118]:

$$y = \frac{0.5L\sqrt{2}\sqrt{\sin(\Theta - \frac{\pi}{2}) - \sin(\theta)}}{K(m)} \tag{2-13}$$

which can be rearranged as:

$$\theta = \sin^{-1}\left(\sin\left(\Theta - \frac{\pi}{2}\right) - \left(K(m)\frac{y}{0.5L\sqrt{2}}\right)^2\right) \tag{2-14}$$

Second, by specifying a range from 0 to h for y coordinates in Equation 2-14, the rotation θ at each point coordinate is obtained. This is used to determine the corresponding $\pm x$ coordinates as:

$$\pm x = \sqrt{\frac{EI}{2F}}\int_{\theta}^{-\frac{\pi}{2}} \frac{\sin\omega}{\sqrt{\sin(\Theta - \frac{\pi}{2}) - \sin\omega}}d\omega \tag{2-15}$$

where F is the value of the two opposing horizontal end forces. F is obtained through equilibrium and by assuming a uniform beam flexural rigidity of EI [117]:

$$F = EI\left(2\frac{K(m)}{L}\right)^2 \tag{2-16}$$

Finally, substituting Equation 2-16 into Equation 2-15, the term $\sqrt{\frac{EI}{2F}}$ can be replaced with $\frac{0.5L}{\sqrt{2}K(m)}$. The flexural rigidity term EI is eliminated and the elastica coordinates $(\pm x, y)$ are given as a purely geometric relation [118], which mean they can arise in any elastically-bent material:

$$\pm x = \frac{0.5L}{\sqrt{2}K(m)}\int_{\theta}^{-\frac{\pi}{2}} \frac{\sin\omega}{\sqrt{\sin(\Theta - \frac{\pi}{2}) - \sin\omega}}d\omega \tag{2-17}$$

Therefore, by specifying any two of b, h, L, m, or Θ, the remaining three parameters can be obtained from Equations 2-9 to 2-12 and a corresponding plot of $(\pm x, y)$ for $0 \leq y \leq h$ is obtained by evaluating Equation 2-14 and Equation 2-17.

2.3.2 Modelling Tools for Elastica Curves

There are numerous methods to model the elastica curves, summarised as follows and illustrated below (Fig. 2-17) for the case of a simply-support elastica:

- *Analytical solution*: Explicit solutions have been derived for the case of simply-support beams, but are limited for general cases. The solution is available as a parametric VB script component in Rhino/Grasshopper [119].
- *Physical form-finding*: Curves can be simply obtained by manually tracing the deformations of an elastically bent prototype. This represents the shape of centreline geometries for other scales and materials.
- *Dynamic relaxation*: Elastica curves can be numerically modelled. For example, rotational spring stiffness models can be implemented in Grasshopper/Kangaroo 2. The dynamic relaxation process will then find elastica curves which represent minimum energy configurations.
- *Finite element approach*: A straight beam can be discretized and analysed with a large-displacement non-linear finite element method. A version of this approach is available in Excel to demonstrate the constituent energy principles [121].

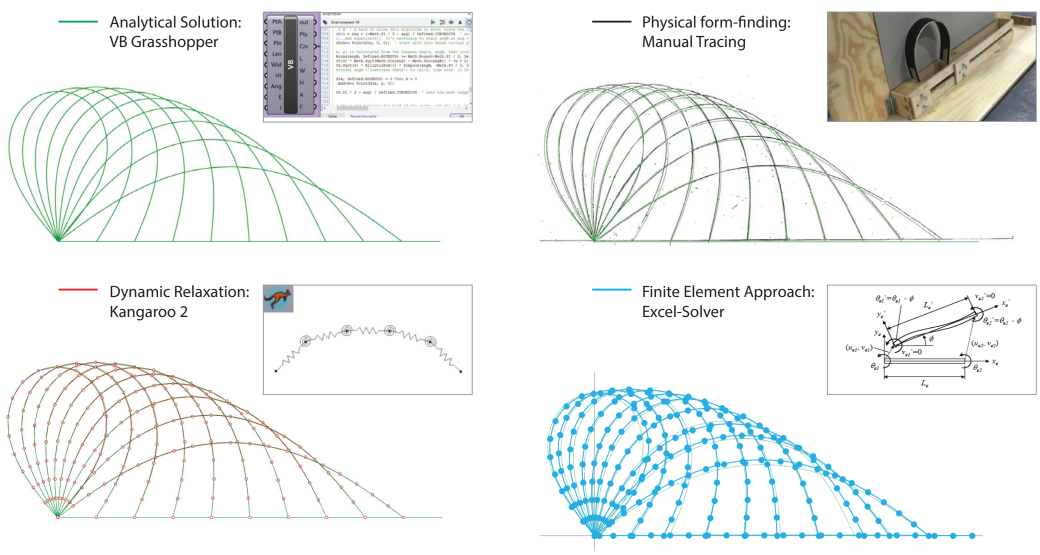

Fig. 2-17 Modelling tools for elastica curves.

2.4 Summary

The literature review shows that origami-inspired structures are popular, as many useful performance characteristics can be generated by folding origami patterns on a range of sheet materials. Curved-crease origami is a class of origami patterns which can be considered as a special extension of developable surfaces but contain regions with a non-zero principal curvature. They are capable of generating striking folded forms, hence has led to the adoption of curved-crease forms for numerous novel engineering and architectural applications. A range of modelling techniques have been developed to realise these applications, including simulation of folded forms and folding behaviours. By necessity, these all must capture two characteristics of curved-crease origami surfaces: enforcement of a constant zero Gaussian curvature for surface developability and evaluation of the non-zero principal curvature for surface bending behaviour. However, most modelling methods prioritise the developability consideration over the bending consideration. Concise descriptions are approximation only, they do not account for elastic or plastic energy behaviour and the interaction between surface bending behaviours and origami developability constraints. Other numerical approximation methods with bending consideration are computationally expensive with no experimental data sets or analytical solutions yet available to support their accuracy. Therefore, this thesis aims to create a concise and accurate curved-crease origami representation by adopting the elastica for representing sheet elastic bending behaviours into analytical transformation methods, which will avoid the need for surface discretisation.

Chapter 3 Modelling of Curved-crease Origami using Elastica Curves

This chapter presents an analytical geometric construction method for curved-crease origami with consideration of material bending behaviours and avoiding the need for surface discretisation. The new method combines a 1D elastica solution for large elastic bending deformation with a straight-crease origami projection and reflection process; it can thus concisely and accurately capture the principal surface curvature and developability characteristics of elastically-bent curved-crease origami. A surface error analysis of 3D scanned physical prototypes is used to validate the analytical model, which is shown to be accurate to within ±50% of the sheet thickness for a 2mm thick model for a range of elastica surface profiles. Limitations of the model are also explored including the derivation of a maximum compressibility limit; investigation of accuracy of numerical folding motion simulation; and an investigation of a free edge distortion behaviour which occurs in certain origami forms.

3.1 Curved-crease Origami Creation

3.1.1 Elastica Curves and Non-zero Principal Curvature of a 3D Surface

While elastic deformation of a 1D beam into a 2D curve is well understood (elastica curve), predicting the elastic bending deformation of a 2D surface when folded into a 3D form is an ongoing challenge and necessitates consideration of the principal curvatures of a surface. It is here proposed that the 2D elastica curve formulation of Equation 2-8 can be adopted as the non-zero principal curvature of a constrained class of elastically-bent 3D surfaces and, by extension, provide an analytical solution for curved-crease origami forms with developability and minimum elastic bending energy characteristics.

To illustrate the creation of a 3D form with an elastica non-zero principal curvature, first consider a unique 1D elastica curve with parameters b and h, shown in Fig. 3-1A and obtained from Equations 2-14 and 2-17. If extruded, it forms an 'isotropic' 3D shell which is both developable and possesses a minimum bending energy, shown in Fig. 3-1B. A simple curved-crease origami form can be obtained from an extruded shell using the mirror reflection method, which truncates and reflects the shell about an intersecting cutting plane as shown in Fig. 3-1C-D. If the inverted shell segment is assumed to possess the same curvature as the original shell, the 3D curved-crease origami form is both developable and assumed to also possess a minimum bending energy. The generated simple curved-crease origami is demonstrated more clearly with different views in Fig. 3-1E.

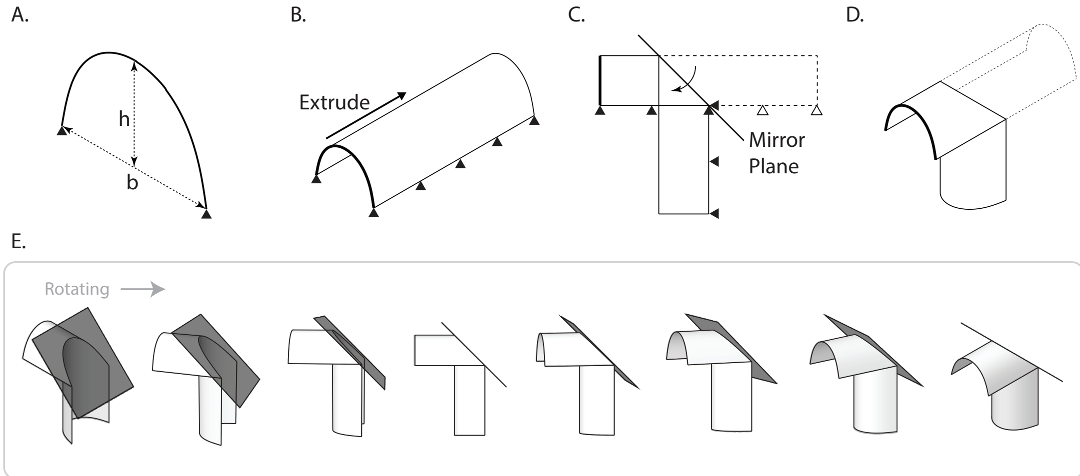

Fig. 3-1 Creation of a 3D elastica surface. (A) 1D elastica curve with parameters b and h. (B) Extruded elastica curve demonstrates the deformed 3D shell. (C) Intersecting cutting plane on a 3D shell for mirror reflection. (D) Reflected 3D folded curved-crease component. (E) Demonstration of the generated simple curved-crease origami.

Designing a more complex curved-crease surface using the mirror reflection method requires sequential specification of truncation planes and shell lengths. By reversing this process, that is by establishing reflection planes from a desired target volume, a direct method of surface design is achieved. This has been demonstrated previously by Gattas and You [21], with a 'base' rigid-foldable straight-crease origami pattern used to specify a target volume as shown in Fig. 3-2A. Straight-crease patterns have folded volumetric parameter and unfolded (developable) parameter relationships that are easily established from vertex constraints. Reflection planes are also established at vertex crease locations, so by 'projecting' a curve along folded axes and reflecting about these planes, a developable surface with an inexact bending behaviour can be parametrised. Projection of an elliptical curve was shown to be sufficient for visual approximation of a curved-crease surface and simulation of surface folding via discretisation into a planar-quadrangle (PQ) mesh, shown in Fig. 3-2B. If discrete rulings on the projected surface are increased to infinity, a continuous developable curved-crease surface is parametrised, shown in Fig. 3-2C. However, the projected elliptical curve is inexact, that is it neglects bending energy considerations, and so the geometric construction remained an approximation only.

By combining the elastica surface projection shown in Fig. 3-1 with the curved-crease surface design method shown in Fig. 3-2, a geometric construction method is achieved that concisely and accurately captures developability and bending behaviours. It includes a major assumption: the elastica remains a valid representation of the bending behaviour of the reflected surface. Key sub-assumptions are that the 'crease line' created from reflection about the truncation plane does not distort the bending behaviour of the surface; the free edges of the 3D shell do not distort the bending behaviour of the surface; and the

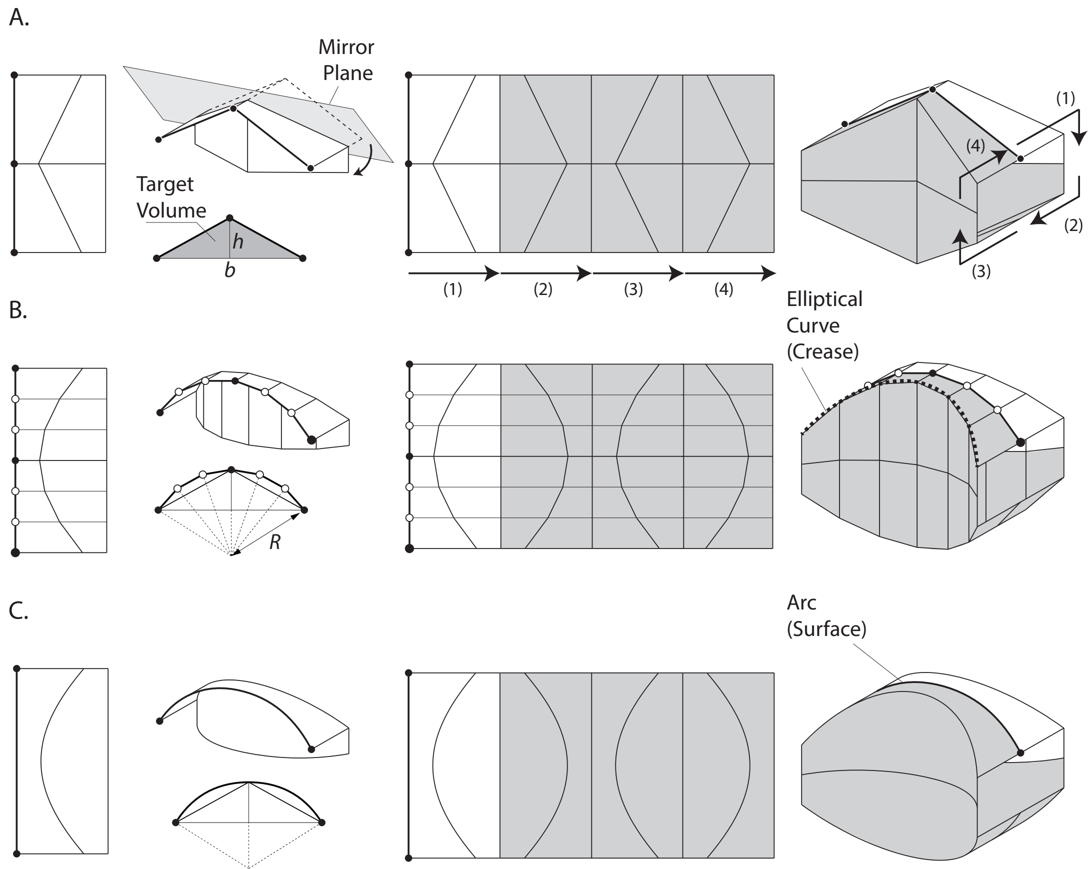

Fig. 3-2 Parametrizations of (A) base rigid-foldable straight-crease origami geometry, (B) curved-crease surface approximated with PQ mesh, and (C) inexact curved-crease surface. Each sub-figure includes unfolded unit, folded unit, 3D surface illustration, unfolded pattern, and folded pattern.

surface edge boundary condition is preserved as pinned-pinned as per the original elastica derivation. These sub-assumptions will be systematically investigated in below sections.

3.1.2 Geometry Construction Method

A geometric construction method is developed here for projection of an elastica curve onto a target folded form. A base rigid-foldable configuration is shown in Fig. 3-3A and is known as an 'Arc' pattern geometry. The unfolded configuration can be completely determined by three parameters: side lengths a_1, b_1, and sector angle ϕ. Remaining side length parameter $a_2 = 2b_1 \cos\phi + a_1$, where $a_1 < a_2$. However, the primary interest is converting a single vertex geometry into its corresponding curved-crease form with minimum elastic bending energy. Therefore, the rectangular 'transformation region' is determined by side lengths c_1, c_2, and d_1, where $c_1 = a_1/2$, $c_2 = a_2/2$, and $d_1 = b_1 \sin\phi$. The edge angles η_A and η_Z are useful in defining a particular folded configuration as shown in Fig. 3-3B. The folded configuration then provides a target volume for designing an elastica curve, where the design parameters b and h are defined as:

$$b = 2b_1 \sin\left(\frac{\eta_z}{2}\right) \tag{3-1}$$

$$h = \sqrt{{d_1}^2 - \left(\frac{b}{2}\right)^2} \tag{3-2}$$

As base pattern parameters are sufficient to define two of five elastica parameters, a unique elastica curve exists for the selected target state. When projected as an assumed non-zero principal curvature along the folded transformation region, a curved-crease surface is created as shown in Fig. 3-3C.

Continued projection of the elastica about all reflection planes, that is planes passing through all zig-zag base pattern edges, creates a complete curved-crease pattern as shown in Fig. 3-3D. If all truncations are mapped to the original elastica extrusion, it can be seen that the Arc base pattern and curved crease pattern correspond to a linear elastica extrusion, that is a surface with free edges parallel to the elastica construction plane. The curved-crease Arc surface thus preserves all of the assumptions made in the previous section when adopting a 1D elastica curve to generate an linearly-extruded surface with non-zero principal curvature. Other straight-crease origami base patterns and their curved-crease variants can also be created with this method, however they possess varied free edge conditions that will affect the elastica curve validity. This is demonstrated more clearly in Fig. 3-4A-C with different types of curved free edges created from freeform straight-crease origami base patterns. The impact of these edge conditions will be explored later in this chapter.

3.1.3 Contact Limit State

A related problem to that of exact bending behaviour is that of the compressibility limit of curved-crease origami surfaces. Several definitions for compressibility limit exist in literature [122], but in the context of elastic bending, it is defined here as the state at which adjacent curved panels are first in 'contact' during folding, as shown in Fig. 3-5A. If the curved-crease surface is designed beyond the 'contact limit state', the inverted panel will form an intersection with the non-inverted panel, as shown in Fig. 3-5B. This configuration can be visually designed in a computational environment, but cannot be achieved in physical models, as penetration between panels is not permitted. Therefore, all elastica generated curved-crease origami must be designed within the contact limit state, as shown in Fig. 3-5C.

By using the method proposed in this study, an analytical relationship can be derived for a contact limit state which occurs when the initial rotation Θ of the elastica curve boundary edge is $\pi/2$. Beyond this point, a surface generated from the projection of the elastica curve will have contacting adjacent curved panels. From Equation 2-12, an upper limit of $\Theta = \pi/2$ will limit the m parameter from 0 to 0.5. Fig. 3-6 plots Equation 2-11 and it can be seen that a minimum b/h ratio of 1.1981 must exist for a non-contacting elastica curve with $m < 0.5$ to be constructable from straight-crease base pattern. It is noted that this is only a

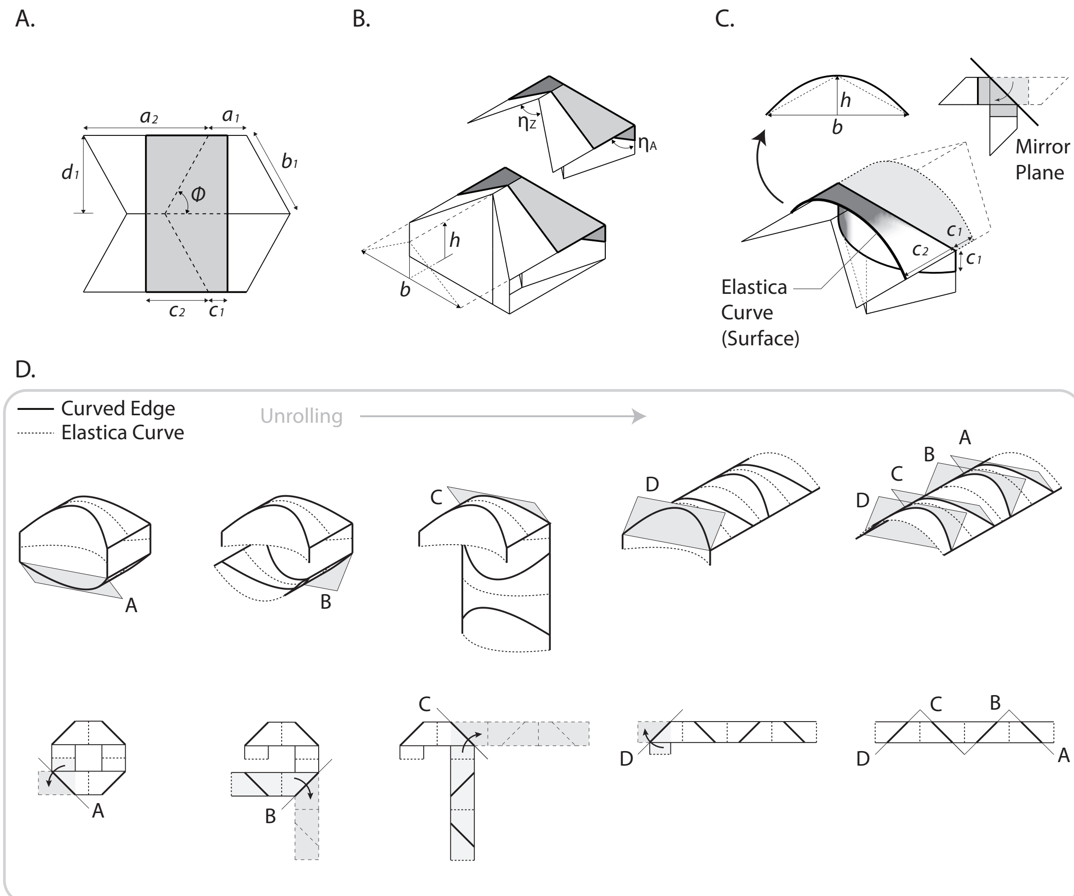

Fig. 3-3 Geometry construction procedures for target folded curved-crease origami. (A) Unfolded base pattern, (B) folded base pattern and design parameters relevant for elastica curve specification, (C) elastica curve projected along transformation region to generate surface with exact non-zero principal curvature, (D) continuous projection of the elastica about all reflection planes and correspondence to linear elastica extrusion.

theoretical limit for elastic bending. It is likely the system could be compressed further after contact occurs, although whether this causes plastic deformation of the constituent panels, reversible elastic deformation, and/or a change of the crease line location and configuration would depend on the material and manufacturing method utilised in practice. This will not be further considered in this thesis.

3.2 Experimental Analysis

3.2.1 Method

To validate the hypothesised curved-crease elastica formulation, prototypes were manufactured and assessed for surface variance. All prototypes were manufactured with a

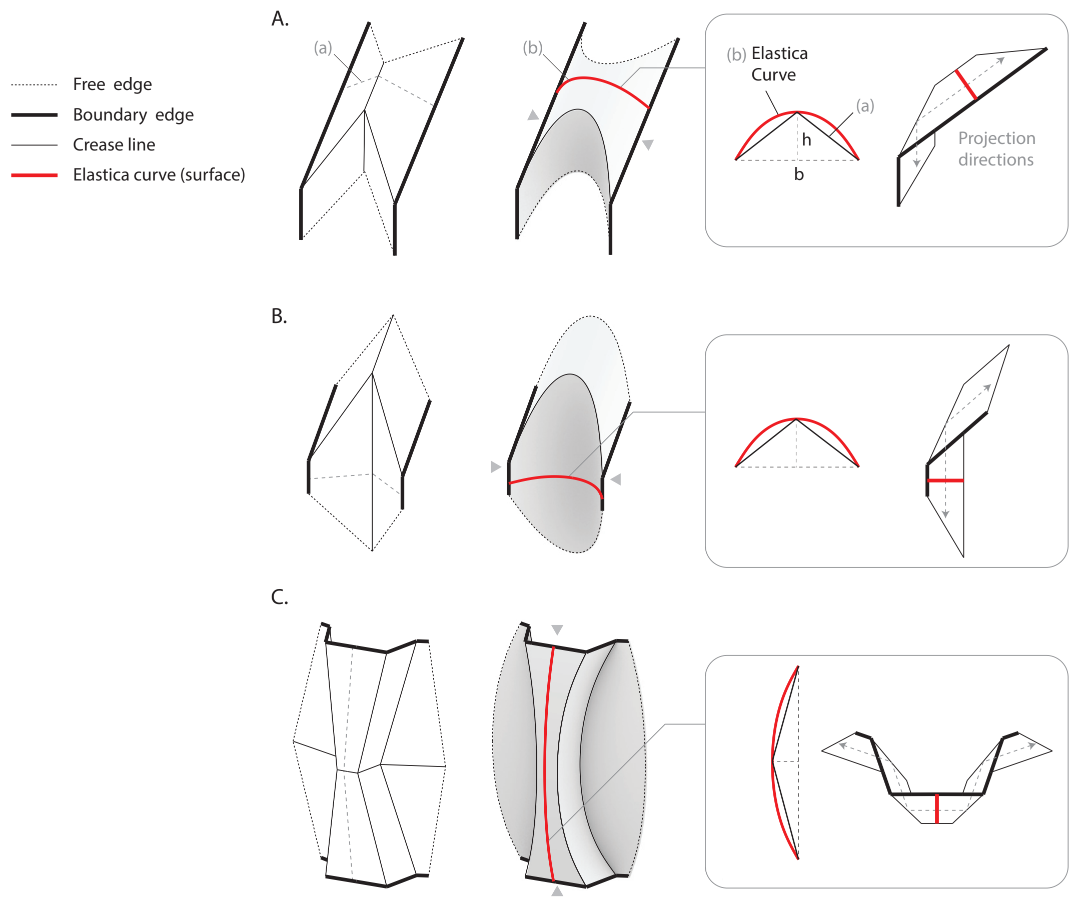

Fig. 3-4 Curved-crease origami creation from freeform straight-crease origami base patterns. From left to right: straight-crease pattern, curved-crease pattern, and elastica curve projection. (A)-(B) Single-crease projection. (C) Continuous projection.

2.0mm thick isotropic polycarbonate sheet, with panels cut separately and joined with a 0.2mm thick Biotex Flax 100g/m^2 2×2 Twill style weave natural fabric hinge. The sheet material achieved the necessary large elastic deformations during folding and the hinge material was selected as one with approximately zero rotational stiffness but with sufficient connectivity and stress transfer to resist the translation displacements and separation of parts during folding.

A series of prototypes were constructed to systematically explore the assumptions of constructing a 3D folded surface from a 1D elastica curve. For all prototypes, a pinned-pinned boundary condition is obtained with a manufactured jig to enforce a fixed boundary width b. Prototypes were then 3D scanned with a FaroArm 3D scan system. The collected mesh data was imported into a Rhino CAD environment and the surface error was measured between the scanned mesh and an 'exact' CAD geometry that incorporated a thickness offset from centreline geometry. A optimisation routine was used to align mesh and geometry, with the Galapagos optimisation solver used to move design geometry along 6-DOF rigid body displacements until a minimum surface error configuration was obtained.

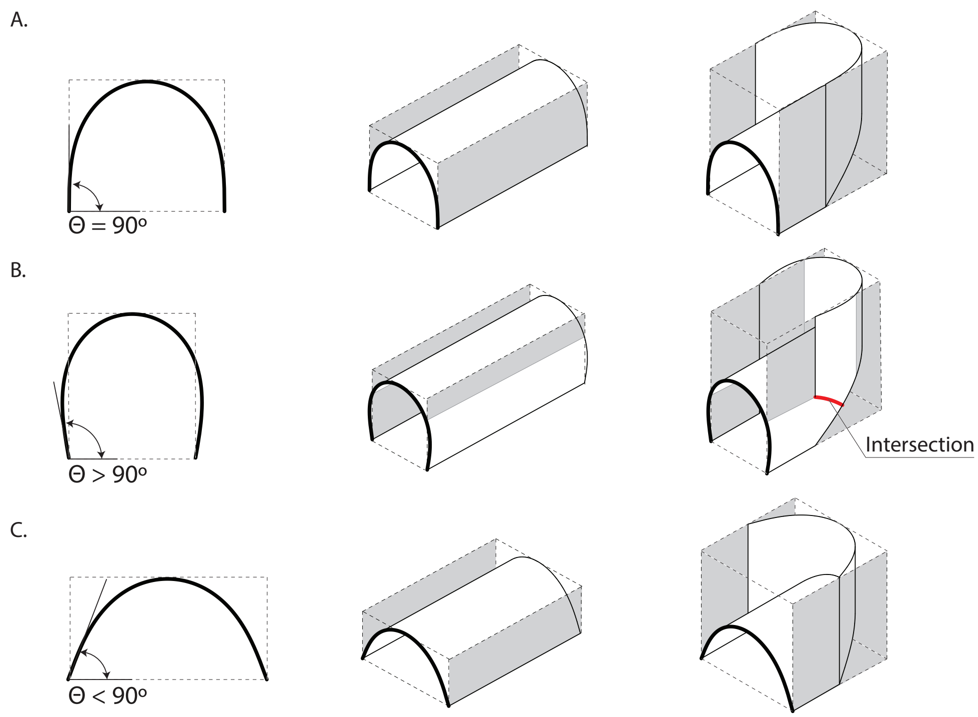

Fig. 3-5 Definition of contact limit state. (A) Illustration of contact limit state, where adjacent curved panels are first in ‘contact’ during folding. (B) Beyond the contact limit state, where curved panels are penetrating each other. (C) Within the contact limit state.

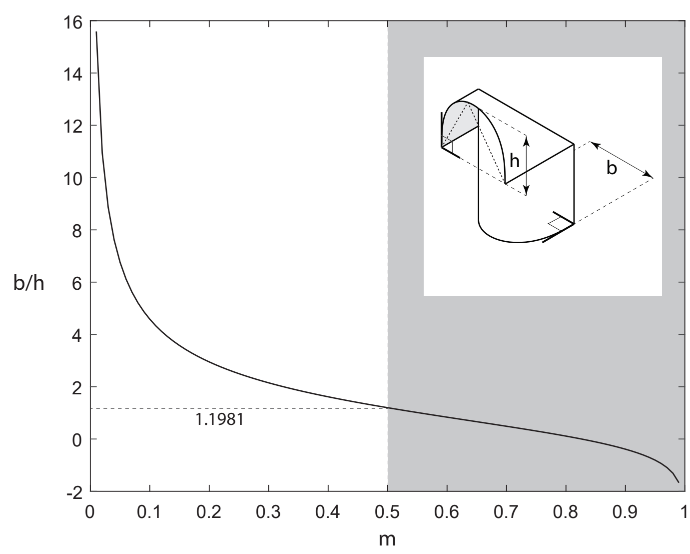

Fig. 3-6 Curved-crease contact limit state. The shaded region indicates the curved-crease design parameters which would cause contact between adjacent curved panels. b/h is the elastica curve design parameter and m is the parameter for elliptic functions.

Detail of the optimisation process is explained as follows. The design surface is first designed in a Rhino-Grasshopper parametric CAD software and sampled with data extraction points. The closest distance between these data extraction points and the scanned mesh surface is then automatically calculated by the software and connected with straight line segments. These lines are here defined as the 'surface error' between design and scanned surfaces. To obtain an optimised alignment between surfaces, the design surface is re-positioned using the Galapagos solver by minimising the average absolute surface error. The optimised alignment can thus be understood as a minimum surface error configuration. The entire work flow is demonstrated more clearly in Fig. 3-7A, summarised in a flowchart shown in Fig. 3-7B, and utilised in a parametric CAD software as shown in Fig. 3-7C.

3.2.1.1 Elastica Surface

The experimental analysis is shown first for a simple 500mm × 500mm polycarbonate sheet, deformed to a width of 350mm as shown in Fig. 3-8A. A corresponding design surface was generated from an elastica curve with parameters $b/L = 350/500 = 0.7$ and extruded along a length of 500mm as shown in Fig. 3-8B. The prototype is scanned and the mesh imported and aligned for minimum surface error as shown in Fig. 3-8C. The design surface is then sampled with approximately 10,000 data extraction points. Error is displayed in Fig. 3-8D as a coloured line between design and scanned points, with a colour legend from green to red for 0 to $+2t$ error and green to blue 0 to $-2t$ error, where $t = 2$mm. Red and blue regions therefore correspond to scanned surface points that lie above and below the simulated surface, respectively, and clear regions correspond to scanned surface points with line lengths approaching zero, that is regions approaching zero error. The overall accuracy of the surface is assessed with an average absolute surface error. This value was calculated as 0.78mm for the current prototype or just under 40% of sheet thickness, which shows the elastica design surface gives a highly accurate prediction of the scanned surface. The majority of error is seen to arise from scanning irregularities that occur at the pinned boundary.

3.2.2 Single-crease Reflection

An initial set of prototypes was constructed to explore the exactitude and validity of a single truncation and reflection of the elastica extrusion, that is a single-crease reflection. One prototype was manufactured from an elastica curve with design parameter $b/L = 0.75$. A second prototype was manufactured with the simplified method proposed by Gattas and You [21], which assumes an inexact curvature, here taken as uniform. Both forms are folded from a 400mm long rectangular sheet, and share design parameters b and h to achieve a common target design volume.

The elastica prototype and surface error is shown in Fig. 3-9A and has an average absolute surface error of 0.88mm, extracted from approximately 20,000 data points. This accuracy is similar to the non-reflected extrusion and confirms that *reflection about the crease line does not distort the bending behaviour*. The pinned boundary and free edge conditions are maintained and again are the main source of scanning error. This finding has offered a strong contribution to the research field of curved-crease origami, which can be

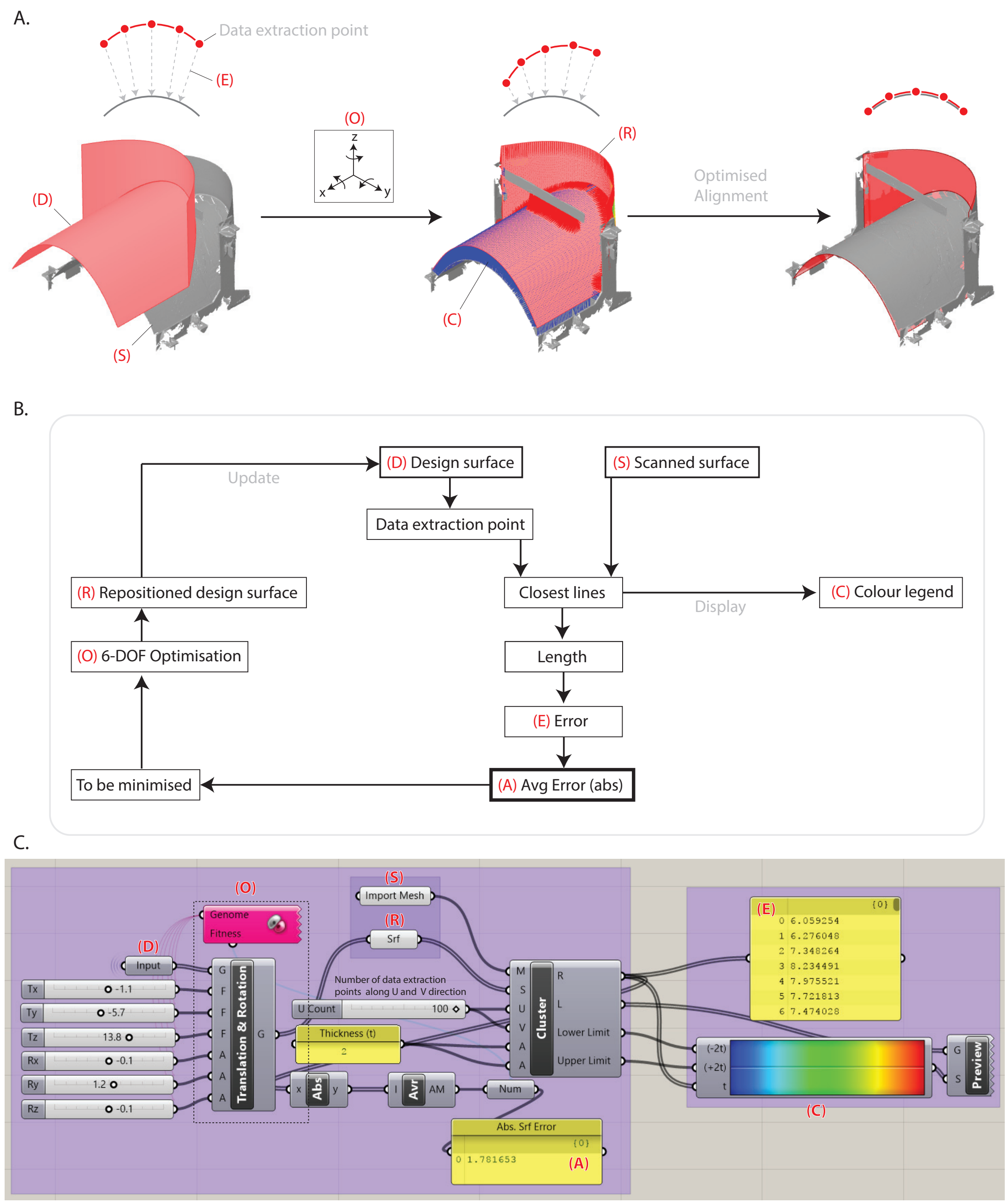

Fig. 3-7 Experimental analysis method. (A) Graphical demonstration of the optimisation process. (B) Flowchart showing the optimisation process. (C) Utilisation of the optimisation process in Rhino-Grasshopper.

applied in many extended origami patterns.

The simplified prototype and surface error is shown in Fig. 3-9B and has an average absolute surface difference of 2.9mm, extracted from approximately 20,000 data points. Interestingly, the minimum surface error occurs near the crease-line region, which implies the crease reflection and enforced developability constraint are able to somewhat enforce the assumed curvature. However away from the crease line, the uniform curvature assumption

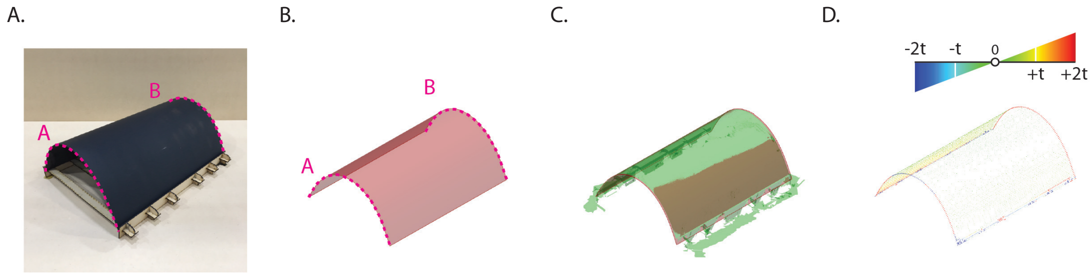

Fig. 3-8 Surface error measurement of a simple deformed sheet, where $b/L = 0.7$. (A) Physical prototype, (B) simulated surface, (C) best-fit scanned surface, and (D) surface error result.

is seen to give a poor approximation of the manufactured surface. Looking at a cross-sectional comparison between manufactured and simplified free-edge profiles in Fig. 3-9C, it can be see that the free edges tend to relax toward an elastica-like minimum bending energy state.

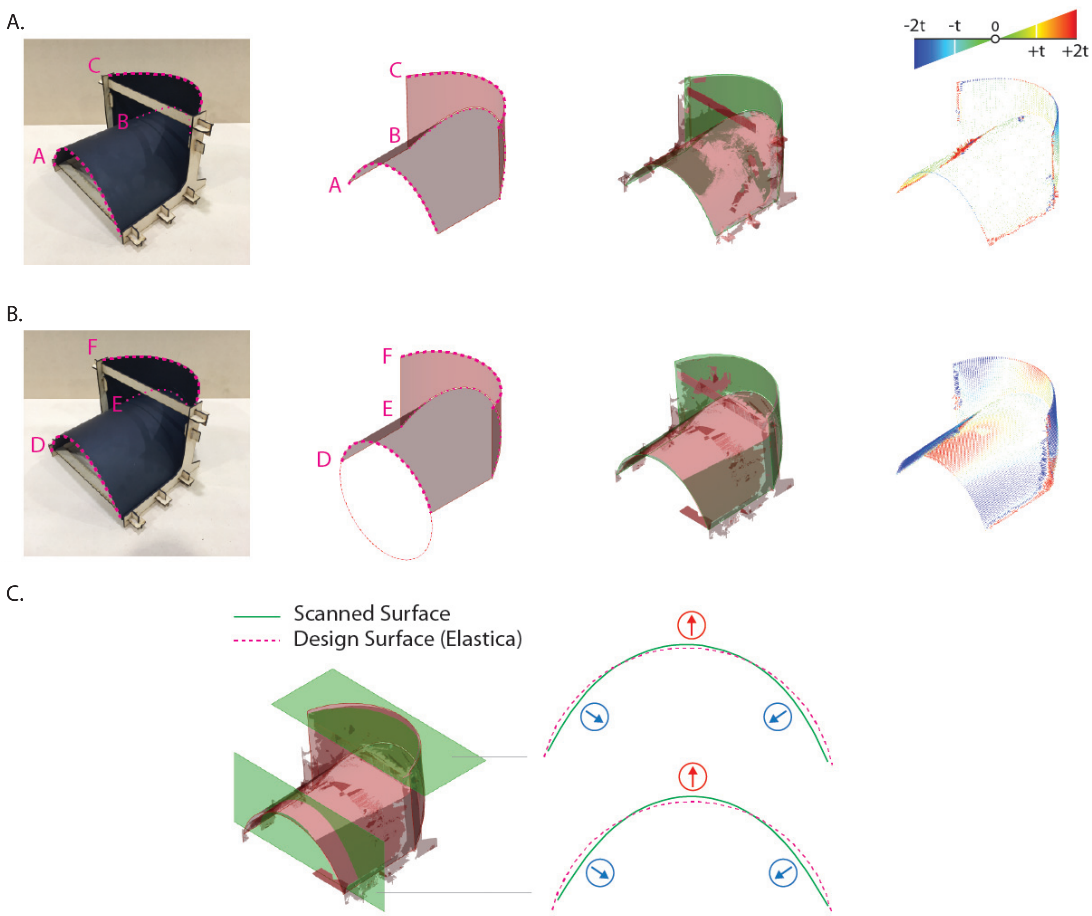

Fig. 3-9 Single-crease reflection of surfaces with (A) exact elastica and (B) inexact (uniform) non-zero principal curvature. From left to right, unfolded planar pattern, simulated folded surface, best-fit scanned surface, and surface error result. (C) Cross section analysis of inexact model.

3.2.3 Constructed State

To examine the accuracy of the geometric construction method, selected geometries are designed and manufactured as shown in Fig. 3-10A-C. Each design is a four-sided tubular geometry corresponding to a constructed curved-crease Arc pattern. They are folded from a 1000mm $\times$ 500mm rectangular polycarbonate sheet with elastica curve design parameters of b/L = 0.75, 0.85, and 0.95.

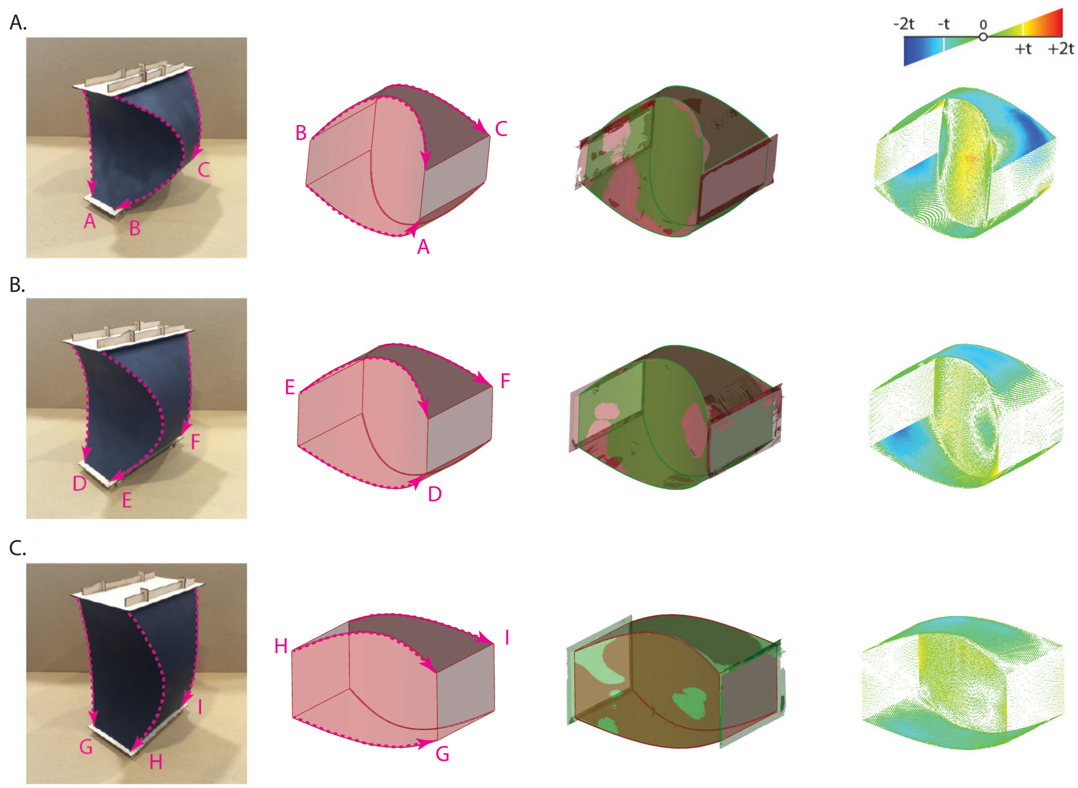

Fig. 3-10 Surface error measurement of constructed state geometries. with elastica curve design parameter b/L of (A) 0.75, (B) 0.85, and (C) 0.95. From left to right, physical prototype, simulated surface, best-fit scanned surface, and surface error measurement result.

The surface error of each model was analysed with approximately 24,000 data extraction points, with results shown in Fig. 3-11. An average absolute surface error of 0.76mm, 0.64mm, 0.63mm was seen for b/L =0.75, 0.85, and 0.95, respectively. The correspondence demonstrates a high degree of design accuracy in terms of 3D surface prediction across a range of elastica profiles, with all average absolute surface differences within half of the 2mm sheet thickness. Regions of maximum and minimum surface error are seen around the boundary region and crease line, attributed primarily to manufacture and assembly defects. The higher errors in steeper elastica design curves are attributed to the same, with curved-crease prototypes with steeper non-zero principal curvatures being more difficult to manufacture and assemble.

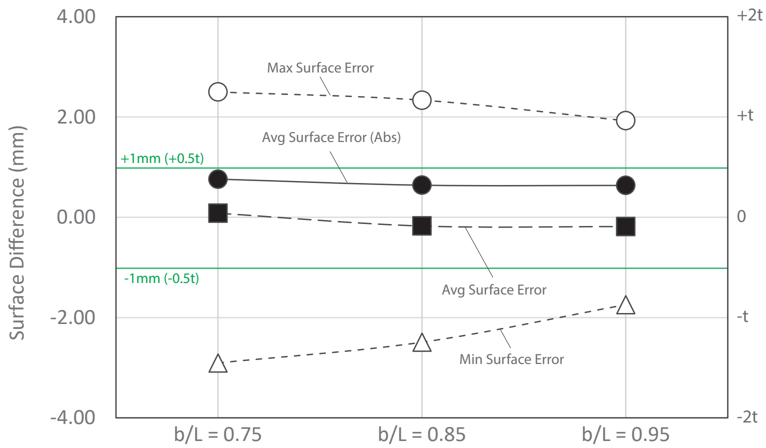

Fig. 3-11 Constructed state surface error measurement results.

3.2.4 Surface Tessellation

The elastica curves used in previous examples are obtained by utilising a pinned-pinned elastica curve. Higher order elastica curves can be obtained [123], however their physical manifestation is highly dependant on constraint conditions. For example, the second mode elastica shape shown in Fig. 3-12A-B is an unstable elastic equilibrium state and one would expect the shape to return back to a first mode configuration. It is theorised though that for folded elastica surfaces, crease lines would provide a means by which to stabilise second or higher mode elastica curves, that is to say that once a higher-order crease line is generated with mirror reflection as shown in Fig. 3-12C, it would prevent a transition back to a lower mode as would be expected in the 1D case. A geometric construction is shown in Fig. 3-12D for a curved-crease Arc pattern that utilises a second-mode elastica curve for generation of the 3D curved surface.

To measure the validity of adopting a second-mode elastica curve as the folded surface curvature, a prototype was manufactured from a 1000mm × 800mm polycarbonate sheet and with $b/L = 0.9$, shown in Fig. 3-13. Surface error measurement was taken from approximately 24,000 data extraction points and showed an average absolute surface difference of 0.66mm, with errors again primarily occurring at the boundary and crease line regions due to manufacture and assembly defects. This good correspondence shows the second-mode elastica curve can be validly assumed as a non-zero principal curvature and mirror reflection can be utilised to stabilise and enable manifestation of higher mode minimum bending energy surfaces.

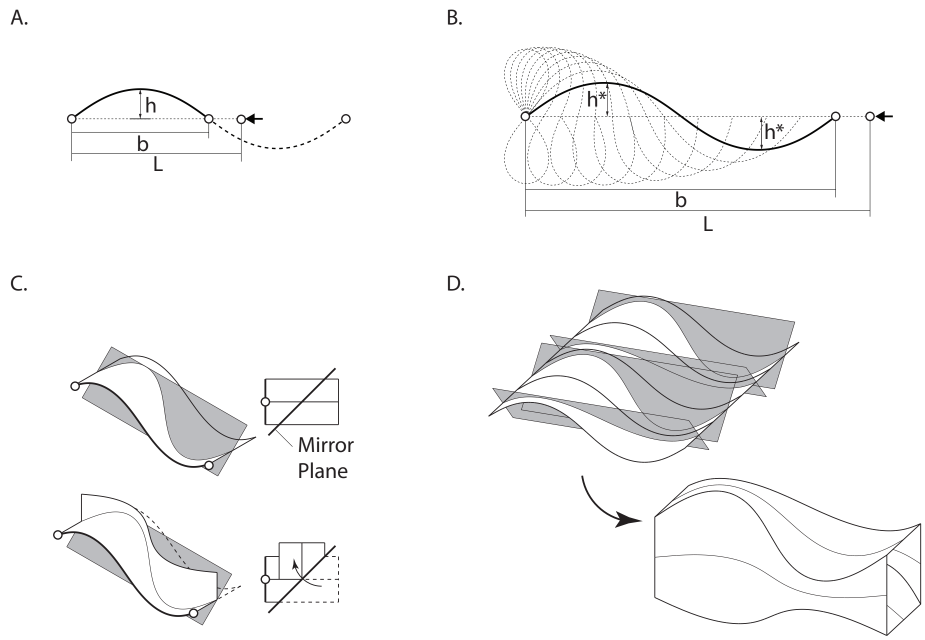

Fig. 3-12 Design procedures of a curved-crease Arc pattern generated with a second-mode elastica curve. (A) First and second mode elastica curve, (B) second-mode elastica geometries, (C) folded unit, and (D) geometric construction.

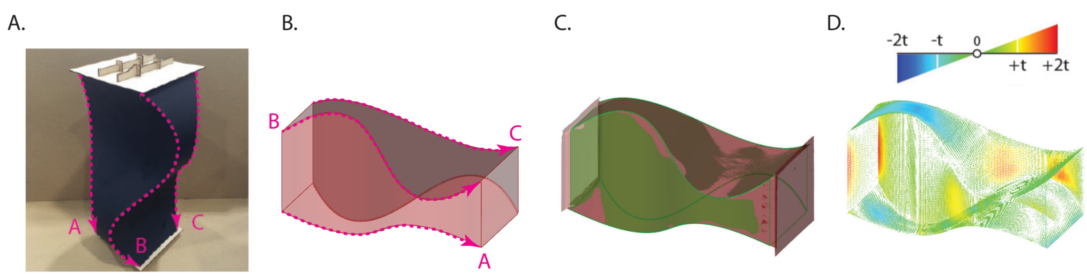

Fig. 3-13 Surface error measurement of second-mode elastica surface. (A) Physical prototype, (B) simulated surface, (C) best-fit scanned surface, (D) surface error measurement result illustration.

3.3 Combined Numerical-elastica Formulations

3.3.1 Folding Sequence

The elastica curve has been demonstrated to give a valid solution for non-zero principal curvature of a specific target folded state. However, in origami-inspired engineering, it is often useful to simulate intermediate folded states, that is the folding sequence of a particular crease pattern. The elastica surface generation method cannot be used to generate valid intermediate states as the reflection planes used to generate a developability condition, and the boundary parameters used to generate the elastica curve are only coincident in the target state. However, many numerical methods exist to simulate the folding behaviour of a known curved-crease surface and so an investigation was conducted to assess the extent to which a numerical folding simulation was able to accurately model the intermediate folded states of an elastica generated origami surface.

To simulate a folding sequence, a curved-crease origami pattern is constructed with a 'Miura' base pattern and elastica curve as shown in Fig. 3-14A-B. The constructed surface is discretised into planar quadrangle strips to give a rigid-foldable piecewise assembly of straight-crease origami that approximates the generated elastica form, shown in Fig. 3-14C. The folding motion of the piecewise assembly can then be simply simulated by numerically varying a common edge angle η_A [73], as shown in Fig. 3-14D. Increasing the number of discrete rulings gives a stronger approximation of the initial target design surface, with a fold simulation consisting of quasi-infinite rulings shown in Fig. 3-14E. This method is selected for investigation as it is a computationally inexpensive and highly inexact; component panels are made planar and no rotational stiffness is imparted to crease lines created during discretisation, so no bending behaviour energy exists in the system.

For practicality of testing, a physical prototype was constructed with two curved-crease Miura units joined together about a mirror plane as shown in Fig. 3-14D-E. Each unit was folded from a 500mm $\times$ 500mm polycarbonate sheet with elastica curve design parameters of $b/L = 0.7$. The prototype was scanned at four intermediate folded states, at an edge angle $\eta_A = 160^o, 140^o, 120^o, 100^o$, and at the target state with $\eta_A = 90^o$.

The surface error of each folded state was analysed with approximately 24,000 data extraction points as shown in Fig. 3-15, with results plotted in Fig. 3-16. Errors are seen to increase in progressive states, with an average absolute surface error of 0.50mm, 0.48mm, 0.69mm, 0.94mm, 1.27mm seen for $\eta_A = 160^o$, 140^o, 120^o, 100^o, 90^o, respectively. The first three intermediate states show good correspondence between the numerical model and physical prototype, with the majority of errors seen around boundary regions in a similar manner to previous surface comparisons. This shows that numerical simulations can provide a good prediction of the surface geometry of intermediate folded states, even when simplified to neglecting bending energy considerations. The validity of elastica design mechanism behaviours will be investigated in depth in Chapter 4.

Errors are seen to jump in the fourth intermediate state and the final target state, with the latter having an error that exceeds half of 2mm material thickness. Inspection of the error location shows it occurred at the connected edges of the Miura units, highlighted in Fig. 3-15E. The primary source of error was initially thought to be from manufacturing defects occurring due to the increased difficulty of attaching a fabric hinge to these non-developable edges. However, closer inspection suggested that the non-zero principal curvature of the surface no longer corresponded to the assumed analytical elastica curve in these edge regions. The next study was conducted to investigate this behaviour, described in the following section.

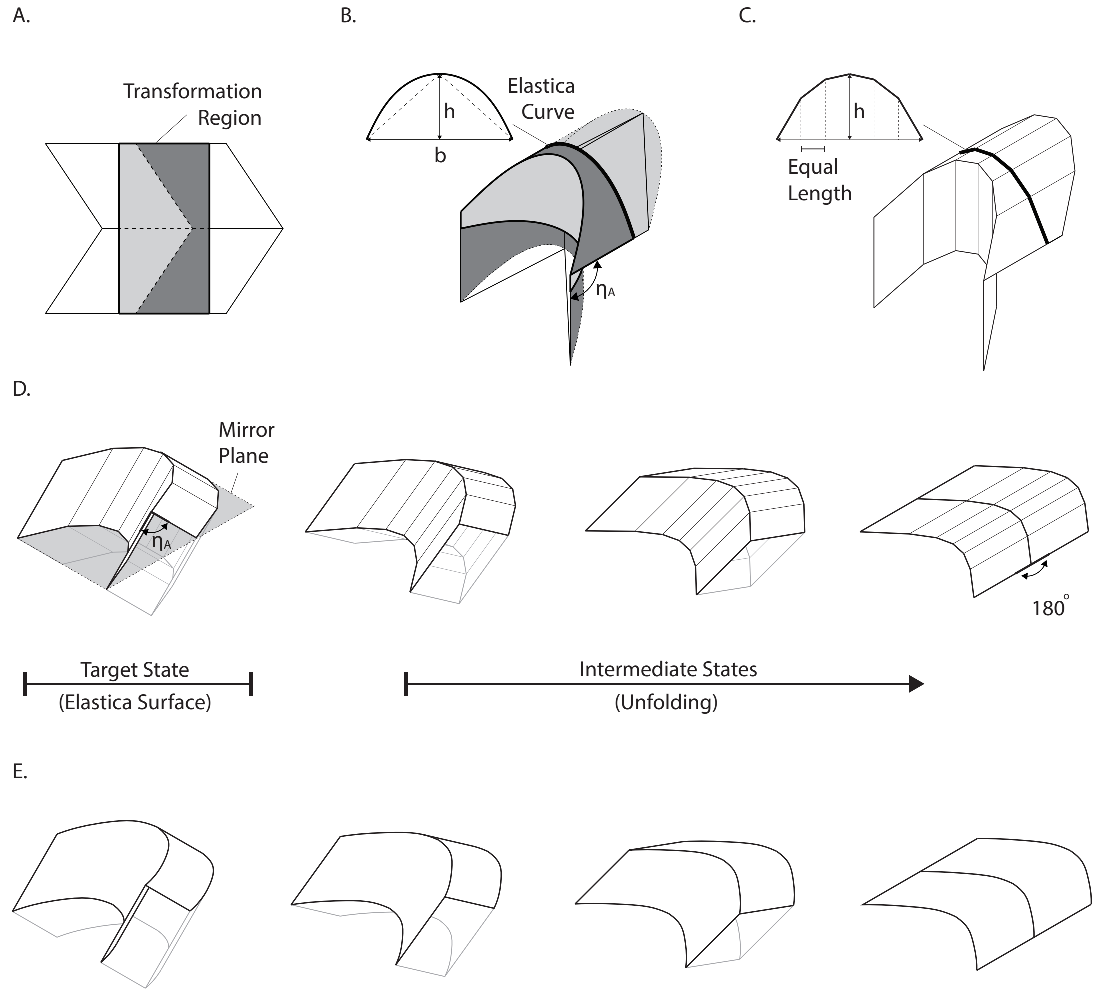

Fig. 3-14 Numerical simulation of folding sequence of elastica generated surface. (A) Base unfolded Miura pattern, (B) curved-crease transformation, (C) rigid-foldable approximation of curved-crease surface, (D) numerical simulation of folding sequence of the rigid-foldable assembly, and (E) numerical simulation of folding sequence of a quasi-infinite rigid-foldable assembly.

3.3.2 Free Edge Effect

For curved-crease models studied in Sections 3.1 and 3.2, the constructed elastica surfaces corresponded exactly to a linear extrusion of a 1D elastica solution, that is the ends, or ‘free edges’, lay in a plane parallel to the elastica construction plane. It was therefore assumed that the free edges of the 3D shell did not distort the bending behaviour of the elastica surface. However, this assumption is thought to be invalid for elastica surfaces generated on the Miura surface of the previous section, or for other base patterns which possess a non-parallel free edge. To explore the effect of the free edge, two elastica surface geometries were generated on a base pattern with non-parallel free edges.

The first investigated surface consists of the component panels of the curved-crease Miura pattern described in the previous section, shown in Fig. 3-17A. These surfaces can

Fig. 3-15 Surface error measurement of numerical folding simulation. From left to right: physical prototype, simulated surface, best-fit scanned surface, and surface error measurement. Folded states generated with an the edge angle η_A of (A) 160^o, (B) 140^o,(C) 120^o,(D) 100^o, and (E) target state 90^o.

be understood as a linear elastica extrusion with free edges that lie in parallel planes that are inclined or 'skewed' relative to the elastica construction plane, as shown in Fig. 3-17B. The surface error measurement result shown in Fig. 3-18A demonstrates a surface variation, with a flatter profile on the skew edge inclined towards the surface centreline and a steeper profile on the skew edge inclined away from the centreline. This variation is shown more

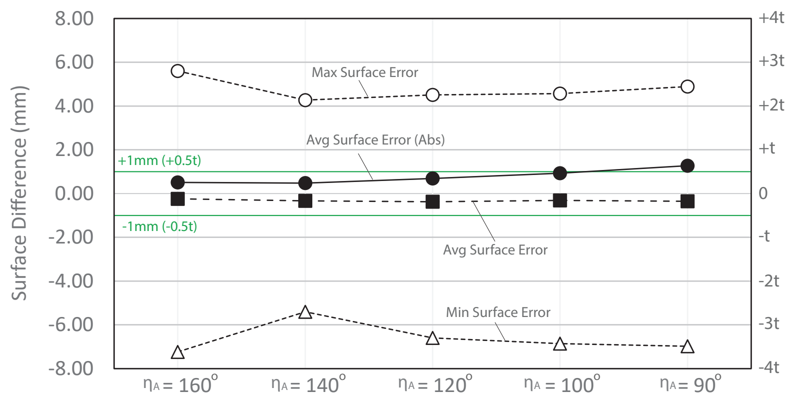

Fig. 3-16 Folded state surface error measurement results.

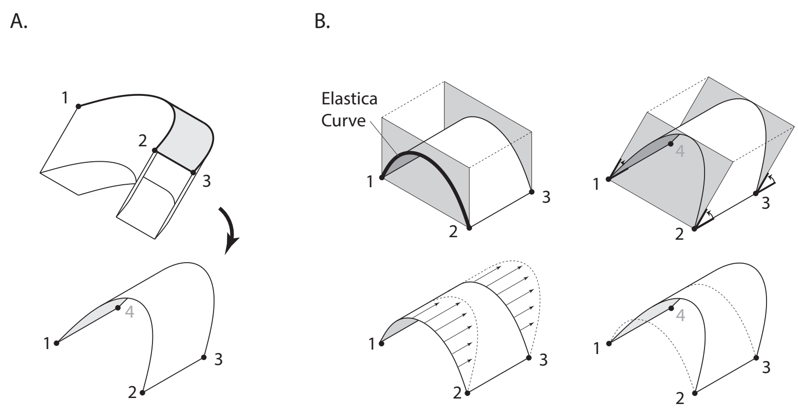

Fig. 3-17 Surface geometry with skewed free edges. (A) Curved-crease Miura pattern geometry and (B) corresponding linear elastica curve extrusion with skewed edges lying in parallel inclined planes.

clearly with a cross-sectional comparison in Fig. 3-18B.

To verify the source of the error originates from the elastica assumption and not the prototype measurement, a numerical finite element simulation was also created to compare with the physical prototype. The simulation was created in the commercial software Abaqus. A static non-linear large displacement method was used. Displacement-control was applied on two rigid plates highlighted in Fig. 3-19A which compress the edges of a deformable shell element to a target displacement. The surface was meshed with S4 shell elements with global size set at 5mm following a convergence study. Material properties were set as a t = 2mm thick elastic isotropic polycarbonate with Young's modulus E = 2400MPa and Poisson's ratio ν = 0.37. Deformed mesh was imported into Rhino as point data based on the nodal displacement data of the underformed and deformed mesh. These points were then patched to a continuous surface using Rhino-Grasshopper, as shown in Fig. 3-19B. This enabled the surface error analysis to be conducted between numerical and physical surfaces. Results of this comparison are shown in Fig. 3-20 and it can be seen that the numerical and physical behaviours have a much better correspondence. Average

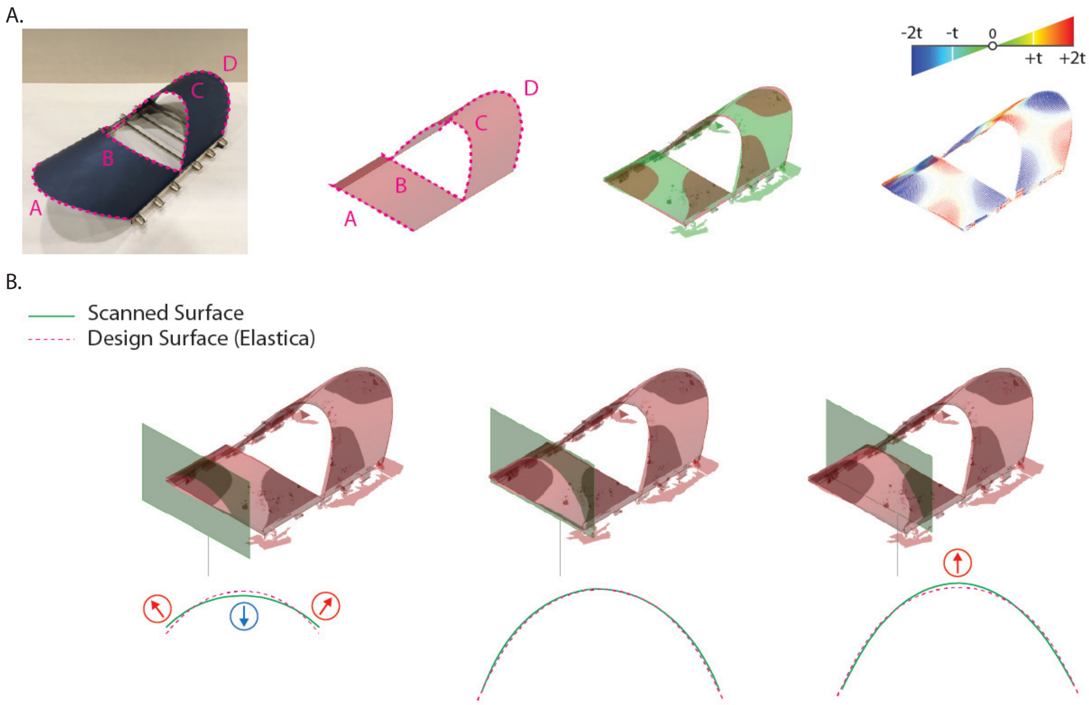

Fig. 3-18 Surface error measurement between elastica generated surface and physical prototype with skewed edges. (A) From left to right: physical prototype, simulated surface, best-fit scanned surface, and surface error measurement result illustration. (B) Cross-sectional comparison.

absolute surface error was 3.37mm for the elastica surface comparison and only 0.78mm for the numerical surface comparison, which shows the elastica curve is an invalid representation of non-zero principal surface curvature in skewed edge regions of 3D surfaces. It also confirms the free edge distortion is the likely cause of the error observed in the previous section.

A second surface was investigated to understand the effect of free edge distortion in a reflected curved-crease origami surface. A single-crease model was constructed from an Arc-Miura base pattern, with skew edges and geometric construction procedure as shown in Fig. 3-21A-B, respectively. Prototype parameters were for a 400mm long arc length, an extrusion length of 400mm, and an elastica curve design parameter of $b/L = 0.75$. The surface error measurement result is shown in Fig. 3-22A and demonstrates a reasonable correspondence between the design and prototype surfaces, with an average absolute surface error of 1.1mm. Similar to that seen previously for the inexact uniform curvature model, low error is seen in the crease line region, with the crease acting to enforce the assumed elastica principal curvature. Larger errors of up to approximately 3.1mm are seen towards the skewed free edge, shown more clearly in cross section in Fig. 3-22B. A numerical finite element simulation was again used to check accuracy of the physical prototype, however a hybrid surface generation approach was used whereby a rectangular sheet was numerically deformed to the target width and then geometrically reflected about a plane, shown in Fig. 3-23. This prevented an assumed crease line from altering the minimum bending energy

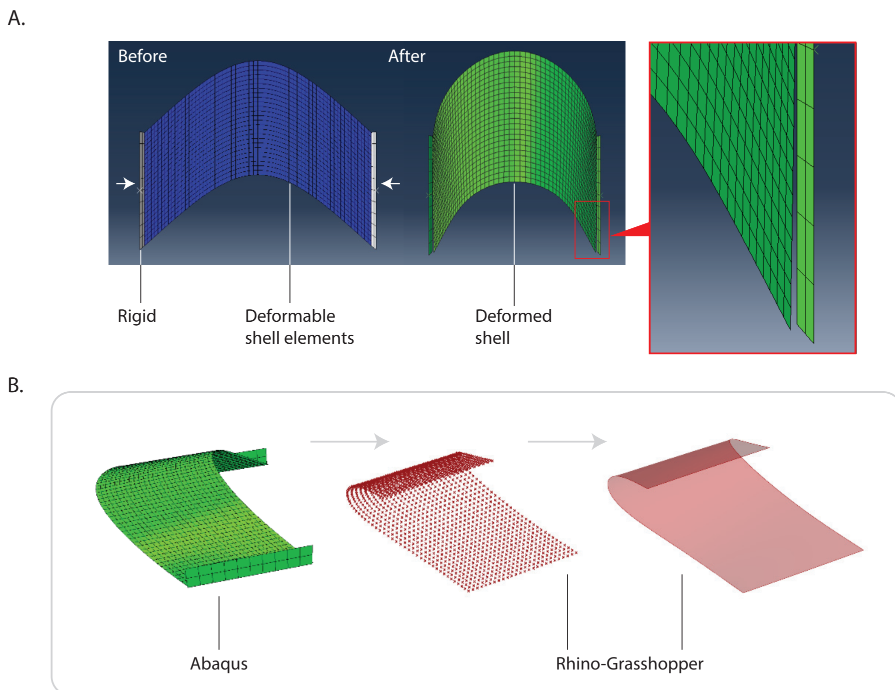

Fig. 3-19 FE simulation method for a skewed shell. (A) Undeformed and deformed mesh in the Abaqus software. (B) Surface recreation from Abaqus to Rhino-Grasshopper using nodal data.

configuration. The average absolute surface error decreased to 0.98mm and the accuracy of the surface is seen to have improved both at crease line and free edge locations, shown more clearly in cross section in Fig. 3-23C. This improvement indicates that a Arc-Miura patten design with eliminated free edge effect has been achieved, as the impact of the free edge effect is localised and does not influence the mirror reflection region. An initial investigation of non-localised free edge effect was conducted, described in the following section.

3.4 Limitation of the Proposed Modelling Method

3.4.1 Motivation

A range of elastica solutions exists for other boundary constraint conditions and bending stiffness (EI). In this final study, elastica curves with non-uniform bending stiffness caused by the shape variation (I) are investigated. Two 500mm long flat strips are designed with a 2.0mm thick isotropic polycarbonate sheet. They are Type 1 (Fig. 3-24A) and Type 2 (Fig. 3-24B) strip, corresponding to the strip with wider and narrower mid-span region, respectively. To compare their bending deformations with elastica curves derived from a uniform bending stiffness, physical strips are bent with one support moved-in horizontally 10% of the length for each sub-deformation, up to a total displacement of 100%.

Comparison results are shown in Fig. 3-24A-B for Type 1 and Type 2 strip, respec-

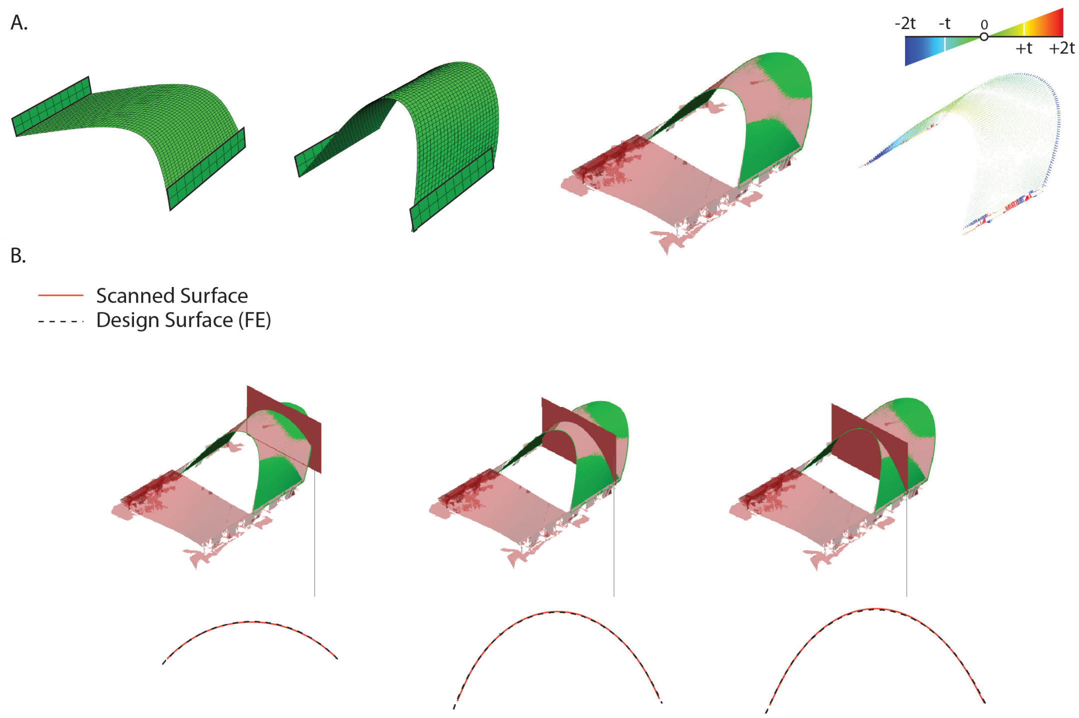

Fig. 3-20 Surface error measurement between finite element simulation and physical prototype with skewed edges. (a) From left to right: undeformed FE model, deformed FE model, best-fit scanned surface and surface error measurement result illustration. (b) Cross-sectional comparison.

tively. It can be seen that deformations of Type 1 strip are above-below-above elastica curves with a uniform bending stiffness, because it has a flexible-stiff-flexible feature; deformations of Type 2 strip are below-above-below elastica curves with a uniform bending stiffness, because it has a stiff-flexible-stiff feature. As elastica curves are purely geometric relations, bending deformations of Type 1 and Type 2 strip can arise in other elastically-bent materials. If bending deformations of Type 1 and Type 2 strip can be accurately captured, further investigation is needed to examine whether they can be adopted as the non-zero principle curvature design of elastically-bent curved-crease origami.

3.4.2 Elastica Surface with Non-uniform Bending Stiffness

To examine the suitability of the geometric construction method developed in Section 3.1 with other elastica solutions, two elastica surfaces are selected to be the 'base' non-reflected shell. They are Type 1 and 2 shell, designed by purely enlarging the width of Type 1 and 2 strip, respectively, and have a curve design parameter $b/L = 0.75$, as shown in Fig. 3-25A-B, respectively. Note that bending deformations were simulated using the numerical method described in Section 3.3.2; a good correspondence between strip and shell again confirms that the shape of elastica is purely a geometric relation.

The surface error of Type 1 and 2 shell was analysed with approximately 140,000 data points, with result shown in Fig. 3-26A-B, respectively. An average absolute surface

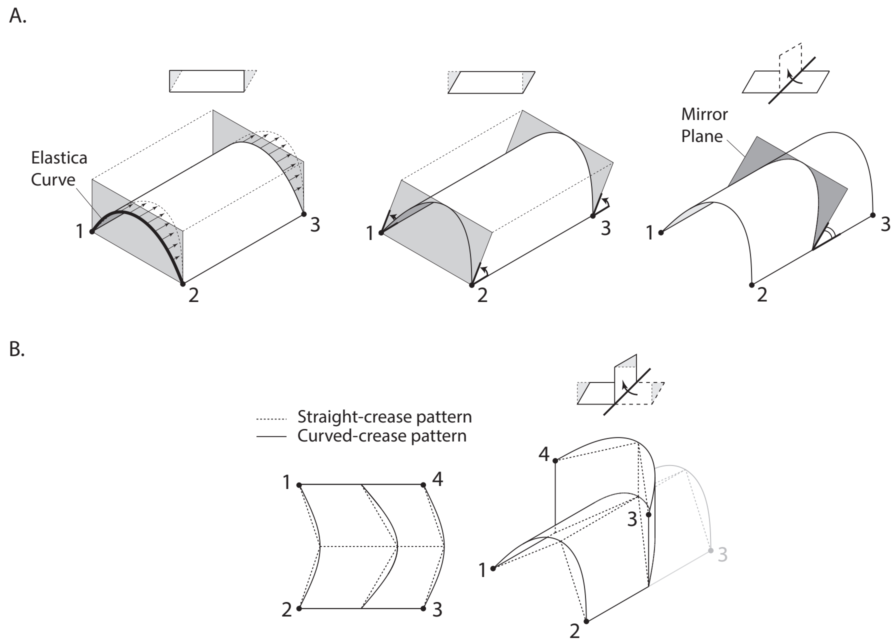

Fig. 3-21 Curved-crease Arc-Miura pattern geometry with skewed free edges. (A) Linear elastica curve extrusion with inclined planes and mirror reflection plane and (B) corresponding unfolded and folded configurations.

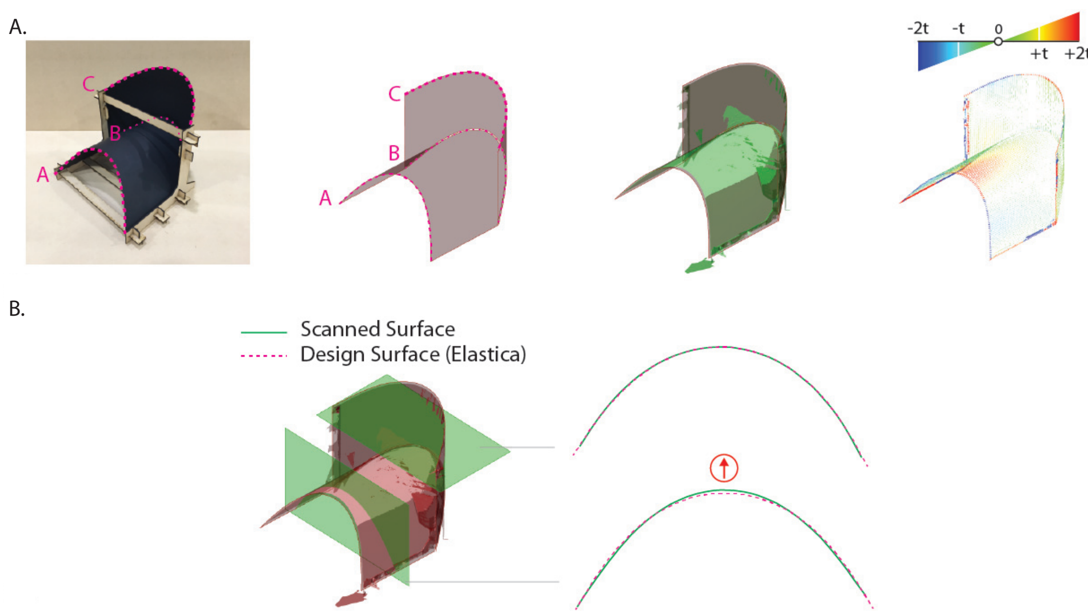

Fig. 3-22 Surface error measurement of single-crease reflection free edge effect. (A) From left to right: physical prototype, simulated surface, best-fit scanned surface, and surface error measurement result illustration. (B) Cross-sectional comparison.

error of 0.27mm and 0.79mm was seen for Type 1 and Type 2 shell, respectively. The correspondence demonstrates a high degree of simulation accuracy in terms of 3D surface prediction with all average absolute surface differences within half of the 2mm thickness.

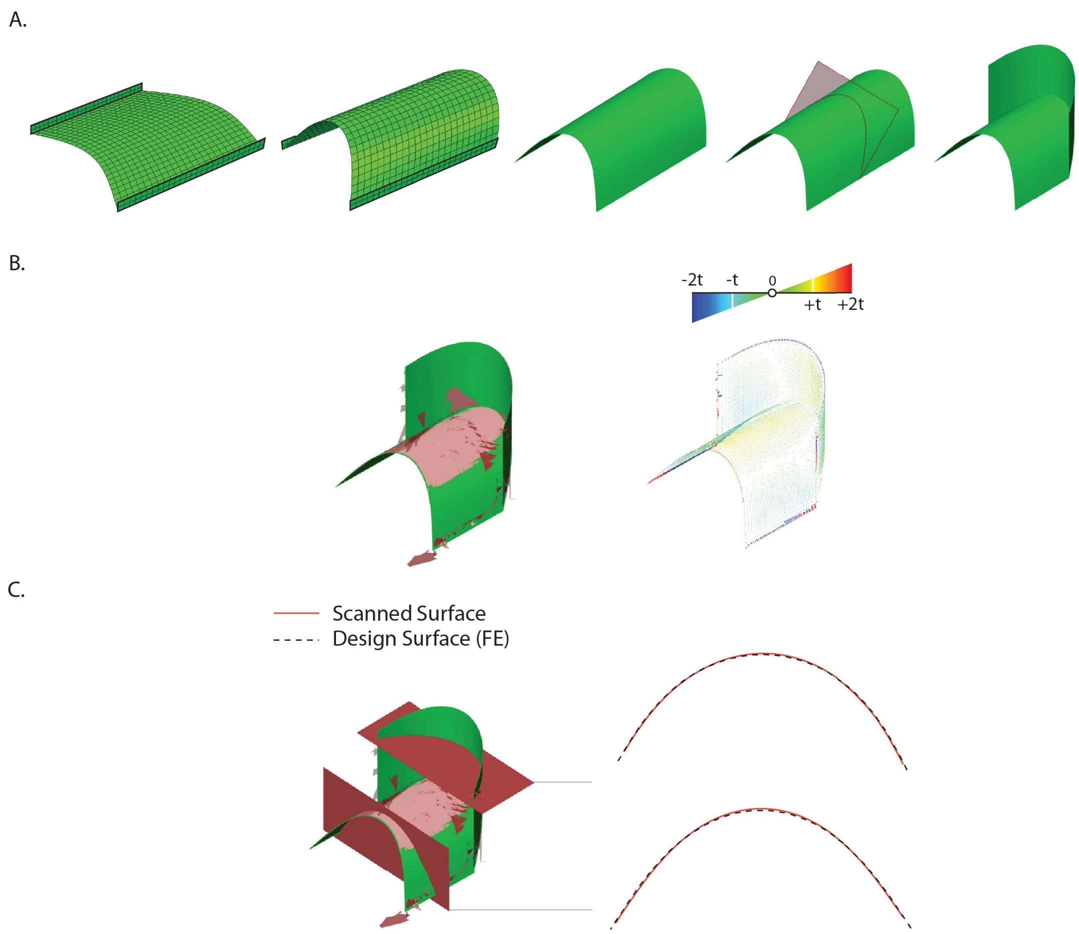

Fig. 3-23 FE simulation of curved-crease origami. (A) Design procedure, from left of right: undeformed FE model, deformed FE model, exported surface, intersecting mirror reflection plane, reflected curved-crease component. (B) Surface error measurement result illustration. (C) Cross-sectional comparison.

Higher errors are seen around boundary regions, attributed primarily to manufacture and assembly defects. The good correspondence has confirmed that both numerical-elastica profiles are reliable, hence can be used for examining the interaction with the introduced origami developability constraint, discussed in the following section.

3.4.3 Non-localised Free Edge Effect

To explore the bending behaviour of curved-crease origami with a non-uniform bending stiffness, four hybrid curved-crease origami surfaces were created from the Type 1 and 2 shell using the method described in Section 3.3.2, including:

- *T1 CC Origami I*: Type 1 shell with mirror plane intersected about the free edge, as shown in Fig. 3-27A.
- *T1 CC Origami II*: Type 1 shell with mirror plane intersected about boundary edges,

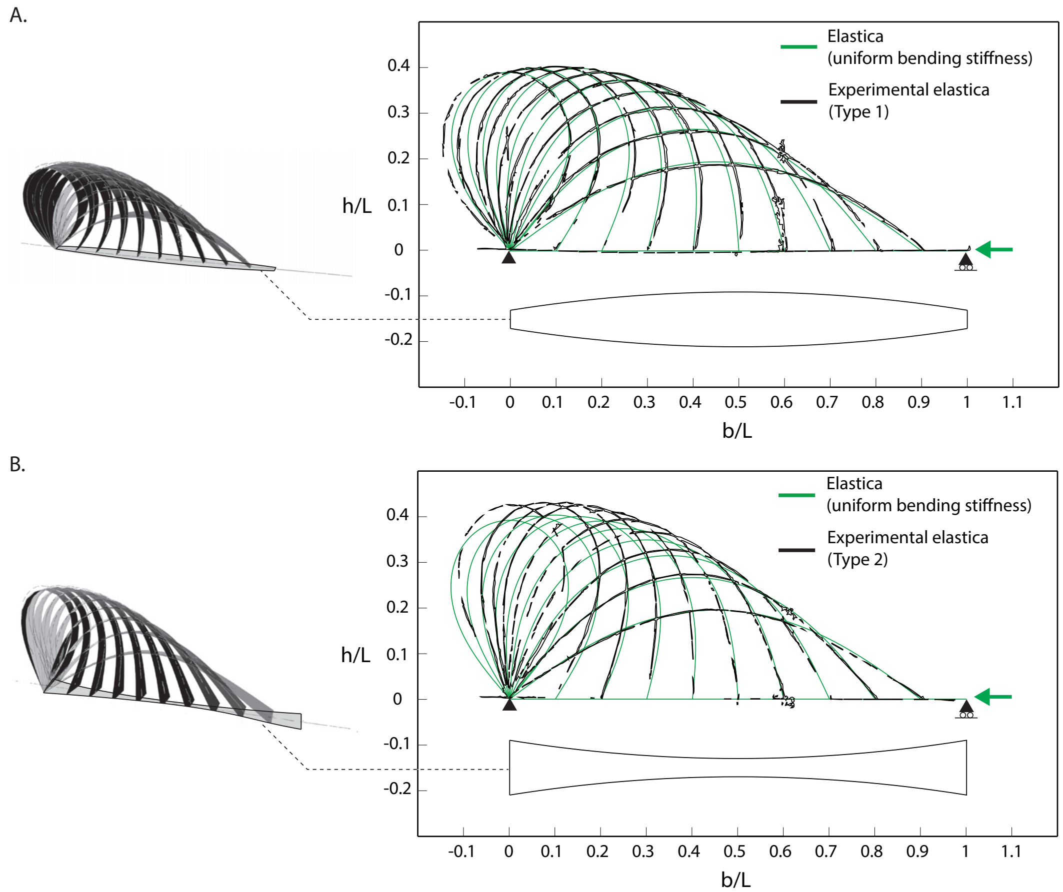

Fig. 3-24 Bending deformations of (A) Type 1 and (B) Type 2 strip. Green lines are analytical elastica curves derived from uniform bending stiffness and black lines are scanned results obtained from manually tracing deformations of strips with non-uniform width.

as shown in Fig. 3-27B.

- *T2 CC Origami I*: Type 2 shell with mirror plane intersected about the free edge, as shown in Fig. 3-27C.
- *T2 CC Origami II*: Type 1 shell with mirror plane intersected about boundary edges, as shown in Fig. 3-27D.

The surface error of each design surface was analysed with approximately 140,000 data points, as shown in Fig. 3-28-3-29 and summarised in Fig. 3-30. The impact of free edge effect are clearly seen in scan results, indicate that design geometries were only capable of capturing the approximate shape of manufactured prototypes. This is shown more clearly in a cross section analysis, as shown in Fig. 3-31. An average absolute surface error of 4.67mm, 1.51mm, 1.44mm, and 1.68mm of the material thickness are seen for T1 CC Origami I, T1 CC Origami II, T2 CC Origami I, and T2 CC Origami II, respectively. These errors exceed half of the material thickness, so distortion is confirmed to have occurred. The source of error is attributed to the developability constraint imparted on the elastica surface, which distort the surface minimum bending behaviour. That is to say, the 2D elastica is no

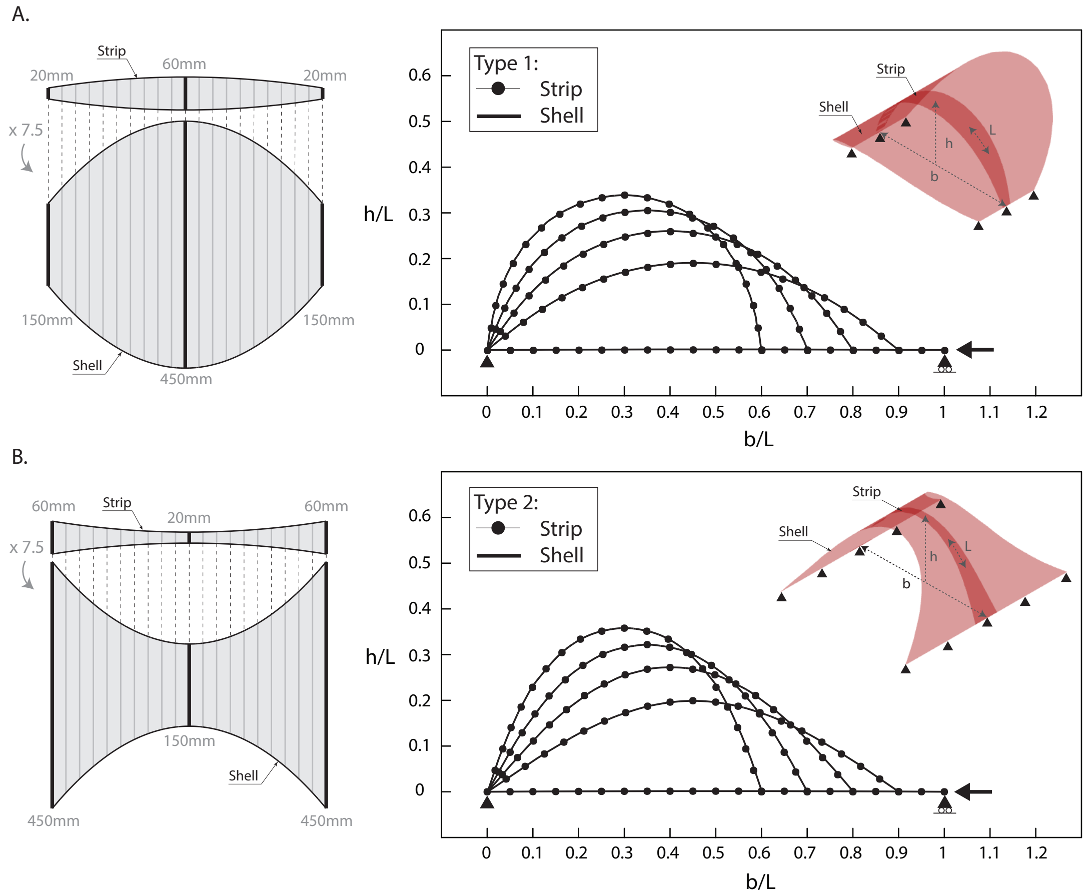

Fig. 3-25 Simulation result of numerical-elastica. (A) Type 1 and (B) Type 2 geometries.

longer a valid representation of the non-zero principal curvature of the curved-crease surface. Based on qualitative observations of the free edge effect seen in this chapter, a simple criteria is proposed for the distortion of elastica surface curved-crease origami, summarised as follows:

- Distortion will not occur if the curved-crease pattern has a rectangular sheet boundary. The folded form can be considered as a reflected elastica curve extrusion, where the reflection does not distort the bending behaviour.
- *Localised distortion* can be achieved if the curved-crease pattern with skewed free edges is designed from a rectangular sheet, hence the folded form can be remapped to a linear elastica extrusion with bending stiffness and boundary condition preserved as per the original elastica derivation.
- *Non-localised distortion* will occur if the curve-crease pattern has a non-uniform boundary which cannot be reconfigured to a rectangular sheet. It involves the use of elastica curve derived from a specific combination of shell geometry (with a non-uniform bending stiffness) and boundary condition, hence the introduced developability constraint will distort the bending behaviour of the non-reflected elastica surface.

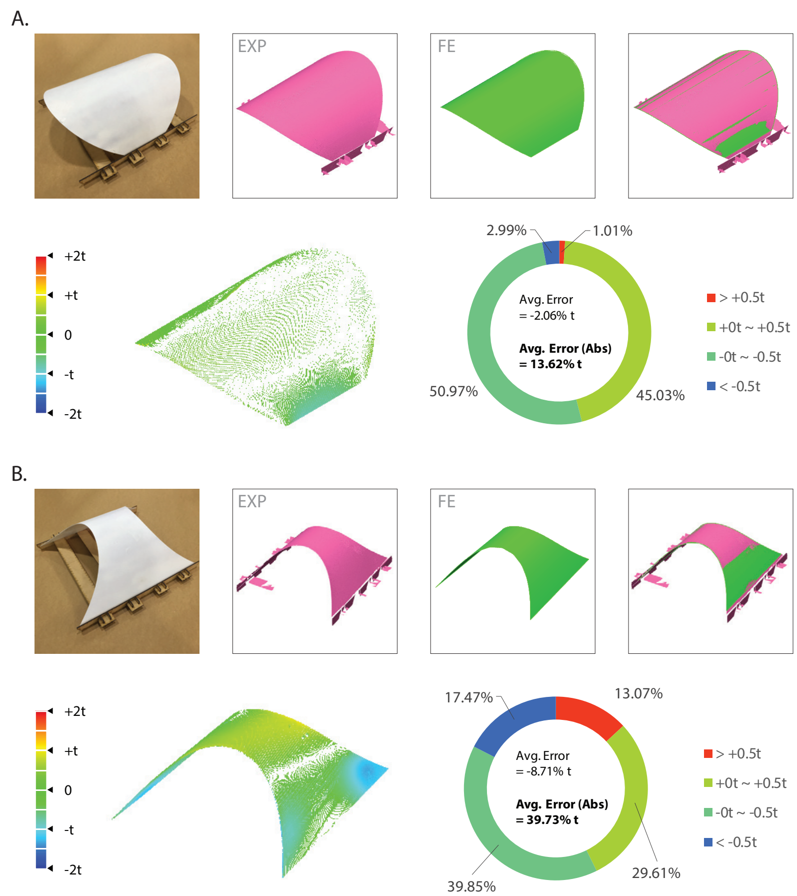

Fig. 3-26 Surface error measurement of shells. (A) Type 1. (B) Type 2. Each sub-figure includes physical prototype, scanned mesh surface, simulated surface, best-fit scanned surface, correspondence result illustration, and result data.

Together, it is concluded that the proposed curved-crease modelling method is limited to the utilisation of a specific type of elastica solution for near-exact representation of sheet elastic bending behaviours, that is elastica with a uniform bending stiffness and pinned-pinned boundary condition. Extrusion and reflection of other elastica solutions can lead to a non-localised free edge effect.

3.5 Conclusion

This study has presented an analytical geometric construction method for curved-crease origami that concisely and accurately captures curvature and developability constraints. Developability is preserved without the need for surface discretisation by projection and reflection of an assumed 2D elastica profile about a known 3D straight-crease origami surface. The use of an elastica curve for non-zero principal surface curvature gives a near-exact analytical representation of 3D curved-crease origami surfaces that are

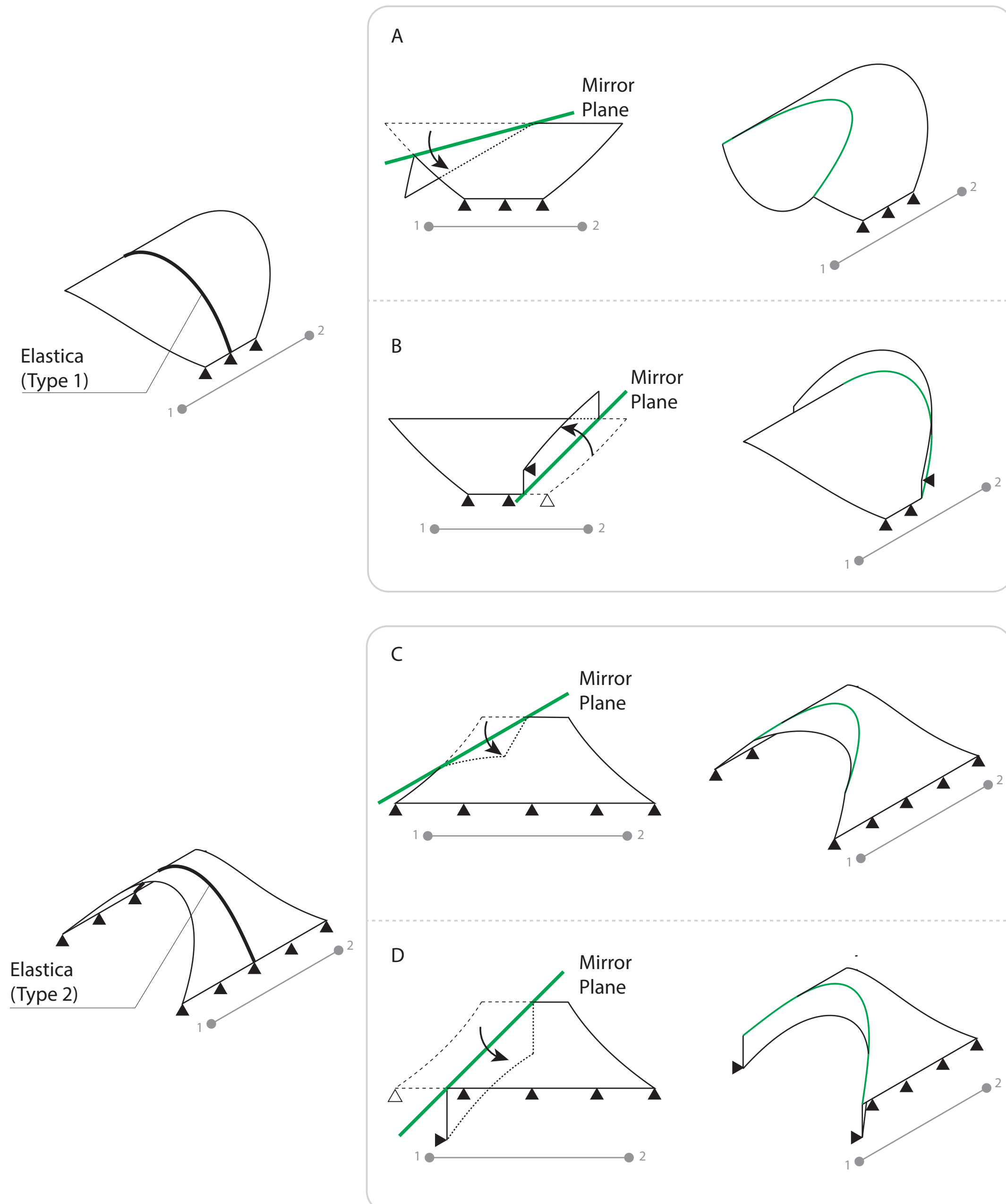

Fig. 3-27 Design procedures of curved-crease origami using Type 1 and 2 elastica curves. (A) T1 CC Origami I. (B) T1 CC Origami II. (C) T2 CC Origami I. (D) T2 CC Origami II.

elastically-bent and have boundary conditions consistent with the utilised elastica solution. Extensions of the method were explored and included identification of the compressibility limit of curved-crease surfaces; construction of stable curved-crease origami surfaces from higher-order elastica profiles; and demonstration that a numerical simulation of the folding motion of a discretised curved-crease surface gave a good prediction of behaviour of a physical prototype over a full range of motion. Limitations of the method are in modelling

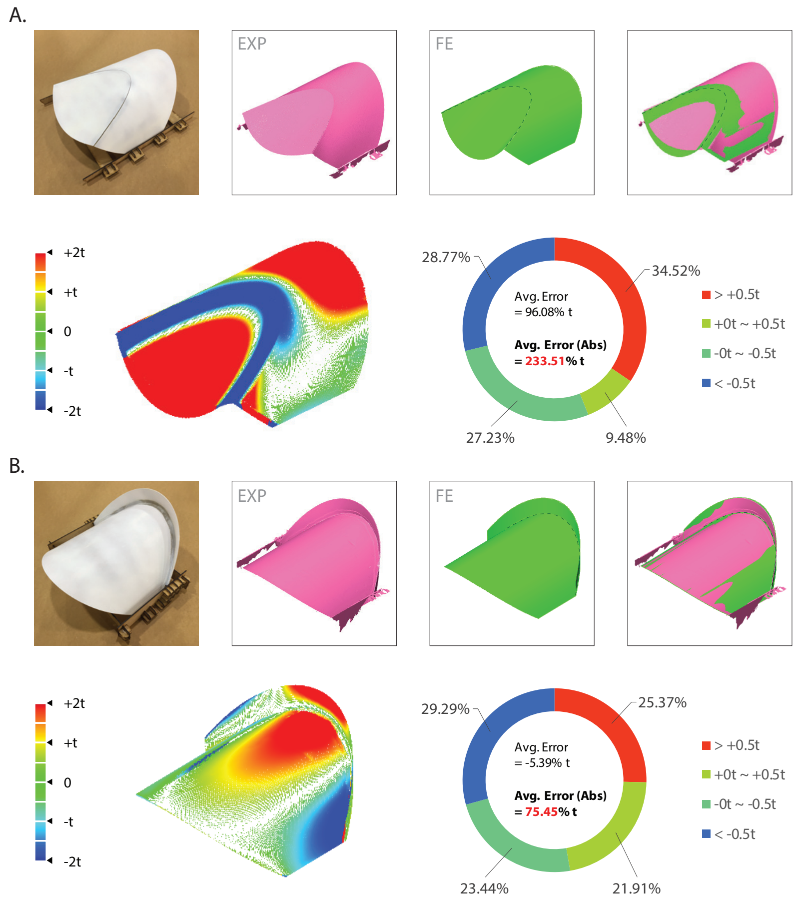

Fig. 3-28 Surface error measurement of Type 1 origami. (A) T1 CC Origami I. (B) T1 CC Origami II. Each sub-figure includes physical prototype, scanned mesh surface, simulated surface, best-fit scanned surface, correspondence result illustration, and result data.

of surfaces which possess free edge regions that are not parallel to the elastica construction plane, non-localised free edge effect, and the need to use of a straight-crease base pattern that approximates the desired curved-crease form.

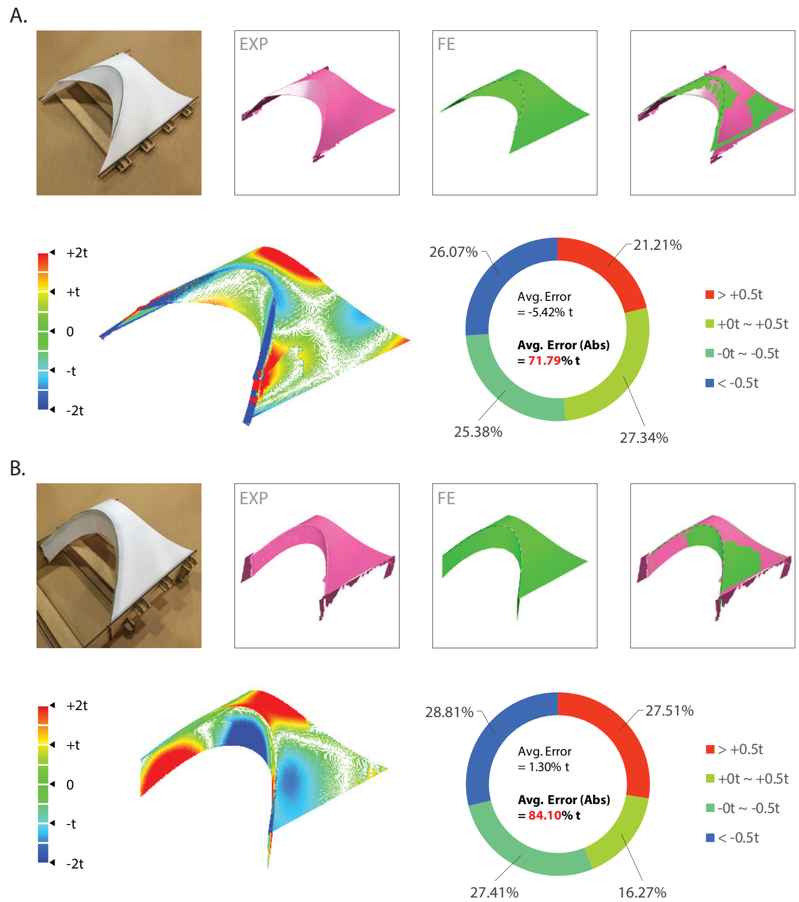

Fig. 3-29 Surface error measurement of Type 2 origami. (A) T2 CC Origami I. (B) T2 CC Origami II. Each sub-figure includes physical prototype, scanned mesh surface, simulated surface, best-fit scanned surface, correspondence result illustration, and result data.

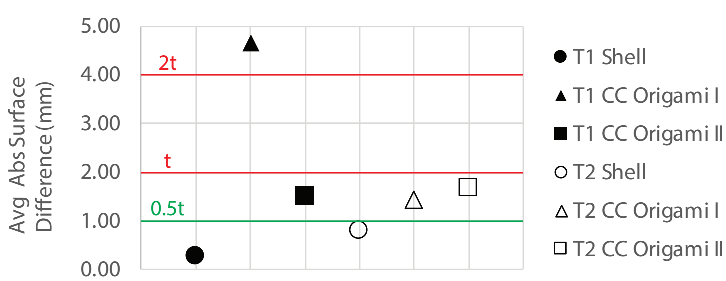

Fig. 3-30 Surface error measurement result summary of Type 1 and Type 2 geometries.

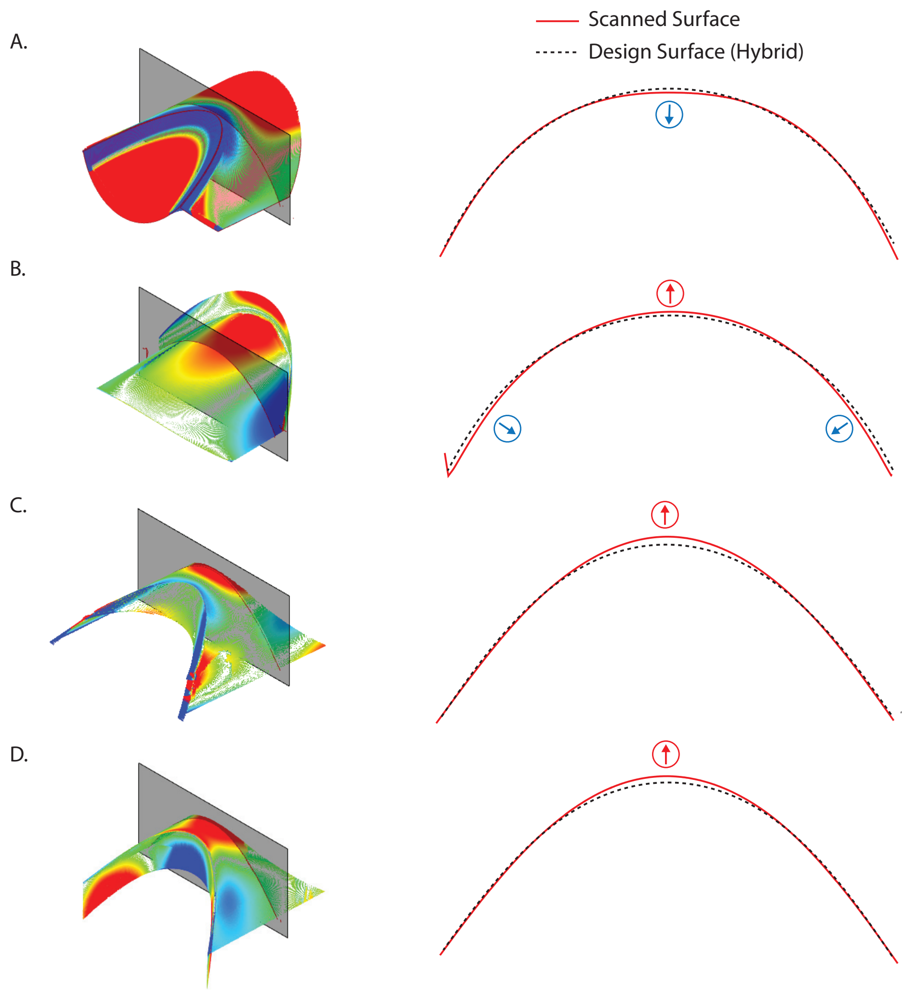

Fig. 3-31 Cross section analysis of (A) T1 CC Origami I, (B) T1 CC Origami II, (C) T2 CC Origami I, and (D) T2 CC Origami II.

Chapter 4 Curved-crease Origami Folding Mechanics

This chapter explores the folding mechanics of curved-crease origami by considering first the minimum elastic bending behaviours of a curved surface, and subsequently considering the interactions between this surface and introduced origami developability constraints. An analytical solution is presented by translating the local cross section deployment mechanics to a global frame of reference set according to the design parameters of the curved-crease origami unit geometry. A valid local-global translation and force-displacement response is found when the cross section deformations with and without developability constraints are suitably close to each other. This feature enabled a range of predictable non-linear force-displacement responses to be realised through the control of pattern edge angle design, edge length design, and tessellated forms.

4.1 Folding Mechanics of Curved-crease Origami

4.1.1 Elastic Bending Strain Energy of a Beam

It is here hypothesised that a lower bound energy prediction for a curved-crease origami, U_{BEND}, can be obtained if the total energy released is assumed to be the same as a non-folded curved surface constructed from an equivalent sheet. Equivalency is defined as a sheet possessing the same non-zero principal curvature, flexural rigidity, and area. The 'cross section' of the non-folded curved surface utilised in this study is adopted as the simplified representation of the surface and considered as an unconstrained 2D beam for analysis. Folding motion of the sheet can be obtained as the minimum bending energy deformations of the 2D beam representation with an arc length, L, and rectangular cross section, $w \times t$, deformed with a free boundary condition, as shown in Fig. 4-1A.

The elastic bending strain energy stored in the deformed beam representation is calculated based on the change in curvatures between the initial and deformed state. The curvature of the initial κ and deformed κ' beam sections are expressed in terms of radii of curvature ρ and ρ', respectively, and defined as the rate of change of the tangent angle $\frac{d\theta}{ds}$ and $\frac{d\theta'}{ds}$, respectively:

$$\kappa = \frac{1}{\rho} = \frac{d\theta}{ds} \tag{4-1}$$

$$\kappa' = \frac{1}{\rho'} = \frac{d\theta'}{ds} \tag{4-2}$$

where s is the position of a given section of the beam along the length, which is the same for initial and deformed states. The strain ε is determined as:

$$\varepsilon = -z\frac{d\theta - d\theta'}{ds - zd\theta} \tag{4-3}$$

where z is the position of the fibre of the beam section in thickness, t, that is $-t/2 \le z \le t/2$. For a linear elastic material, the stress, σ, has a linear relationship with the Young's modulus, E:

$$\sigma = E \times \varepsilon = E\Big(-z\frac{d\theta - d\theta'}{ds - zd\theta}\Big) \tag{4-4}$$

The elastic bending energy stored in the overall beam body, U_{BEND}, is then derived as [124, 125]:

$$\begin{aligned} U_{BEND} &= \int_V \frac{1}{2}\sigma\varepsilon dV \\ &= \frac{E}{2}\int_S \int_A z^2\Big(\frac{d\theta - d\theta'}{ds - zd\theta}\Big)^2 dAds \\ &= \frac{E}{2}\int_S \int_A z^2\Big(\frac{d\theta - d\theta'}{ds}\Big)^2\Big(\frac{1}{1 - z\frac{d\theta}{ds}}\Big)^2 dAds \\ &= \frac{E}{2}\int_S \int_A z^2\Big(\frac{1}{\rho} - \frac{1}{\rho'}\Big)^2\Big(\frac{1}{1 - z\frac{1}{\rho}}\Big)^2 dAds \end{aligned} \tag{4-5}$$

Solving the internal term $\int_A z^2(\frac{1}{1-z\frac{1}{\rho}})^2 dA$ gives,

$$\begin{aligned} \int_A z^2(\frac{1}{1 - z\frac{1}{\rho}})^2 dzdw &= w\int_{-\frac{t}{2}}^{\frac{t}{2}} z^2(\frac{1}{1 - z\frac{1}{\rho}})^2 dz \\ &= w\rho^3\Big(\frac{t}{\rho} + \frac{4t\rho}{(2\rho - t)(2\rho + t)} + 2ln\Big(\frac{2\rho - t}{2\rho + t}\Big)\Big) \end{aligned} \tag{4-6}$$

where w is the total width of the beam equivalent to the width of the curved surface, as shown in Fig. 4-1B. Substituting Equation 4-6 back into Equation 4-5 then gives the explicit form:

$$U_{BEND} = \frac{wE}{2}\int_S \Big(\frac{1}{\rho} - \frac{1}{\rho'}\Big)^2\rho^3\Big(\frac{t}{\rho} + \frac{4t\rho}{(2\rho - h)(2\rho + t)} + 2ln\Big(\frac{2\rho - t}{2\rho + t}\Big)\Big)ds \tag{4-7}$$

Calculation of U_{BEND} at sequential folded states is demonstrated using a beam deformed with an arc of uniform radius of 35.3mm at the initial state giving a curve design parameter b/L=0.75. This is the assumed cross section of a $w \times L$ = 180mm × 90mm sheet, as shown in Fig. 4-1A-B. The material properties of the beam representation are assumed as a t = 0.5mm isotropic PET sheet with E = 2299MPa. For this particular instance, deformed shapes were obtained using a numerical finite element method described in Section 3.3.2 with the 2D beam subdivided into 40 elements. The nodal displacement data were used to generate a smoothed deformed beam profile using a 3rd order polynomial interpolation, for each intermediate configuration. Curvature values were then evaluated with 1000 sampling points on the beam along its arc length. Combining multiple bending deformations with material properties in Equation 4-7 then gives the energy-displacement history path shown in Fig. 4-1C, where the displacement is measured as the changed in vertical distance between beam's mid and end position during intermediate states, denoted as $h - h'$.

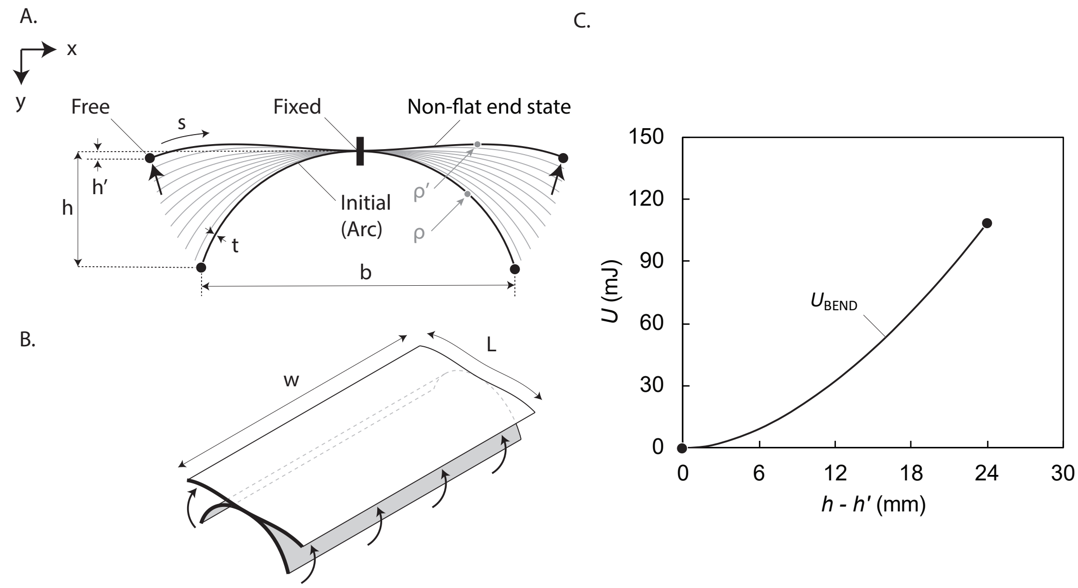

Fig. 4-1 Bending behaviour of a simple curved surface with an arc of uniform radius cross section profile. (A) Bending deformations using a 2D beam representation. (B) Illustration of arc surface bending. (C) Energy-displacement history path.

4.1.2 Comparison of Lower and Upper Bound Energy Behaviours

To investigate the interaction between a surface's minimum bending behaviour and developability-constrained behaviour, curved-crease origami geometries were created by imparting crease lines on a simple curved developable surface, with the utilisation of multiple intersecting truncation planes as developed in Chapter 3. The $w \times L$ sheet is reconfigured to a curved-crease origami by inverting and assembling the split panels about the truncation planes, where the inclination angle of the truncation planes is identified as η_B as shown in Fig. 4-2A. The edge angle, $\eta_A = \pi - 2\eta_B$, is useful in defining a particular volumetric configuration. If the constructed curved-crease origami is deformed, the developability of its 'local' cross sections are enforced by the developability constraint highlighted in Fig. 4-2B, which can potentially lead to a higher energy behaviour than the non-folded surface.

To explore the simplest case of developability condition, the curved fold developability constraint is set to have a zero rotational stiffness in this study. An upper bound energy behaviour of a curved-crease origami U_{PRBM} is defined when the foldability is fully enforced by the assumed rigid-ruling folding motion, as shown in Fig. 4-3A-B, which enables the utilisation of PRBM formulation (Equation 2-7) discussed in Section 2.2.3.

The U_{PRBM} calculation is demonstrated using a curved-crease origami constructed from the arc surface utilised in the previous section with $\eta_A = 90^o$, termed 'arc surface origami' and shown in Fig. 4-3A-B. The folding behaviour is simulated with surfaces approximated with $S = 100$ rigid divisions at the initial state following a convergence study described in Section 4.1.5. Longitudinal discrete rulings of surfaces are assigned with a linear spring

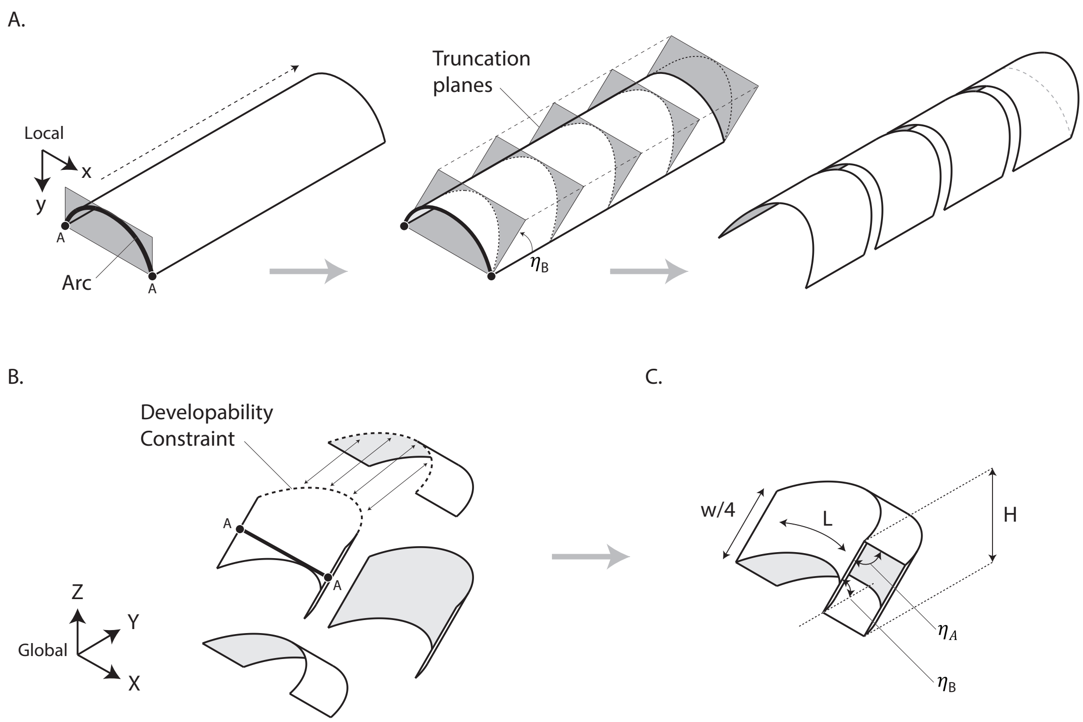

Fig. 4-2 Geometric construction of an initial curved-crease origami. (A) Simple curved developable surface split by multiple truncation planes. (B) Assembling the split components. (C) Constructed initial curved-crease origami.

stiffness equivalent to the material bending stiffness $k_s = EI/l_s$, where second moment of area $I = wt^3/12$, and spring effective length $l_s = L/S$. Local cross section displacement $h - h'$ was measured based on developability-constrained deformations, as shown in Fig. 4-3A.

Comparing energy behaviours of arc surface origami in Fig. 4-3C, it can be clearly seen that $U_{PRBM} > U_{BEND}$, with strict enforcement of the developability condition causing a higher energy behaviours as hypothesised. The energy paths are different because their corresponding deformation were approaching different end states; a 'non-flat' sheet-bending deformation is seen for U_{BEND} and a 'flat' developability-constrained deformation is seen for U_{PRBM}, as shown in Fig. 4-1A and 4-3A, respectively.

4.1.3 Elastica Surface Curved-crease Origami

A special class of 'elastica surface origami' exist, which adopts elastica curves as the generating curvatures for curved-crease pattern construction, as described in Chapter 3. Elastica curves are the elastically-deformed shapes of a straight slender beam, a simple elastica surface can be bent to a fully flat configuration following minimum bending energy deformation, as shown in Fig. 4-4A. Therefore, the surface bending behaviour of elastica surface origami during intermediate deformed states is hypothesised to be similar to the

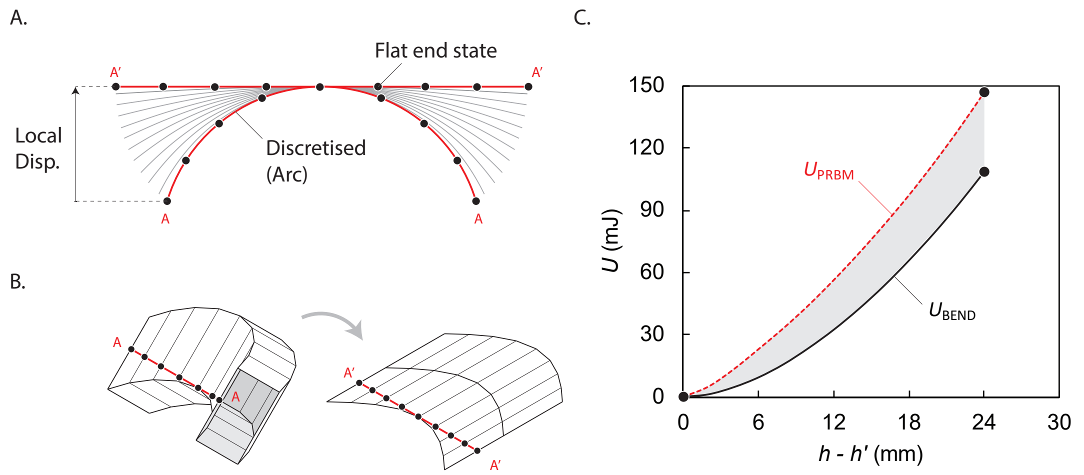

Fig. 4-3 Upper bound energy behaviour of arc surface origami. (A) Developability-constrained deformations of a 2D arc representation. (B) Initial and end folded state determined by rigid-ruling folding motion. (C) Upper and lower energy-displacement path comparison.

developability-determined rigid approximation, with both approaching to a flat configuration.

A 2D elastica curve is used for calculating the lower bound energy behaviour U_{BEND} of a simple elastica surface constructed from a $w \times L$ = 180mm × 90mm PET sheet. The elastica curve is designed to have a curve design parameter b/L=0.75, which is the same as the arc beam utilised in Section 4.1.1, but with a non-uniform curvature along its arc length. Analytical solutions are available for obtaining the exact shape of an elastica curve bent to sequential intermediate states [117, 118]. The U_{BEND} energy path is then obtained by incorporating exact beam bending deformations with the PET material properties, as shown in Fig. 4-4B.

The elastica surface origami geometry utilised in this section is reconfigured from the simple elastica surface with η_A= 90^o. The constructed surface is then discretised to give a rigid-foldable piecewise assembly of straight-crease origami for obtaining upper bound energy behaviour U_{PRBM}, as shown in Fig. 4-4B.

Comparing lower and upper bound energy behaviours of elastica surface origami, it can be clearly seen that $U_{PRBM} \approx U_{BEND}$, with a common end sheet-bending and developability-constrained deformation causing a highly similar lower and upper bound energy behaviour as hypothesised. The similarity also indicates that the developability constraint has a small/neglectable influence to surface minimum bending behaviour during the folding motion. Looking at a comparison of energy behaviours across elastica and arc surface origami in Fig. 4-4C and Tab. 4-1, $\Delta U = U_{PRBM} - U_{BEND}$ for the elastica surface origami is seen to be extremely small in compared with arc surface origami. As the only difference between arc and elastica surface origami is the curvature design at the initial state, it is confirmed that the curvature design is a key component to accurately determining energy behaviours of curved-crease origami.

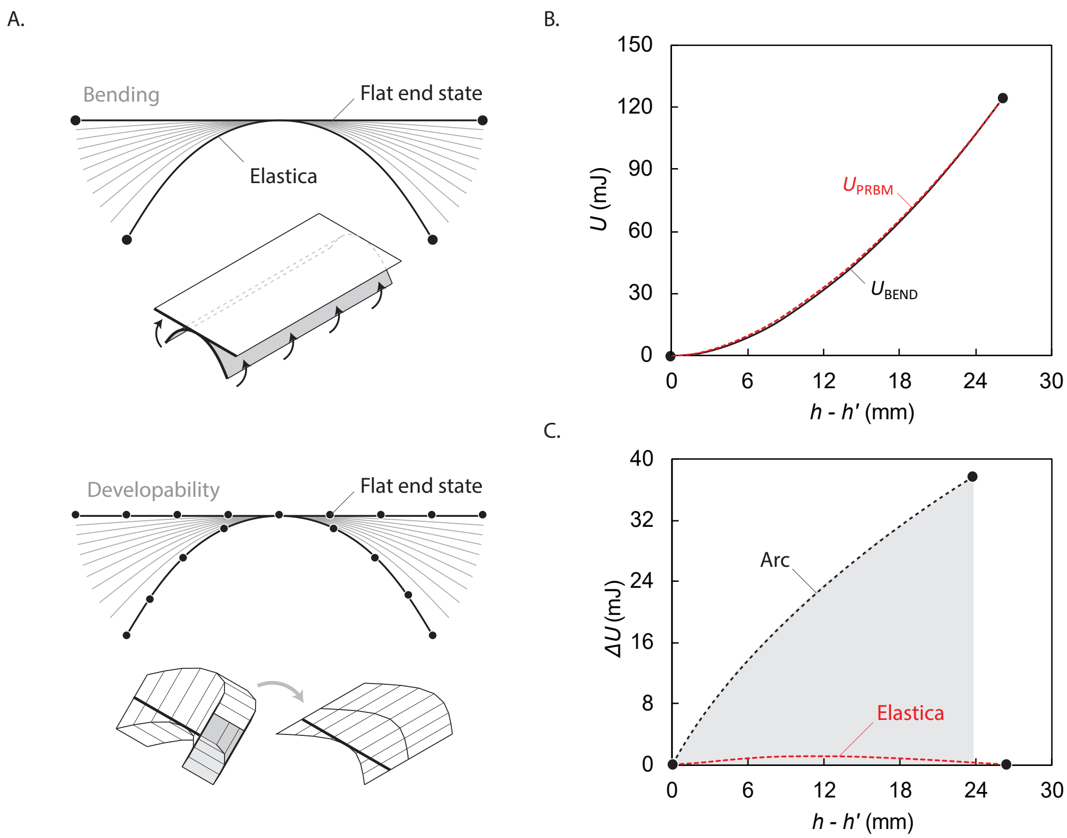

Fig. 4-4 Energy behaviours of elastica surface origami. (A) 2D representation of bending and developability deformations. (B) Lower (U_{BEND}) and upper (U_{PRBM}) energy-displacement path comparison. (C) ΔU comparison of elastica and arc surface origami.

Tab. 4-1 Compariosn of energy behaviours of elastica and arc surface origami

$(h - h')$: 0 to 24	mm	Elastica	Arc
Max. U_{BEND}	(mJ)	107.44	108.63
Max. U_{PRBM}	(mJ)	107.69	146.58
Max. ΔU	(mJ)	1.21	37.95

4.1.4 Experimental Validation of Energy Behaviours

To validate the accuracy of energy behaviours during curved-crease folding, prototypes were manufactured and tested. Geometries were selected to be the elastica and arc surface origami with parameters as described above. The material selected for this investigation was the 0.5mm thick PET sheet. Curved panels were then jointed with a 0.1mm thick isotropic vinyl hinge, which has a relatively small rotational stiffness but with sufficient connectivity to resist the separation of parts during folding. Prototypes were subjected to a quasi-static compression test by using a Type 5982 Instron Universal Testing Machine.

The specimens were compressed at a rate of 60 mm/min and until 75-80% of their original hight. Finite element (FE) simulations were also created to ensure that the experimental data is not distorted by manufacturing and/or measurement defects.

FE simulations were created in the commercial software Abaqus. An implicit *non-linear static analysis* method was used, which accounts for geometric nonlinearity due to large displacements and rotations, where material and boundary nonlinearity were neglected. Similar to the experimental method, displacement-control was applied on two external rigid plates to laterally compress the deformable curved-crease pattern in the software, and material properties were set to be the same as the PET sheet described above. During deformation, NLGEOM was turned on, which accounts for stiffening effects with stiffness matrix being updated after each step. Surfaces were meshed with quadrangle S4 shell elements, with an approximate global size set at a fine size 1mm following a convergence study. Crease lines were modelled to be a 0.5mm wide and 0.05 mm thick reduced-thickness regions, similar to the manner described in Gattas et al. [56], as shown in Fig. 4-5. Penetration was not permitted between panels, but it was permitted in the hinge region to prevent thickness interaction. By using this simulation method, the approximate bending behaviour of the curved-crease can be captured. It is approximate, because the crease modelling method is different to the actual crease construction. Therefore, strain energy result data is collected from panels only, where the crease 'region' energy contribution is neglected.

For elastica surface origami, accurate prediction is observed in Fig. 4-6A, attributed to a minimally-distorted panel bending behaviour. For arc surface origami, it can be seen that the constructed model has an energy behaviour between U_{BEND} and U_{PRBM} in Fig. 4-6B. This is believed to be due to the developability condition not being exactly enforced in the physical prototype with the result being a bending behaviour between surface bending behaviour and origami developability constraints. However, the lower and upper bound solution are still useful references for determining the energy bounds of a curved-crease origami.

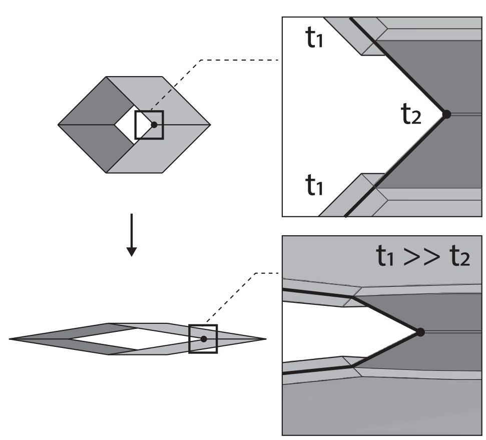

Fig. 4-5 FE simulation method for the hinge region of curved-crease origami.

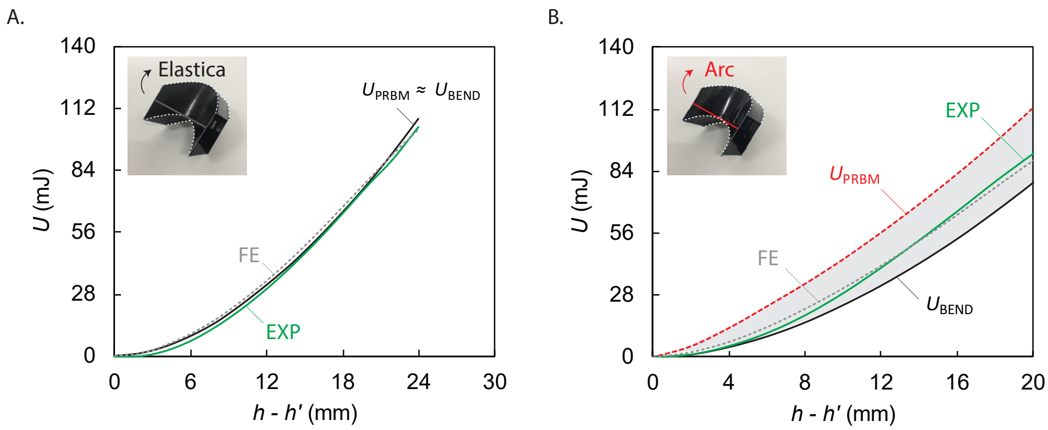

Fig. 4-6 Energy behaviour of a physical curved-crease origami during folding motion. (A) Elastica surface origami. (B) Arc surface origami.

4.1.4.1 Mechanical Properties of PET

Material tensile test of isotropic PET was conducted for obtaining its mechanical properties. From the result stress-strain curve shown in Fig. 4-7, it can be seen that the selected material has a linear-like elastic behaviour, where the fracture point is seen at approximately 50MPa. For FE simulations, the material is considered to be linear elastic; the Young's modulus, E = 2299MPa, was obtained in the near-linear region, where the stress value is less than approximately 11MPa.

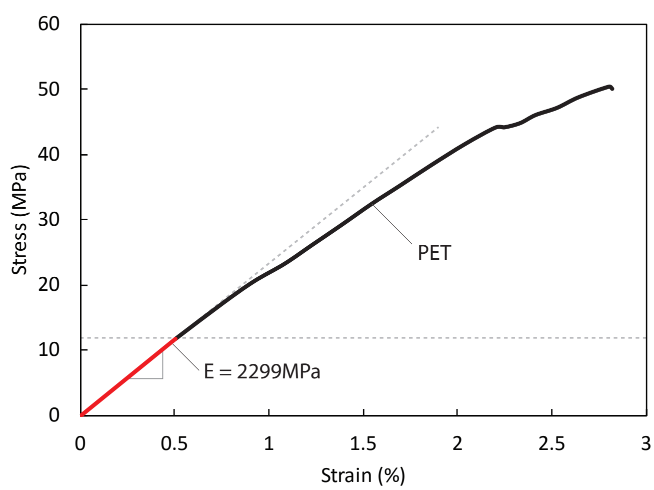

Fig. 4-7 Material tensile test result of PET.

4.1.5 Further Details of PRBM Calculation

To ensure that the PRBM approach used in this study is reliable, an S convergence study was conducted, as S (number of rigid divisions) determines the resolution of rigid-foldable curved-crease approximations. To this end, there are two ways to improve the folding simulation generated from the rigid assembly:

- Smoothing the rigid-foldable curved-crease surface at the initial state by increasing the number of rigid divisions, or
- Rebuilding the curved-crease developable surface for each intermediate folded state by creating curved boundary edges from discrete vertices using a 3rd order polynomial interpolation, as shown in Fig. 4-8A.

The later can result in an interpolated-pseudo-rigid-body-model (IPRBM) shown in Fig. 4-8B. This then allows the strain energy history to be obtained based on the curvature measurement of the cross section using Equation 4-7. A reliable S value is said to be obtained if PRBM and IPRBM give the same strain energy results.

To assess the difference between PRBM and IPRBM, the tested geometry was selected to be the curved-crease component of the elastica surface origami used in Section 4.1.3. Strain energy values were captured at 25%, 50%, 75%, and 99% deformed state with S ranging from 2 to 500. The comparison result between methods is shown in Fig. 4-8C. A good correspondence is seen when a large S value is used, that is $S > 50$. The good correspondence also represents that both PRBM and IPRBM are sharing a similar folding motion, attributed to a similar initial state origami surface, as shown in Fig. 4-8D. Therefore, the $S = 100$ used in this study is considered to be a reliable value in determining U_{PRBM}, as it is capable of generating fine approximations of curved-crease origami surfaces.

4.1.6 Comparison of Cross Section Profiles

A conclusion drawn from Fig. 4-4C is that if the sheet-bending and developability-constrained deformations exhibit 'common' or 'different' curvatures at their end deformed state, then 'converging' and 'diverging' energy behaviours will occur, respectively. This can be demonstrated more clearly by comparing the shape of the cross section representations and the curvature variances between curves, which can be achieved by comparing their tangent angles difference $\Delta\theta = \theta_{BEND} - \theta_{PRBM}$ along the arc length as shown in Fig. 4-9A.

The comparison result for elastica and arc surface origami is shown in Fig. 4-9B and Fig. 4-9C, respectively. For elastica surface origami, the tangent angle measurement demonstrates a zero difference at the initial and end state, hence enabling intermediate deformations to have a high similarity, as the tangent difference on all points were converging to zero. Arc surface origami on the other hand has an increasing tangent angle variance on all measured points, as its sheet-bending and developability-constrained deformations are diverging toward different end states.

4.1.6.1 Detail Calculation

Detail calculation of developability-constrained tangent angle during the folding motion, θ_{PRBM}, is summarised as follows. At the initial state, the tangle angle of the measured point on the cross section is denoted as Θ_1, as shown in Fig. 4-10A. It can be used to obtain an useful projected tangent angle parameter, Θ_P, by specifying h and η_A using Equation

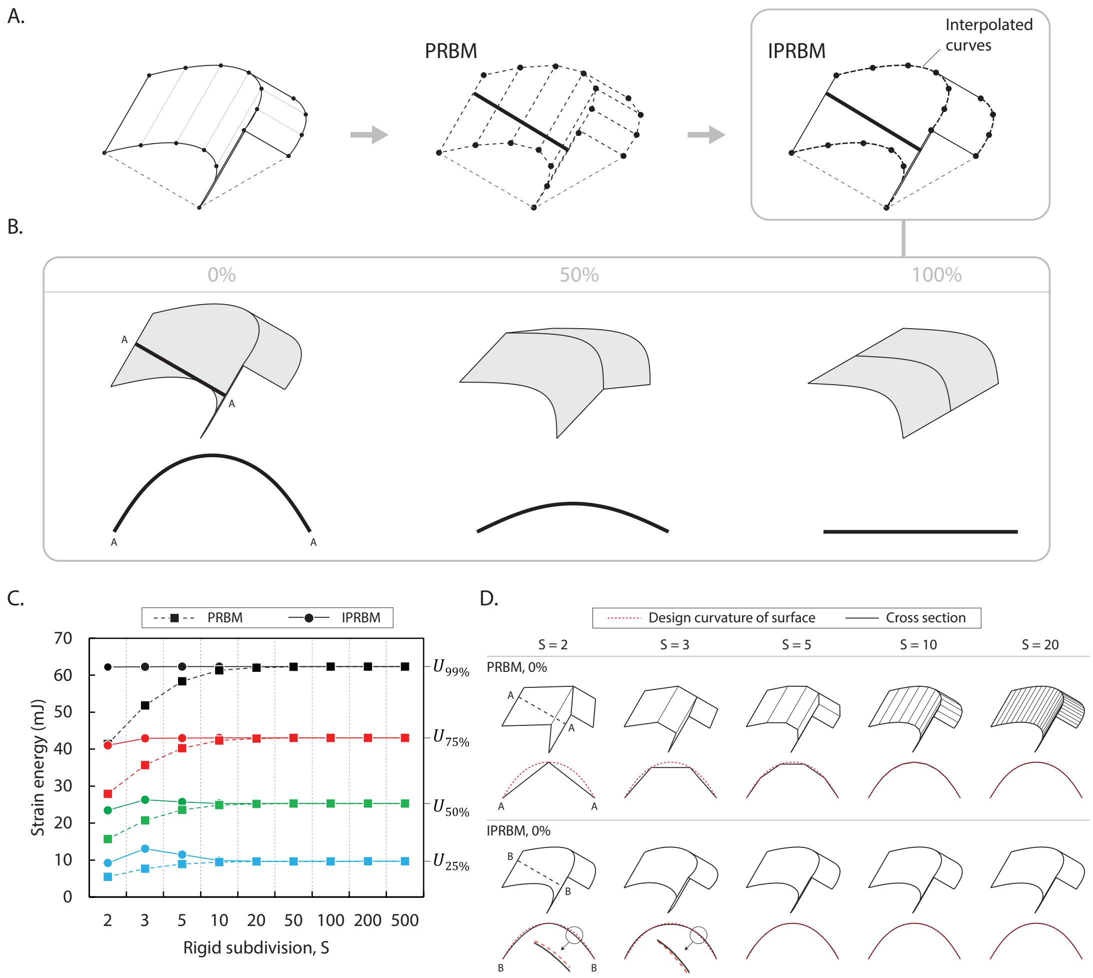

Fig. 4-8 PRBM and IPRBM. (A) Generation of PRBM and IPRBM. (B) Folding simulation of the IPRBM. (C) Strain energy result comparison. (D) Initial state cross section comparison with the exact form.

4-8-4-12:

$$\Theta_P = \sin^{-1}\left(\frac{\sqrt{h^2 + {w_k}^2}}{d_1}\right) \tag{4-8}$$

$$w_k = \frac{h}{\tan \eta_B} \tag{4-9}$$

$$\eta_B = \frac{\pi - \eta_A}{2} \tag{4-10}$$

$$d_1 = \sqrt{{e_1}^2 + {w_k}^2} \tag{4-11}$$

$$e_1 = \frac{h}{\sin \Theta_1} \tag{4-12}$$

where w_k is a length constant which describes the skewness of the boundary edge.

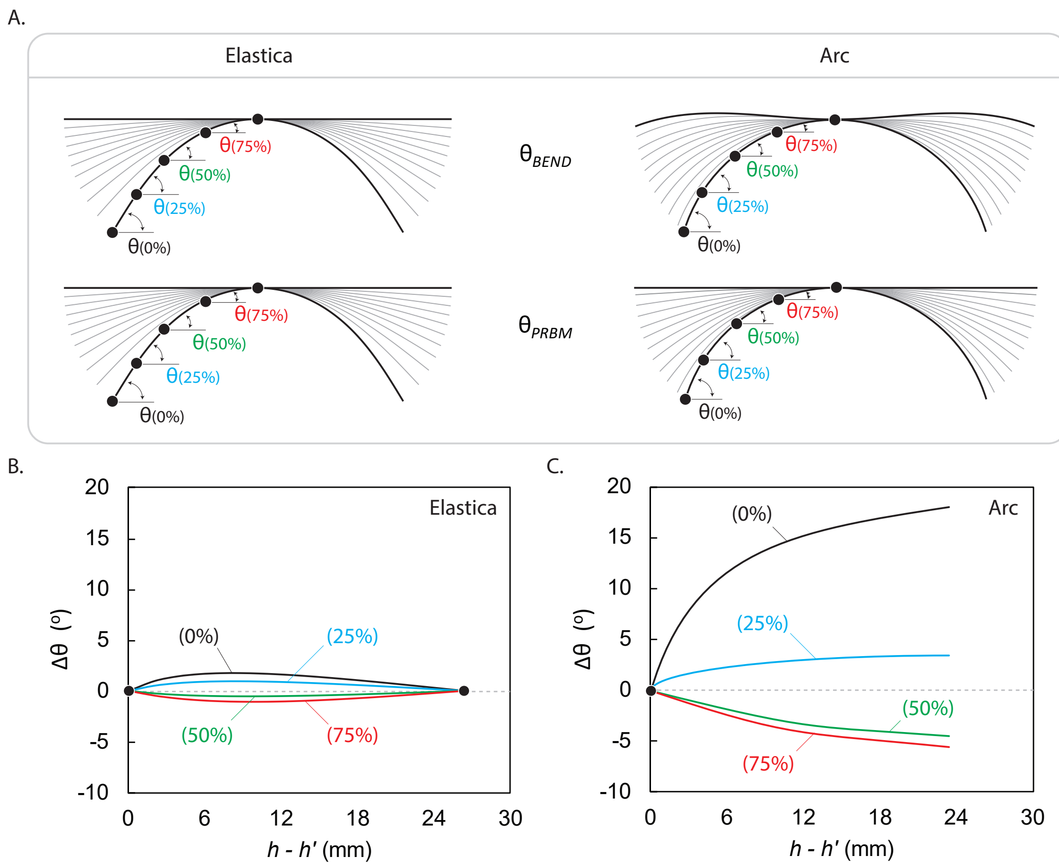

Fig. 4-9 Tangent angle measurement. (A) 2D dending and developability deformation of elastica and arc. (B) $\Delta\theta$ for elastica surface origami. (C) $\Delta\theta$ for arc surface origami.

Substituting Θ_P and η_B into Equation 4-13-4-14 then gives the lateral angle parameter, ϕ:

$$\phi = \cos^{-1}\left(\frac{\cos\eta_B}{\cos\gamma}\right) \tag{4-13}$$

$$\gamma = 0.5\pi - \Theta_P \tag{4-14}$$

During folding, ϕ remain unchanged as shown in Fig. 4-10B, hence the projected tangle angle parameter at the intermediate folded state, Θ'_P, can be calculated as,

$$\Theta'_P = \sin^{-1}(\cos\gamma') \tag{4-15}$$

$$\gamma' = \cos^{-1}\left(\frac{\cos\phi}{\cos\eta'_B}\right) \tag{4-16}$$

$$\eta'_B = \tan^{-1}\left(\frac{h'}{w_k}\right) \tag{4-17}$$

Finally, the tangent angle of the measured point at the intermediate folded state, Θ_2, is calculated using Equation 4-18-4-20:

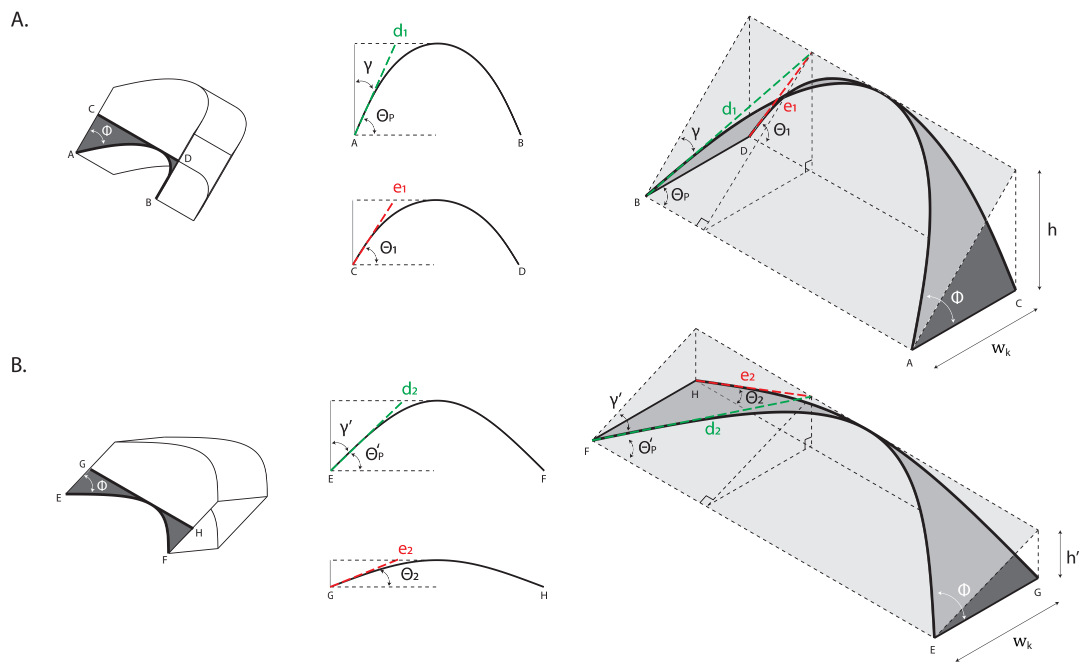

Fig. 4-10 Developability-constrained tangent angle calculation. Design parameter of the curved-crease origami at its (A) initial state and (B) intermediate folded state.

$$\Theta_2 = \sin\left(\frac{h'}{e_2}\right) \tag{4-18}$$

$$e_2 = \sqrt{{d_2}^2 - {w_k}^2} \tag{4-19}$$

$$d_2 = \frac{\sqrt{{w_k}^2 + h'^2}}{\sin \Theta'_P} \tag{4-20}$$

Therefore, the entire θ_{PRBM} response at a point can be obtained by specifying a single Θ_1 value and multiple Θ_2 values for intermediate folded states.

For bending-determined tangent angle during the folding motion, θ_{BEND}, an analytical solution is available for elastica beam deformations, but not for arc beam deformations. The entire θ_{BEND} response for unique elastica beam was obtained using Equation 2-14 with multiple elastica bending configurations being specified. The θ_{BEND} response for the arc beam used in this study was directly measured on numerical deformations shown in Fig. 4-1A using Rhino-Grasshopper measurement tools.

4.2 Parametric Investigation of Force-displacement Responses

4.2.1 Translation of Local Deployment Mechanics

For compliant mechanisms, the mechanism response along the actuation direction is typically more useful than an energy response as measured in a cross section deformation direction. The 'global' response as measured in the actuation direction can be understood as the product of 'local' cross section bending deployment with global origami geometry transformation. If the local bending mechanics of curved-crease panels are minimally distorted, they can be 'translated' to an analytical global force-displacement response set according to the origami design parameters shown in Fig. 4-11A. A *curved-crease bending translation* (CCBT) method is here proposed to convert a local energy-displacement response to a global energy-displacement response, and subsequently to a global force-displacement response, as shown in Fig. 4-11B.

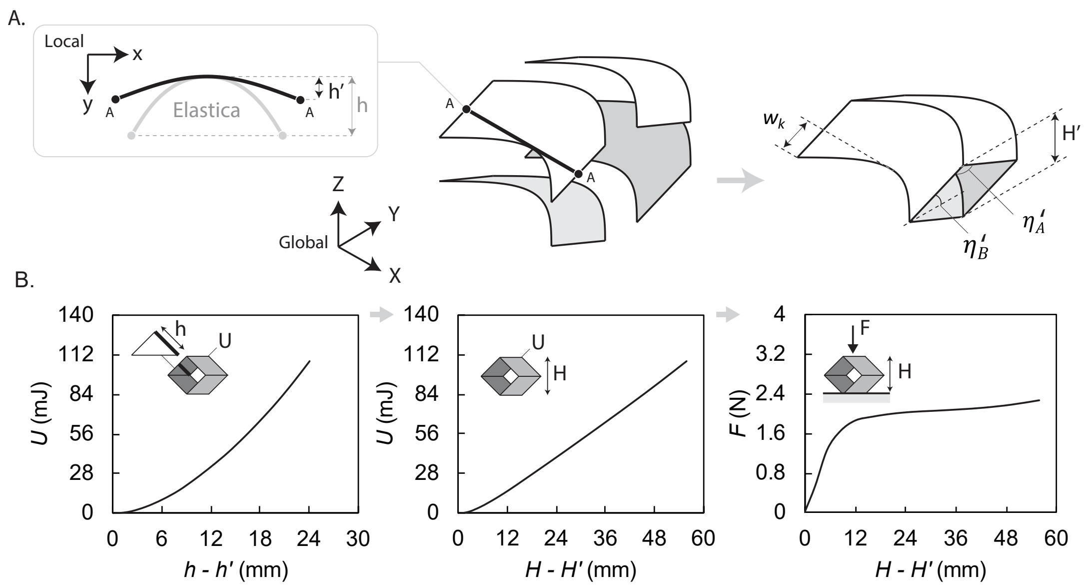

Fig. 4-11 Local-global translation of curved-crease origami mechanics. (A) Intermediate state simulation using a valid 2D beam deformation as the non-zero principal curvature. (B) The mechanics response translation stated from left to right: local energy-displacement, global energy-displacement, and global force-displacement.

The CCBT method first translates the local displacement measurement $(h - h')$ to a global displacement measurement $(H - H')$. At the initial state, the global height of the curved-crease origami H is determined based on η_B, as shown Fig. 4-2C:

$$H = \frac{w}{2} \sin \eta_B \tag{4-21}$$

During deformation, the global height H' is calculated based on the assembly of deformed panels determined by η'_B, as shown in Fig. 4-11A:

$$H' = \frac{w}{2} \sin \eta'_B \tag{4-22}$$

The output force F along global-Z direction generated from the summation of internal strain energy U is then calculated as:

$$F = \frac{dU}{dZ} \tag{4-23}$$

The elastica surface origami was constructed for validating the accuracy of the analytical global force-displacement prediction. It can be seen that the analytical (ANA) prediction and experimental (EXP) result have demonstrated good agreement in Fig. 4-12A. However, variances are seen beyond Point (c), when the local cross section is approaching to a near-flat configuration ($b/L \approx 1$). The error occurred mainly due to the 'free edge effect' described in Section 3.3.2, where a stress concentration is seen around the crease-line region, attributed to the non-uniform stress transfer on a non-rectangular surface, as highlighted in Fig. 4-12B. Initial investigation of the free edge effect of curved shells is shown below, but it will not be closely studied in this chapter, because the prediction error occurred only when the curved-crease origami was deformed to a near-flat configuration; intermediate states demonstrated a good correspondence.

Other predictable global force-displacement responses can potentially be achieved by adjusting curved-crease origami design parameters. A parametric study was conducted to investigate this using a range of elastica surface origami.

4.2.1.1 Free Edge Effect of Curved Shells

To explore the free edge effect in curved-crease folding behaviours, two curved shells were designed, simulated, and tested with physical models. They were simple and skewed curved developable surface, corresponding to Fig. 4-13A and B, respectively. Both models were designed from a 90mm × 90mm PET sheet, with elastica surface design parameter to be $b/L = 0.75$, and $\eta_B = 45^o$ for the skewed surface. Analytical force-displacement predictions for both models were translated from U_{BEND} using the proposed CCBT method and exact elastica beam bending deformations shown in Fig. 4-4A. It can be seen that analytical predictions and EXP results have demonstrated good correspondence for both models. However, minor variances are seen from the initial state with FE confirms that errors were not simply attributed to manufacturing or measurement defects. For simple curved developable surface, the source of error is believed to be due to the coupling effect between in-plane loading and out-of-plane deformation, result in warped free edges as highlighted in Fig. 4-13A. For skewed curved developable surface, the error is attributed to the combination of warped free edges and non-rectangular sheet bending, result in a non-uniform stress transfer contour shown in Fig. 4-13B. However, wrapped regions are relatively small compared to the overall shell area for both models, hence enabling actual bending behaviours to be captured using a simplified 2D beam bending representation. Furthermore, if the skewed shell is designed with a shorter edge length, the effect of non-rectangular sheet bending will be amplified, as shown in Fig. 4-12B. A more significant finding is that these free edge effects will not be eliminated in certain curved-crease origami forms, and a more complex behaviour will occur when the 'free edges' are subjected to geometric constraints.

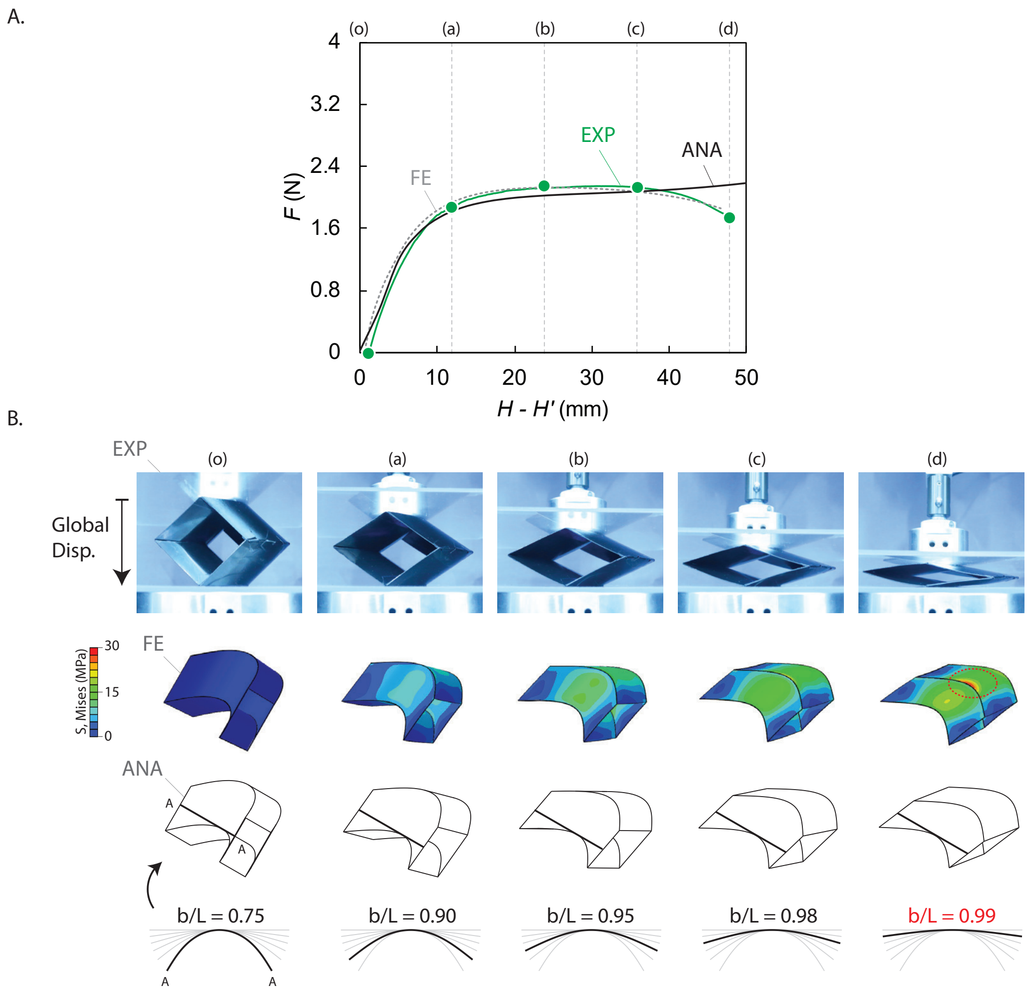

Fig. 4-12 Experimental analysis of local-global mechanics translation. (A) Global force-displacement responses comparison. (B) Intermediate folded configurations, from top to bottom: experimental, numerical, and analytical.

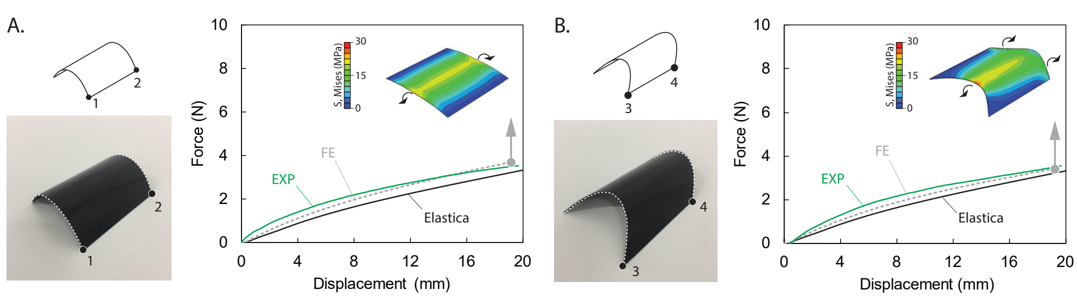

Fig. 4-13 Free edge effect of curved shells. (A) Simple curved developable surface. (B) Skewed curved developable surface.

4.2.2 Edge Angle Effect

With reference to Fig. 4-2, it can be seen that the shape of the crease line of a curved-crease origami is generated from the intersection between the curved surface and inclined truncation planes, which give the edge angle η_A after the component surfaces are assembled. An initial set of models were generated by altering the edge angle of an initial curved-crease origami with the local cross section and origami design parameters remaining unchanged, as shown in Fig. 4-14A. Two physical prototypes were tested, which were modified from the elastica surface origami utilised in the previous section ($\eta_A = 90^o$). They were $\eta_A = 120^o$ and 60^o, corresponding to results shown in Fig. 4-14B and C, respectively. Experimental results are seen to have a good agreement with analytical predictions for both prototypes. On the comparison of force-displacement paths in Fig. 4-14A, a more significant feature can be observed, that is the global force-displacement *response type* [126] can be achieved using different elastica surface origami constructed from the same elastica surface:

- Path (a): When η_A >90^o, a hardening response will occur, as validated in Fig. 4-14B.
- Path (b): When η_A =90^o, a plastic response will occur, as validated in Fig. 4-12A.
- Path (c): When η_A <90^o, a softening response will occur, as validated in Fig. 4-14C.

A stronger free edge effect and prediction error is seen when the component surfaces have skewered edges, but it only occurs when the local deformation is approaching to a near-flat configuration as discussed above.

4.2.3 Edge Length Effect

Recalling Equation 4-21, the global height H of the initial curved-crease origami can be controlled by varying the edge length design parameter w with a fixed η_B. A modified elastica surface origami was tested, with its edge length designed to be twice as long than the elastica surface origami utilised in Section 4.2.1, as shown in Fig. 4-15A. It can be seen that the experimental result again confirms the reliability of the analytical prediction, as shown in Fig. 4-15B and that an extended force-displacement response has been achieved by using a longer edge length design. It is concluded that the edge length determines the displacement capacity of the force-displacement response, assuming the local cross section and origami design parameters remain unchanged.

4.2.4 Modular Tessellation

A unit curved-crease origami geometry can be tessellated to larger configurations for fulfilling specific design objective, where the deployment mechanics of the macro tessellated form is generated from repeated unit geometries. Four tessellated forms were tested including two in-plane tessellations (Tessellation X and Y), one out-of-plane tessellation (Tessellation Z), and one combined tessellation (Tessellation XYZ), as shown in Fig. 4-16A. Depending on the method of tessellation, different global force-displacement

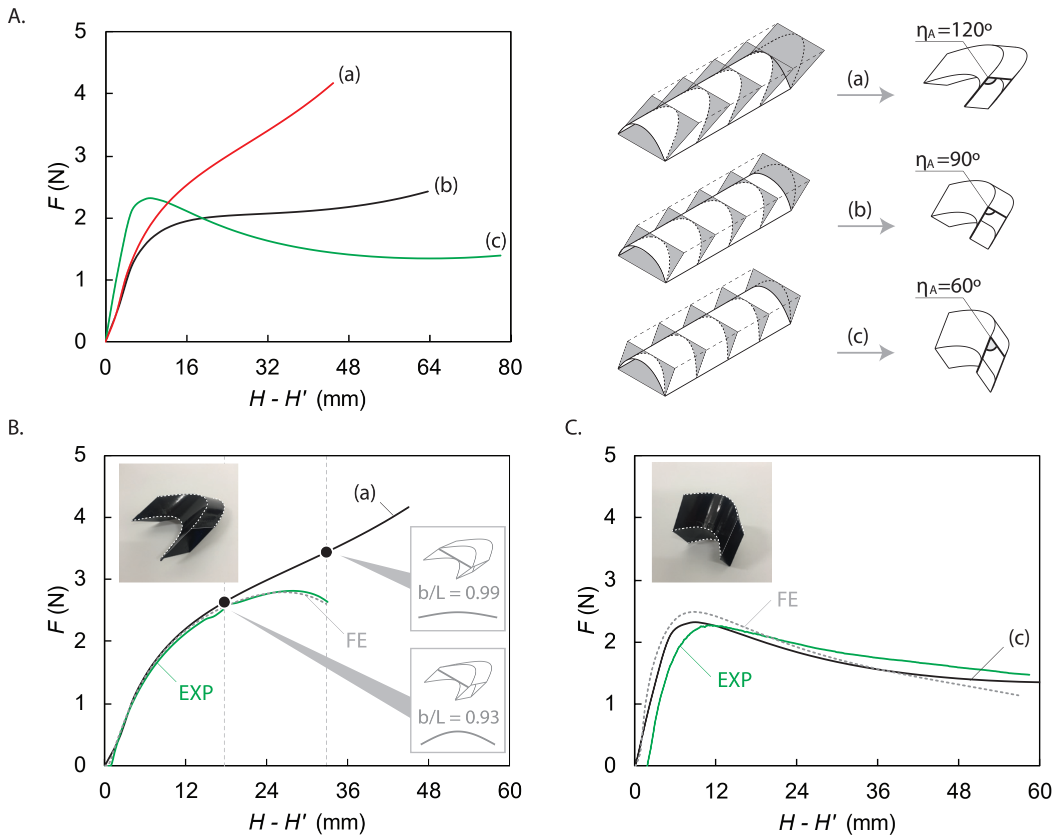

Fig. 4-14 Global force-displacement investigation of edge angle effect. (A) Analytical predictions. Experimental result of edge angle η_A = (B) 120^o, and (C) 60^o.

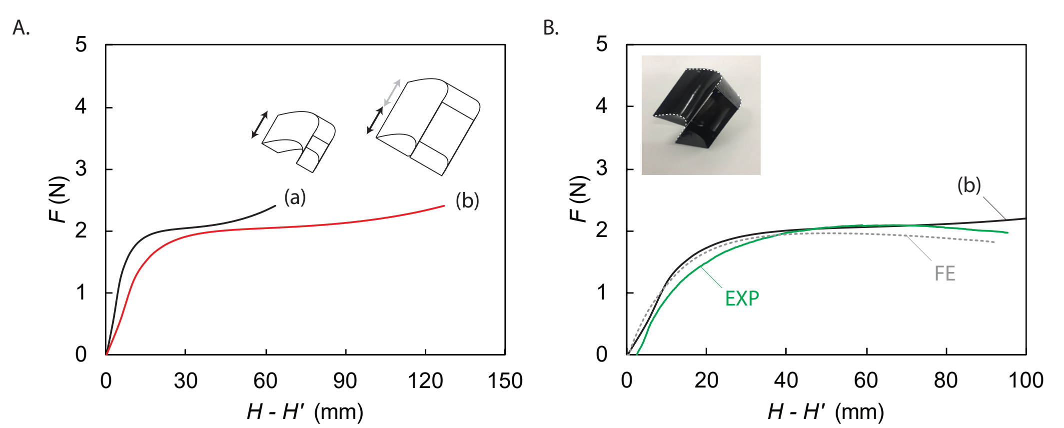

Fig. 4-15 Global force-displacement investigation of edge length effect. (A) Analytical prediction. (B) Experimental result of an elastica surface origami with doubled edge length.

responses can be realised. If considering the base unit as a non-linear mechanical spring, in-plane tessellation will give a parallel spring behaviour, out-of-plane tessellation will give a series spring behaviour, and the combined tessellation will give a combined parallel and series spring behaviour, as validated in Fig. 4-16B-C, Fig. 4-16D, and Fig. 4-16E, respectively.

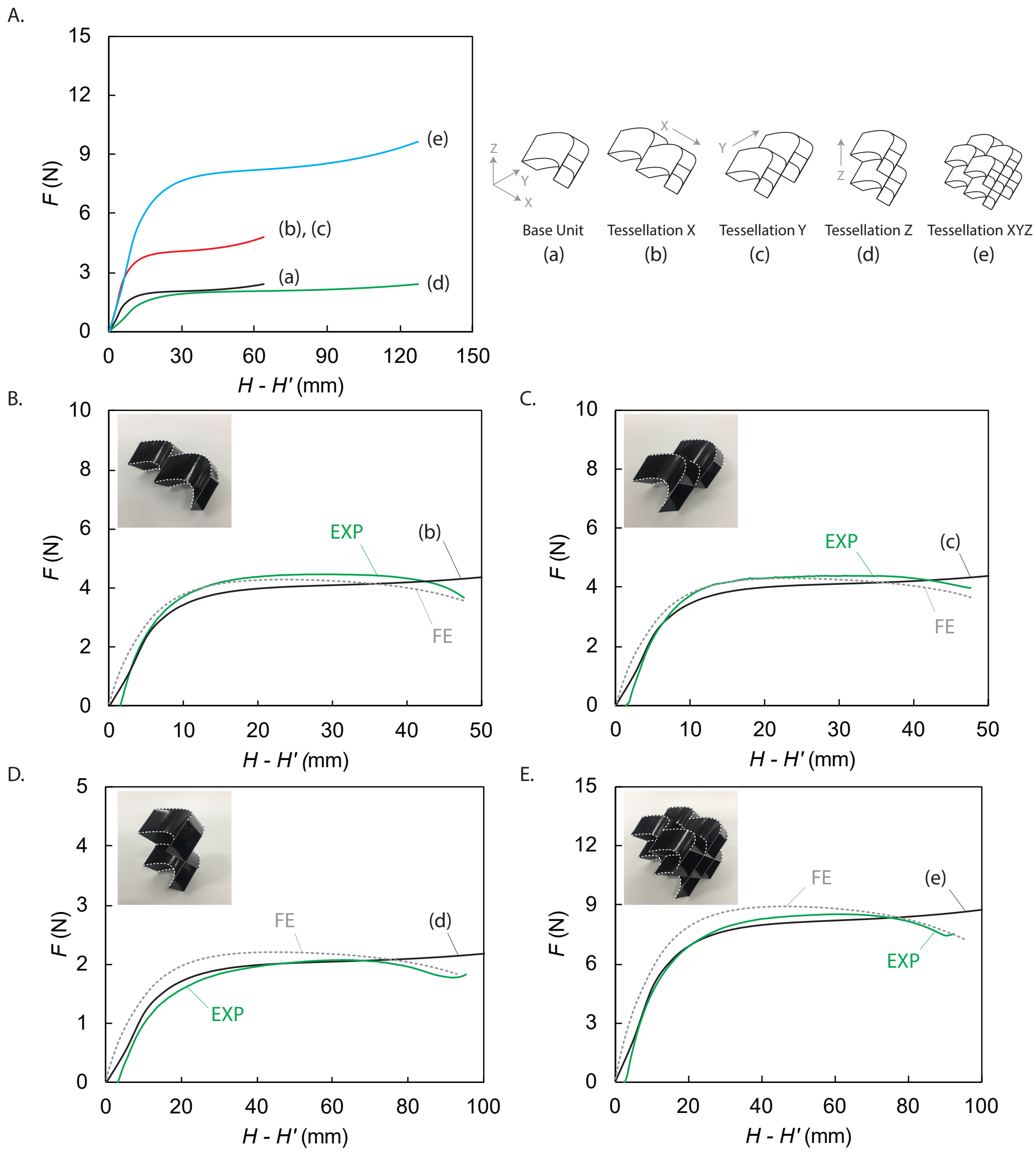

Fig. 4-16 Global force-displacement investigation of modular tessellation. (A) Analytical predictions. Experimental result of (B) Tessellation X, (C) Tessellation Y, (D) Tessellation Z, and (E) Tessellation XYZ.

4.3 Customizable Force-displacement Responses

A customizable global force-displacement response can be realised by using an elastica surface origami and the insight gained into the effect of available origami design parameters. This is demonstrated more clearly in Fig. 4-17 and by following the four design steps:

Step 1 selects a desired shape of the global force-displacement response. Diverse responses can be generated by modifying a default elastica curved-crease origami with different edge angles, η_A, as shown in Fig. 4-17A. The default origami utilised in this example is the same as the elastica surface origami designed in Section 4.1.3, which can be specified by nine design parameters, including $\eta_A = 90^o$, $w = 180$mm, $L = 90$mm, $b/L = 0.75$, $E = 2299$MPa, $t = 0.5$mm, $T_x = 1$, $T_y = 1$, and $T_z = 1$, where T_x, T_y, and T_z are the number of tessellations in X, Y, and Z, respectively. The modified form, (a), is selected to have a softening response with the origami edge angle designed to be $\eta_A = 45^o$.

Step 2 determines the maximum displacement, H, of the global force-displacement response. This can be done by controlling the edge length design parameter, w, and out-of-plane tessellation, T_z, of the origami, as shown in Fig. 4-17B. Specifying H and η_A allows the total width requirement of the sheet to be calculated using Equation 4-21-4-10. For this example, (a) is modified to (b) with $H = 60$mm by setting $w = 130$mm and $T_z = 1$.

Step 3 designs the energy response, U, of the unit origami geometry, that is the area under the force-displacement path. With reference to Equation 4-7, the energy response is determined by the origami cross section design, L and b/L, and material properties, E and t, as shown in Fig. 4-17C. A desired energy response can therefore be generated with a range of elastica curves and diverse elastic sheet materials. Available elastica curves are ranging from $b/L < 1$ to the contact limit state as discussed in Chapter 3-5. However, not all materials have the capacity to be elastically-bent with the selected curvature, suitable combinations must be bent within the elastic strain limit [127, 128]. As steeper curvatures are more difficult to be deformed with fixed material properties, using shallower curvature is one way to avoid plastic deformations. This is shown more clearly by reducing the cross section steepness of (b) to (c) with b/L decreased to 0.85.

Step 4 finalises the total energy response and the shape of macro tessellated form. This can be done by specifying T_x and T_y for obtaining in-plane tessellation forms, as shown in Fig. 4-17D. As the result, the unit origami geometry will proceed a repeating unit performance and amplifies the energy response with a parallel spring behaviour, for example, (c) is tessellated to (d) with $T_x = 2$ and $T_y = 2$.

4.4 Conclusion

This chapter has analytically investigated the folding mechanics of curved-crease origami by considering surface minimum elastic bending behaviours, and validated by a set of manufactured prototypes. The curvature design in curved-crease origami was found to be the key component to determining the interaction between surface bending behaviour and origami developability constraints. More significantly, the use of elastica curve for non-zero principal surface curvatures allows surface minimum elastic bending behaviours to be preserved under a developability-constrained condition. This enabled the energy re-

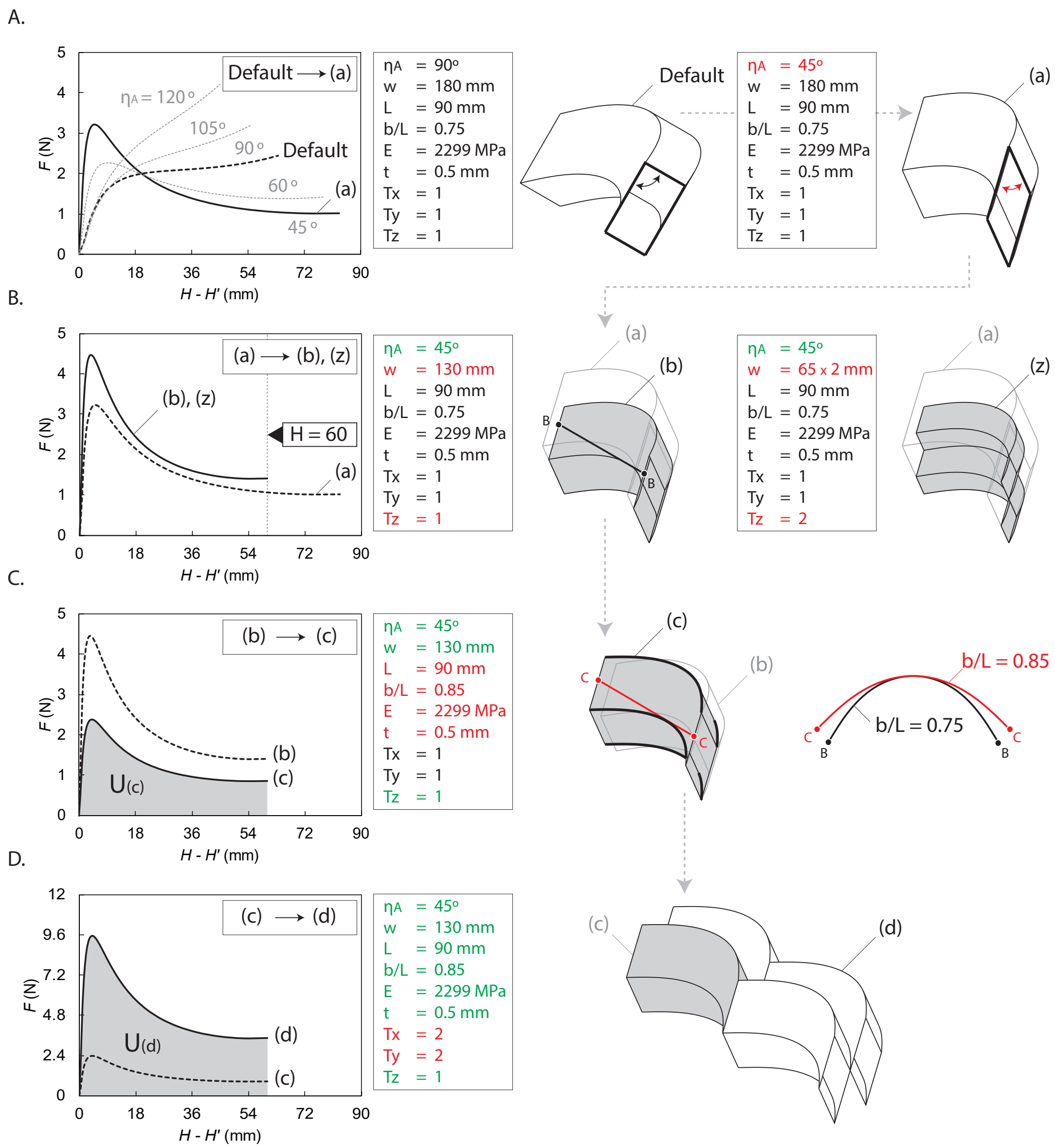

Fig. 4-17 Customizable force-displacement responses. (A) Step 1 selects a desired shape of the global force-displacement response. (B) Step 2 determines the maximum displacement, H, of the global force-displacement response. (C) Step 3 designs the energy response, U, of the unit origami geometry. (D) Step 4 finalises the total energy response and the shape of the macro tessellated form.

sponse of an elastica surface origami to be accurately predicted using both U_{PRBM} and U_{BEND}. By extension, a range of global force-displacement responses were also accurately predicted using the CCBT method based on the local cross section deployment translation set according to the global curved-crease origami design parameters. The effect of origami design parameters was explored, it was found that the shape of the global force-displacement response is determined by the edge angle, the duration of the global force-displacement response is controlled by the edge length, and series and parallel spring effect can be achieved through modular tessellation. Together, these allow a curved-crease compliant mechanism to be designed with a fully customizable force-displacement response.

Chapter 5 Curved-crease Origami Applications in Elastic Buckling of Tubes

This chapter demonstrates the utilisation of elastica surface generation of curved-crease origami in cylinder buckling control. A curved-crease tubular geometry is first generated from a higher-order elastica, where the shape is similar to the natural deformed shape of a buckled cylinder, namely the diamond mode. A manufactured cylinder, rolled from a flat sheet, with a pre-embedded curved-crease origami pattern is then axially compressed and buckled into the pre-determined folded shape. The deformation is analysed and shown to be highly accurate to the analytical geometry. This result demonstrates that the buckling mode of a cylinder can be accurately controlled, where the crease line constraints can act as a mode director.

5.1 Introduction

5.1.1 Motivation

Specific applications capable of utilising elastica-generated curved-crease origami were sought as the final stage of this thesis. The *elastic buckling of thin-walled tubes* was identified as one, building on recent works in straight-crease (SC) tubes at Tianjin University (TJU) [129, 130]. Results of this are presented here.

5.1.2 Tubular Buckling and Origami Tubes

To explore a new platform for curved-crease origami pattern applications, this section explores the intersection of origami engineering and large deformation nonlinear mechanics in the *buckling of thin-walled tubes*. It is an interesting intersection because origami patterns can be naturally formed in some buckling modes and buckling behaviours of tubes can be controlled by origami patterns, including straight and curved-crease patterns.

5.1.2.1 Tubular Buckling

Thin-walled tubes are used in many applications across a wide range of scales and disciplines. Their excellent weight-specific structural performance characteristics sees them used as building elements [131, 132] and subsea fluid pipes [133, 134]. Their good crashworthiness behaviours see them used as energy absorption devices [135–138]. These applications all rely on a comprehensive understanding of the buckling behaviours of thin-walled tubes.

Thin-walled cylinders are the simplest form of thin-walled tube and their behaviour under axial compression has been intensively studied for decades. It has been found that their buckling modes are strongly influenced by the material properties and geometrical parameters [139], with global and local buckling behaviours determined by length-to-diameter (L/D) and diamater-to-thickness (D/t) ratios, respectively [140, 141]. For example, long slender cylinders with larger L and smaller D exhibit global buckling behaviours with mode shapes arising from lateral deformation [142]. By contrast, short and medium-length cylinders have local buckling behaviours [143], where the deformation involves the formation of progressive folds within the tube itself [144]. Two significant mode shapes are seen in local buckling, based on observations of compressed thin-walled cylinders with varying D/t ratios [140]. The axi-symmetric concertina mode (also known as the ring mode) occurs with relatively thick wall thickness $D/t < 90$ [145, 146] and the non-symmetric diamond mode (also known as the Yoshimura mode) occurs with relatively thin wall thickness $D/t > 90$ [79–81]. Interestingly, the diamond mode is a naturally formed origami tube which can be represented by tessellated triangles and unrolled to a planar origami pattern.

5.1.2.2 Origami Tubes

The buckling behaviour of thin-walled tubes can be controlled by utilising their imperfection sensitive characteristics [147]. This includes the use of non-uniform wall thickness for a functionally-graded form [148, 149], or employing cutouts, plastic folds, or dents on the surface to guide the deformation process to a predictable buckling mode [150–152]. Modern thin-walled tubes have also been combined with developable origami-inspired surface textures [153–155], where the plastically pre-folded creases can determine the mechanics of the buckling process and act as a mode director [49, 156].

Instead of using pre-folded geometries, an early concept has demonstrated that origami-inspired patterns can also be *pre-embedded* on smooth surfaces for altering the elastic buckling behaviour. Straight-crease diamond patterns, pre-embedded on thin-walled cylinders have been shown to generate a postbuckling configuration similar to the 'diamond' mode [129, 130], as shown in Fig. 5-1. It was found that the number of circumferential and longitudinal lobes n and the slant angle α are the two most important parameters for realising inwardly-deformed 'diamonds', with all tested specimens $\alpha < 45^o$ exhibiting the diamond mode failure. However, the manifested deformation was seen to include a complex curved bending region and hence the exact deformed shape was unknown. This limitation is not unique to pre-embedded tubes; for most buckling types and modes, capturing the exact shape of a postbuckled configuration is an extremely challenging problem. To overcome this limitation, Chapter 3 has suggested the possibility of the exact deformed shape of a manufactured curved-crease origami to be accurately captured using the elastica surface technique. Therefore, it is hypothesised that the shape of the postbuckled tube can be accurately pre-determined by pre-embedding curved-crease origami on the smooth surface.

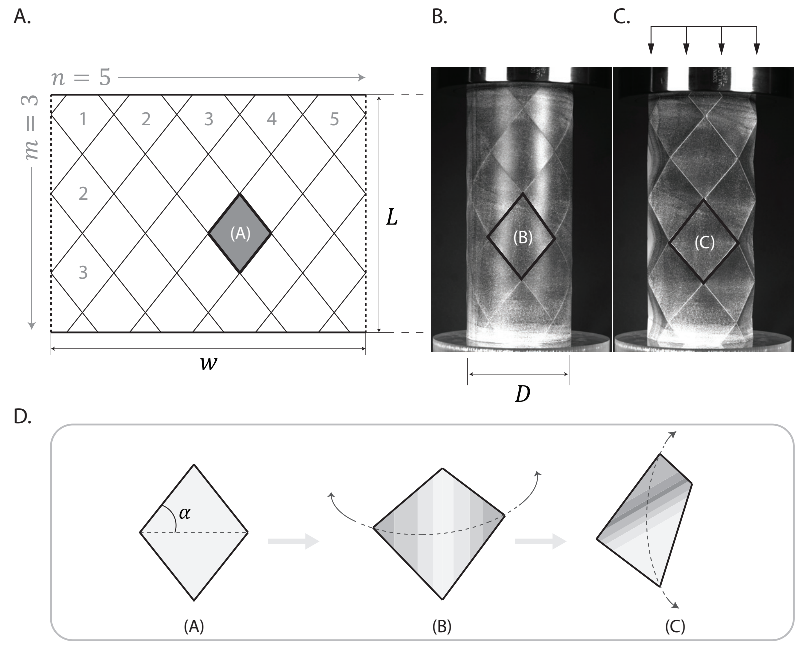

Fig. 5-1 Buckling shape control by using pre-embedded straight-crease diamond pattern. (A) 2D pattern and design parameters. (B) Undeformed cylindrical shell with design pattern. (C) Deformation when subjected to axial compression, with (D) complex curved bending regions.

5.2 Geometric Design

5.2.1 Target State Curved-crease Origami Creation

The curved-crease origami geometries utilised in this study are first modelled at their fully-folded, or 'target' state. The target state of key interest in this study is a cyclidrical tube with a pre-determined post-buckled shape. The geometric design method is as developed in Chapter 3, summarised as follows. First, a 'higher-order' elastica curve for a simply-supported slender rod is selected as shown in Fig. 5-2A. It represents the exact post-buckling geometry of a compressed beam and also a minimum bending energy configuration. The curve has three length parameters: curve length L, target state support distance b, and height of the curve away from the centreline h^*. These parameters are also related to the parameter m for determining the shape of the curve, where we only consider and enumerate even modes with a central inflection point in this study, that is m=1 is a second-mode elastica, m=2 is a fourth-mode elastica, et cetera. Specifying any three of L, b, h^*, or m gives an exact shape of a higher-order elastica curve. Extruding the curve by length w then transforms the 2D curve to a simply-supported 3D surface, as shown in Fig. 5-2B.

A higher-order mode of an elastica curve is unstable without lateral restraint, for example the $m = 2$ fourth-mode surface shown in Fig. 5-2B would be expected to snap to first-mode elastica surface if it possesses only the shown end restraints. However, a pseudo-lateral restraint and stabilising effect can be provided by *folding* the extruded surface as demonstrated in Section 3.2.4. The mirror reflection method is a technique for generation of a folded surface from a specified developable surface. A series of mirror planes are intersecting on the extruded elastica surface to control the folding angle of the folded form and identifying sequential curve folds required for tubular configurations.

The folded surface must additionally form a tubular configuration, which introduces several conditions on the specification of mirror planes. First, to give discrete individual lobes, reflection planes are constructed within the extrusion sectional height $2h^*$ as shown in Fig. 5-2C. Second, an even number of mirror planes $2n$ must be defined so that the final reflected surface has the same orientation as the initial surface, as shown in Fig. 5-2D. These constraints allow plane edge angles θ_{MB} and θ_{MA} to be found with the following relationships:

$$\theta_{MA} = \frac{\pi(n-1)}{n} \tag{5-1}$$

$$\theta_{MB} = \frac{\pi - \theta_{MA}}{2} \tag{5-2}$$

$$h^* = \frac{w\sqrt{\tan^2\theta_{MB}}}{4n} \tag{5-3}$$

Sequentially truncating and reflecting the shell about the mirror planes then gives the target folded state of the tubular curved-crease origami, where n and m determine the number of circumferential and longitudinal lobes, respectively. To summarise, the target state is generated with specification of four design parameters: w, L, m, and n. Parameters n and w give h^* from Equations 5-1-5-3, from which an elastica curve can be determined with L, m, and h^* using Equation 2-9-2-17. The higher-order elastica curve forms the non-zero principal curvature for the target curved-crease surface.

The tubular origami can be unrolled to generate a 2D pattern within a $w \times L$ sheet as shown in Fig. 5-2E. The patterned sheet can either be folded into the designed target state, or simply rolled into a thin-walled cylinder with a diameter D. The latter forms a cylindrical tube, pre-embedded with the curved-crease pattern. Therefore, there are two 3D stable states, *a curved-crease origami state* and *a cylindrical tube state*. The key hypothesis of this study is that *the target curved-crease origami state is the exact deformed shape of the cylindrical tube state*. If so, it should be obtainable by actuating the patterned cylinder with an axial compression load and at a target displacement of $l_D = L - b$. Sub-assumptions of this hypothesis include: the crease pattern is pre-embedded into the sheet without any surface pre-folding; the crease lines act as hinges and do not distort the final surface bending behaviour; and that the boundary condition is preserved as pinned-pinned as per the original elastica derivation. If this hypothesis is correct, it can be said that the post-buckled shape of a thin-walled cylinder can be precisely controlled by using a pre-embedded curved-crease origami pattern.

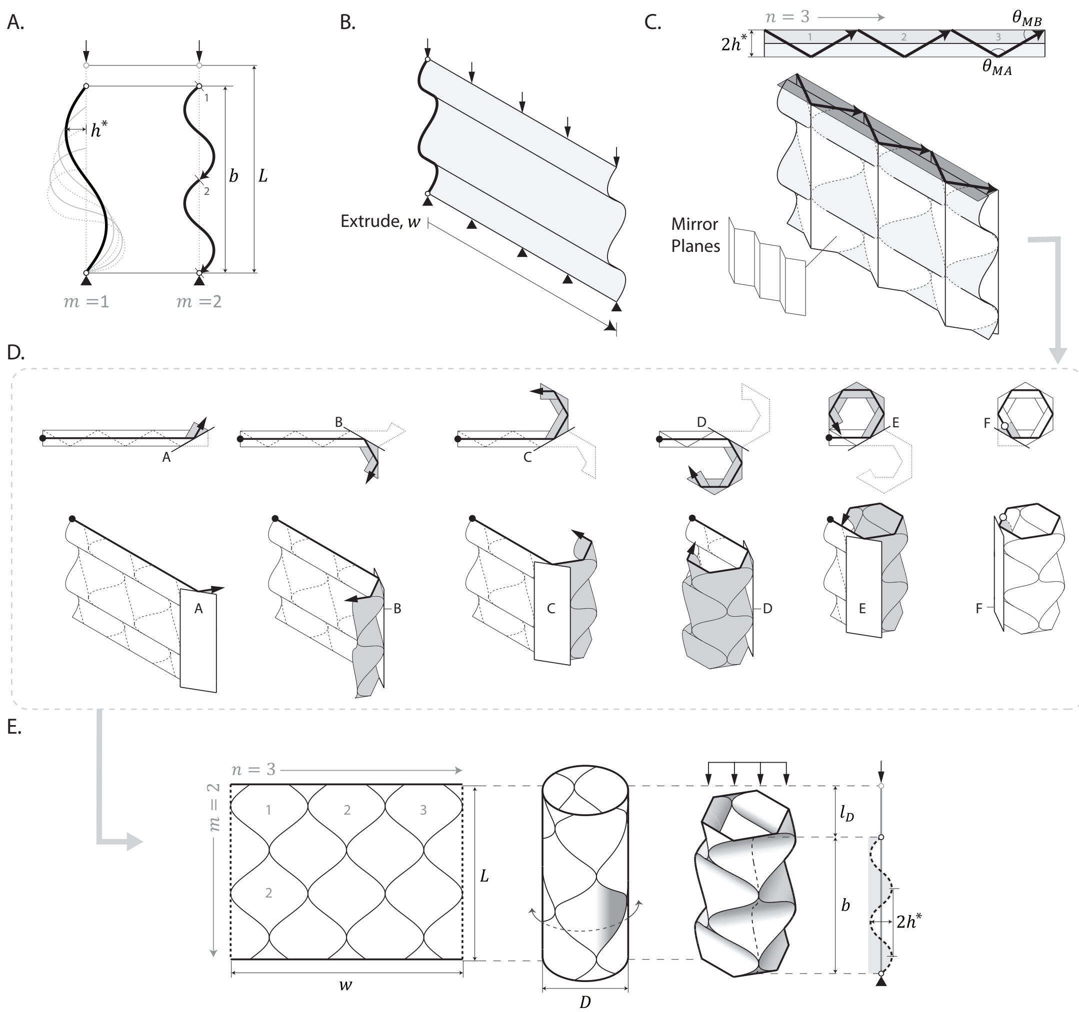

Fig. 5-2 Design procedures for tubular curved-crease origami. (A) 1D higher-order elastica curve and its design parameters. (B) An unstable bent shell extruded from the higher-order elastica curve. (C) Sequential mirror planes intersecting with the extruded shell. (D) Continuous truncation and reflection about the mirror planes, resulting in the target state curved-crease origami. (E) The unrolled pattern and its two possible forms.

5.2.2 Transformation of Curved to Straight-crease Diamond Pattern

Straight-crease (SC) diamond patterns are reproduced for the comparison with curved-crease (CC) patterns in this study. To make the two patterns comparable, the shape of target state curved lobes is transformed into diamonds by connecting the lobe boundaries with straight-line segments as shown in Fig. 5-3A-C. As the result, both patterns share a similar shape, a common sheet size, and the same number of circumferential and longitudinal lobes. Due to these characteristics, it is hypothesised that they will have a similar buckling behaviour, where the design parameter n and α strongly determine the post-bucked shape as described in Yang et al. [130]. These hypotheses will be systematically investigated in below sections.

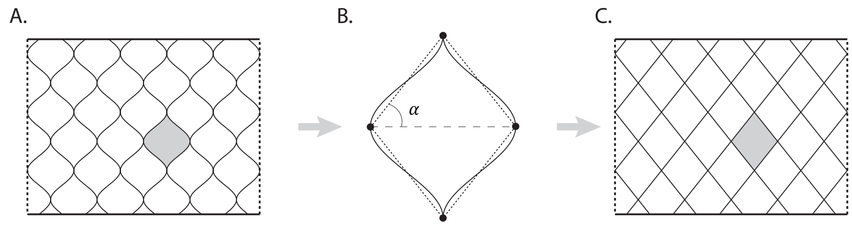

Fig. 5-3 Transformation of curved and straight-crease diamond pattern. (A) Base curved-crease 2D pattern. (B) Transformation of modular curved-lobes to diamonds. (C) Resultant straight-crease 2D pattern.

5.3 Experimental Analysis

5.3.1 Method

To investigate the buckled shape of a patterned cylinder, nine pairs of specimens (CC/SC patterns) were manufactured and tested. These patterns were selected based on SC patterns with controllable buckling modes, tested previously in [130]. They were all designed within a $w \times L$ = 278 mm × 210 mm sheet and rolled into a D/t = 294.96 cylinder with pattern design parameters summarised in Tab. 5-1. All specimens were manufactured with a t = 0.3 mm thick isotropic polypropylene sheet, which allows the requisite large elastic deformations. Crease lines were pre-embedded into the flat sheet by using a laser scoring process to reduce the material thickness along crease lines. Scored creases were approximately 0.3mm wide and 0.15-0.2mm deep on the outer tube surfaces as all crease are designed to be folded with the same direction, hence avoid the thickness interaction for unscored regions during deformation. This correspondingly reduced crease line rotational stiffnesses such that they could approximately act as ‘hinges’ during folding.

Specimens were loaded under quasi-static axial compression in an Instron Universal Testing machine with a 100kN load cell. Displacement control was used for load application, with a rate of 2 mm/min. Specimens were simply-supported between two rigid bodies, mounted on the Instron base plate and cross-head. The deformation process was captured by using a digital image correlation (DIC) system CSI Vic-3D9M, at a frame time interval of 100 milliseconds and with a 1.2/mm^2 speckle pattern [44, 130].

5.3.2 Buckling Modes and Force-displacement Responses

Tube deformations observed in tested specimens are categorised into two buckling modes based on their post-buckled shapes, summarised in Tab. 5-1. The first mode is the ‘controlled’ type as shown in Fig. 5-4A. Patterned cylinders with this mode had all lobes buckle and bend inwards when fully compressed by l_D, as per the designed curved-crease deformation mode. Patterned cylinders with such buckling mode are concluded to have a ‘shape-controllable’ feature which is a modified form of the idealised diamond buckling mode.

The second mode is the 'uncontrolled' type, where the patterned cylinder buckled without triggering, or only partially triggering, the pre-embedded lobes during the compression process as shown in Fig. 5-4C. This uncontrollable mode can be considered as similar to a typical thin-walled tube local buckling behaviour.

The force-displacement of selected CC/SC tube pairs is shown for controlled and uncontrolled modes in Fig. 5-4B and D, respectively. It is seen that CC and corresponding SC tubes share a similar force-displacement response if they are undergoing the same failure mode. Five cases show CC and SC tubes with the same controllable buckling mode: $m2n5$, $m2n6$, $m3n5$, $m3n5$, and $m3n8$. Two cases show CC and SC tubes with the same uncontrollable buckling mode: $m3n4$ and $m6n5$. Two cases have different failures with controllable buckling mode in CC tubes and uncontrollable buckling mode in SC tubes: $m1n4$ and $m4n9$.

To more closely investigate the observed differences between CC and SC buckling mode behaviours, Fig. 5-5 shows a failure map for tested specimens, plotted against key design parameters n and α. Also included are results from [130] for SC tubes with controllable buckling mode, shown shaded in grey. SC diamond mode buckling occurs where design parameters are distributed within or close to the shaded area. The design parameter range which determines diamond mode buckling in SC patterns also determines the controllable buckling mode in CC patterns. Similarly, away from the shaded region with α close to or smaller than 45^o, uncontrollable buckling mode occurs in both SC and CC tubes. Non-matching failures are shown as half-coloured dots and occur above $\alpha = 45^o$ and close to the shaded region. This suggests that the design range for controllable buckling mode can be extended by using curved-crease origami patterns, as compared with straight-crease diamond patterns.

Tab. 5-1 Design parameters and buckling mode comparison for patterned cylinders with curved and straight-crease patterns, where • = Controlled, ∘ = Uncontrolled.

m	n	α (^{o})	b/L (-)	$2h^*$ (mm)	l_D (mm)	Mode (CC, SC)
1	4	71.69	0.988	14.39	2.45	(•, ∘)
2	5	62.10	0.982	9.03	3.88	(•, •)
2	6	66.19	0.991	6.21	1.82	(•, •)
3	4	45.21	0.888	14.39	23.56	(∘, ∘)
3	5	51.54	0.958	9.03	8.86	(•, •)
3	7	60.43	0.990	4.53	2.19	(•, •)
3	8	63.60	0.994	3.46	1.27	(•, •)
4	9	59.43	0.993	2.72	1.40	(•, ∘)
6	5	32.19	0.814	9.03	39.05	(∘, ∘)

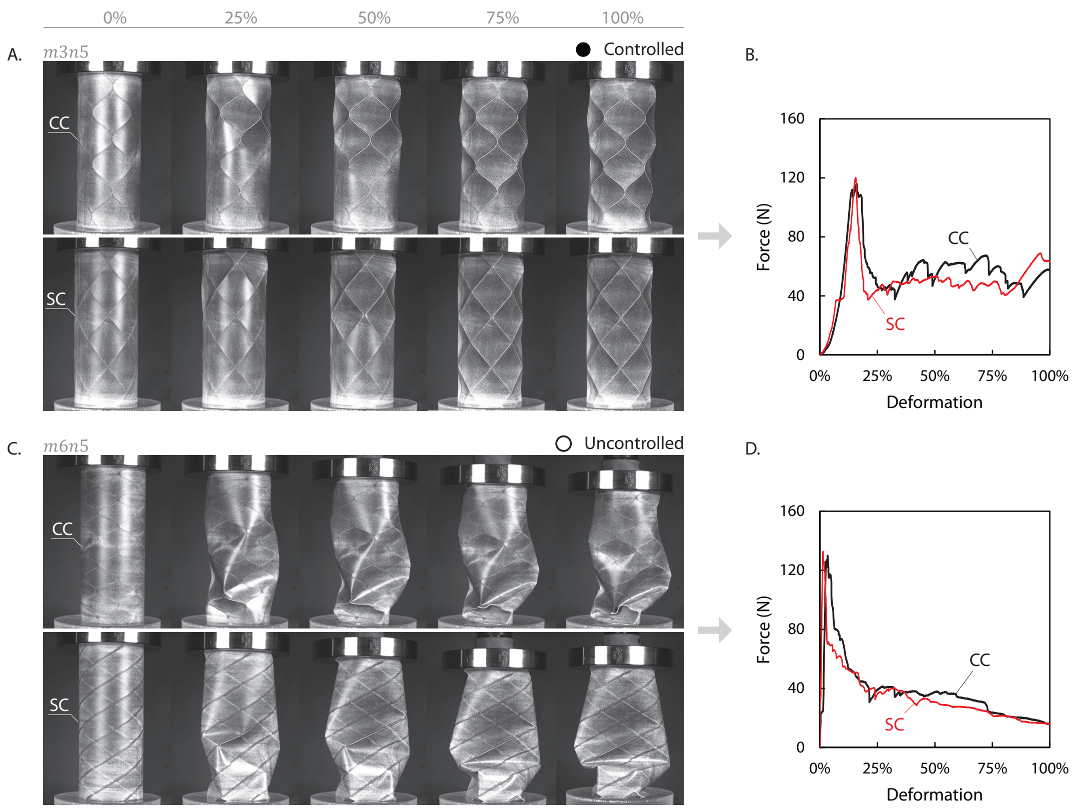

Fig. 5-4 Buckling mode classification. Left: deformation of comparable curved-crease (CC) and straight-crease (SC) patterns. Right: Force-deformation comparison of CC and SC patterns. (A-B) Demonstration of controlled type of buckling mode by using *m*3*n*5 patterns. (C-D) Demonstration of uncontrolled type of buckling mode by using *m*6*n*5 patterns.

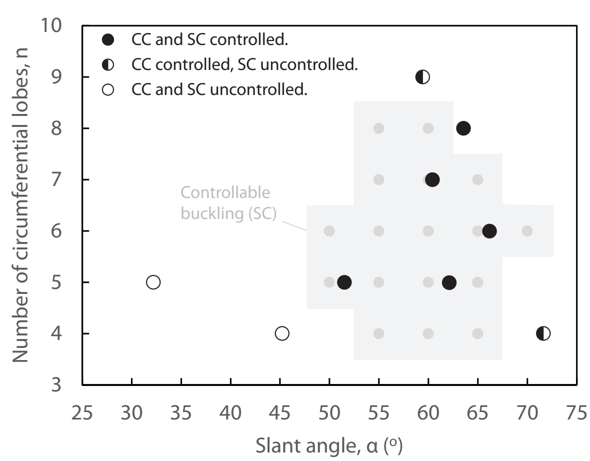

Fig. 5-5 Summary of buckling mode result comparison, where the shaded area indicates design parameters for controllable buckling mode.

5.3.3 Deformed Surface Analysis

For thin-walled cylinders achieving the controlled buckling mode, additional study was undertaken to determine the correlation between the buckled shape and the analytical folded form. The controlled buckling type $m2n5$ CC and SC specimens were selected for study, with their final deformed lobe geometry measured as point cloud data from DIC measurements. Only a single lobe was extracted from each specimen for the analysis, due to the large deformation influence on the light source reflection causing unmeasurable regions for the DIC system. The deformed lobe was measured at approximately 5,000 data extraction points and imported into a Rhino CAD environment. This was compared with the isolated analytical lobe highlighted in Fig. 5-6A, with surface error calculated as the closest line distance between the data points and the analytical surface. A 6-DOF rigid body displacement optimisation routine was used to locate analytical geometry, relative to measured geometry, so as to minimise overall surface error, as discussed in Chapter 3.

Error measurements are plotted in Fig. 5-6B as a contour diagram with colour legend from green to red for 0 to $+2t$ error, and green to blue for 0 to $-2t$ error, where sheet thickness $t = 0.3$mm. An average absolute surface error of 0.09 mm and 0.23 mm were seen for the CC and SC patterns, respectively. The correspondence for CC specimen demonstrates a high degree of design accuracy, where the average absolute surface error is within half of the sheet thickness. Therefore, it is concluded that *the post-buckling configuration of a patterned cylinder can be accurately controlled by design of a curved-crease origami pattern with a target displacement applied*.

The error analysis also shows a clear difference between the SC diamond mode and CC curved-crease mode, although these are superficially very similar and were both classed above as controllable buckling modes. The substantial surface error seen for SC lobes indicates it is not collapsing to the designed geometry. Regions of high error are seen around the crease line boundary and regions of lower error are seen in the central bent lobe area. Therefore, it can be said that the curved deformation in the SC diamond mode is generated as the straight-crease pattern relaxes toward an elastica-like minimum bending energy state. The deformation process forces straight creases to somehow deform to their closest corresponding curved-crease origami. Stronger evidence can be seen in the cross section comparison shown in Fig. 5-6C. Close correspondence to the elastica curvature is seen in the mid-region, but this reduces towards the bounding crease lines. To conclude, SC and CC pre-embedded patterns can generate a controlled buckling mode, but only elastica-generated CC patterns can give a *precise* geometric definition of the buckled surface.

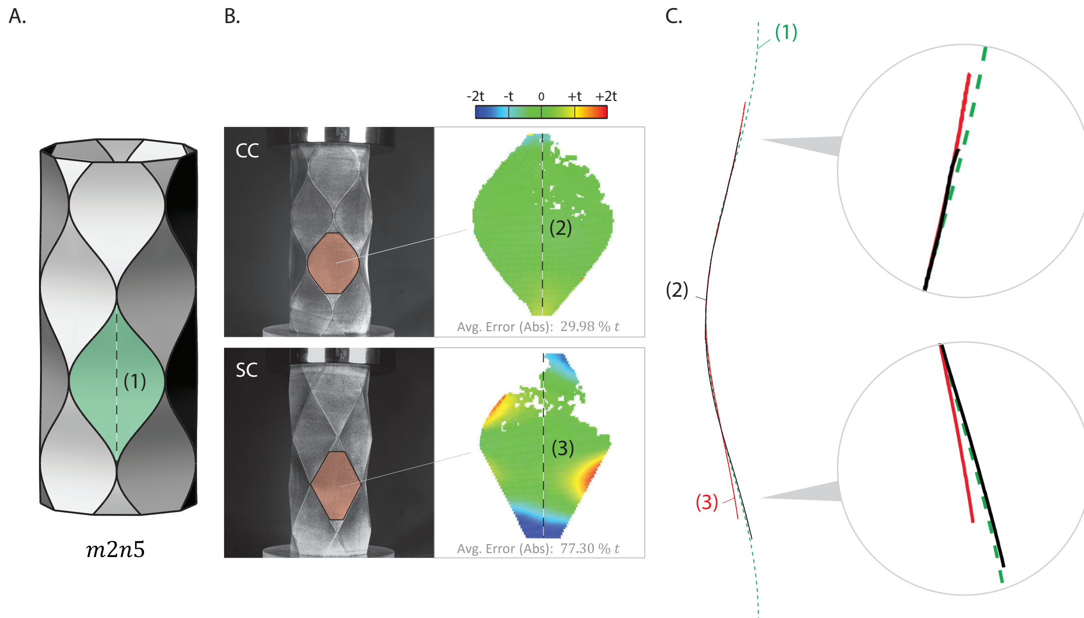

Fig. 5-6 Target state surface analysis of $m2n5$ pattern. (A) Designed geometry with elastica surface. (B) Deformation of - top: curved-crease, bot: straight-crease pattern when the target displacement has reached. (C) Cross section comparison.

5.4 Behaviour Analysis

5.4.1 Elastic Bending Energy of Deformed and Undeformed States

The difference in exhibited buckling modes was hypothesised to be related to the curvature of the lobe, which changes direction and magnitude from the undeformed to the deformed state. The undeformed lobe has a uniform curvature along the circumferential direction which is obtained from the cylindrical shell surface, denoted as κ_1 and shown in Fig. 5-7A. The deformed lobe has a non-uniform curvature along the longitudinal direction which is obtained from the elastica profile, denoted as κ_2. If $\kappa_2 > \kappa_1$, the target deformation state would have a larger surface curvature and bending strain energy potential and hence the change of bending direction may not be easily realised. However, κ_1 is a uniform value and κ_2 is a non-uniform function, so they cannot be compared in such a direct manner.

The curvature present in both undeformed and deformed lobes can be represented as an equivalent elastic bending strain energy, assuming that either state has been folded from a flat sheet with $\kappa_1 = \kappa_2 = 0$. The equation to calculate the energy U of a sheet subjected to large elastic bending has been developed previously in [157] and utilised in [130] for their SC patterns as:

$$U = \frac{Et^3}{24(1-\nu^2)} \int_{Lobe} (\kappa_x^2 + \kappa_y^2 + 2\nu\kappa_x\kappa_y)dA \tag{5-4}$$

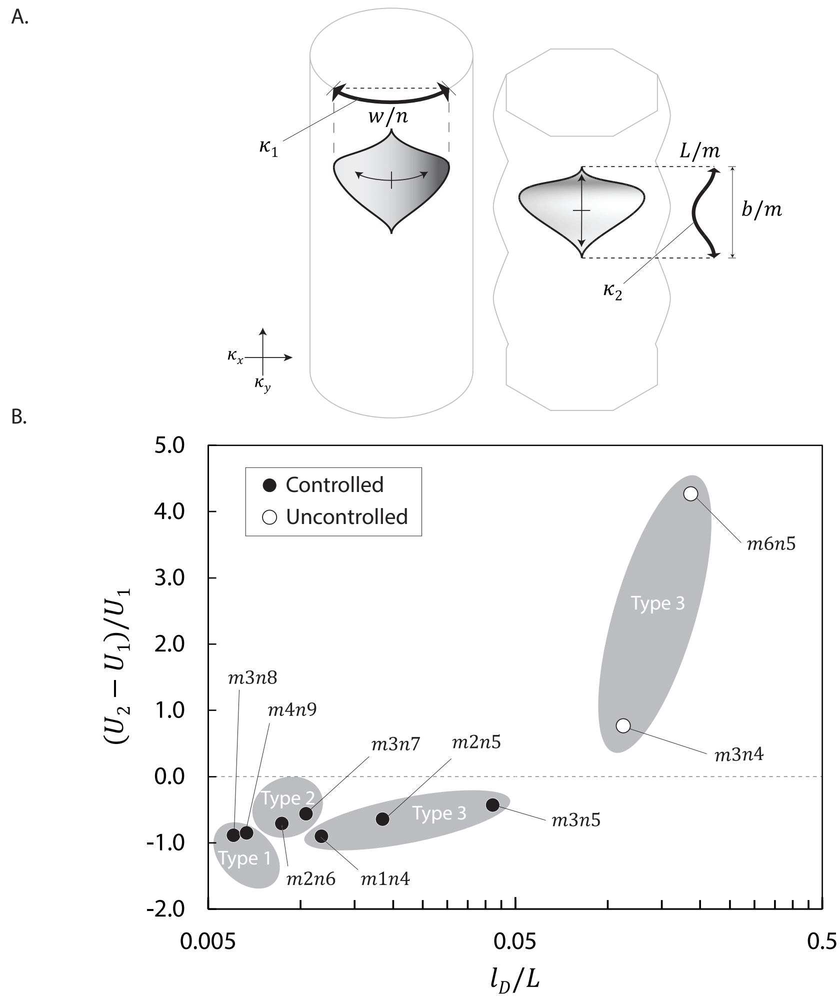

Fig. 5-7 (A) Curvature of a single lobe before and after deformation. (B) Correlation between strain energy, displacement, and buckling modes.

For the polypropylene material used in this study, Young's Modulus E = 1,260 MPa, Poisson's ratio $\nu = 0.30$, and $t = 0.30$mm. κ_x and κ_y are the curvatures along the perpendicular directions of the lobe, so the undeformed lobe has $\kappa_x = \kappa_1$ and $\kappa_y = 0$ and the deformed lobe has $\kappa_x = 0$ and $\kappa_y = \kappa_2$. The energy for undeformed and deformed lobes are denoted as U_1 and U_2, respectively.

Energy results for all tube configurations are summarised in Fig. 5-7B and Tab. 5-2. Note that force-displacement response types classification, that is Type 1, 2, and 3 behaviours, is explained in the following section. The discovery of this section is that all prototypes with $U_2 < U_1$ exhibited controllable buckling mode and conversely, all prototypes with $U_2 > U_1$ showed uncontrollable buckling mode. It is concluded that *a pre-embedded CC pattern will generate a controlled buckling shape, if that shape has a lower elastic bending strain energy potential than the initial tubular state*.

Tab. 5-2 Experimental result of different types of buckling behaviours for curved-crease patterns, where • = Controlled, ◦ = Uncontrolled.

m	n	U_1 (mJ)	U_2 (mJ)	l_D/L (-)	$(U_2 - U_1)/U_1$ (-)	Result (Type, Mode)
1	4	19.47	2.00	0.012	-0.897	(3, •)
2	5	7.79	2.81	0.018	-0.639	(3, •)
2	6	6.49	1.92	0.009	-0.704	(2, •)
3	4	6.49	11.49	0.112	**0.770**	(3, ◦)
3	5	5.19	2.97	0.042	-0.428	(3, •)
3	7	3.71	1.63	0.010	-0.561	(2, •)
3	8	3.24	0.38	0.006	-0.884	(1, •)
4	9	2.16	0.33	0.007	-0.846	(1, •)
6	5	2.60	13.68	0.186	**4.271**	(3, ◦)

5.4.2 Lobe Transition Characterisation

Examination of the force-displacement curves of curved-crease specimens can give insight into the transitional behaviour between underformed and deformed tube shapes. Fig. 5-8 shows the specimen responses up to their target state compression limit l_D, with controlled and uncontrolled buckling modes further classified based on observed force-displacement response characteristics:

- Fig. 5-8A shows specimen $m3n8$ and $m4n9$ responses. These manifest a controlled failure mode with a smooth, approximately linear region only.
- Fig. 5-8B shows specimen $m2n6$ and $m3n7$ responses. These manifest a controlled failure with an approximately linear region followed by a slightly fluctuating plateau region.
- Fig. 5-8C shows specimen $m1n4$, $m2n5$, and $m3n5$ responses. These manifest a controlled failure with a classic non-linear bucking response, with a peak load followed by sharp reduction in strength and an extended plateau region.
- Fig. 5-8D shows specimen $m3n4$ and $m6n5$ responses. These manifest an uncontrolled failure but also have a classic buckling response as described for Fig. 4-9C.

These force-displacement responses are classified Type 1, 2, and 3 behaviours for Fig. 5-8A, B, and C-D, respectively.

With reference to Fig. 5-7B, a clear trend is seen between the relative axial displacement l_D/L and the transitional behaviour. When the displacement is relatively small ($l_D/L = 0.006, 0.007$), the lobe transition is a smooth Type 1 behaviour. With increasing displacement ($l_D/L = 0.009, 0.010$), the buckling process is a less smooth Type 2 behaviour. When the displacement is relatively large ($l_D/L = 0.012, 0.018, 0.042$) but with $U_2 < U_1$, specimens undergo a controlled Type 3 behaviour. For larger displacements again, with

$U_2 > U_1$, specimens undergo an uncontrolled Type 3 behaviour. The presence of a classical buckling response indicates that a bifurcation behaviour is occurring between the tube state acting under membrane stress, and the buckled state acting under bending stress. It is hypothesised that this bifurcation is happening in all controlled specimens, but that it is more evident in specimens with a long stroke length, as a larger initial displacement and axial load can be reached in the first stable state, before transition to the second stable state.

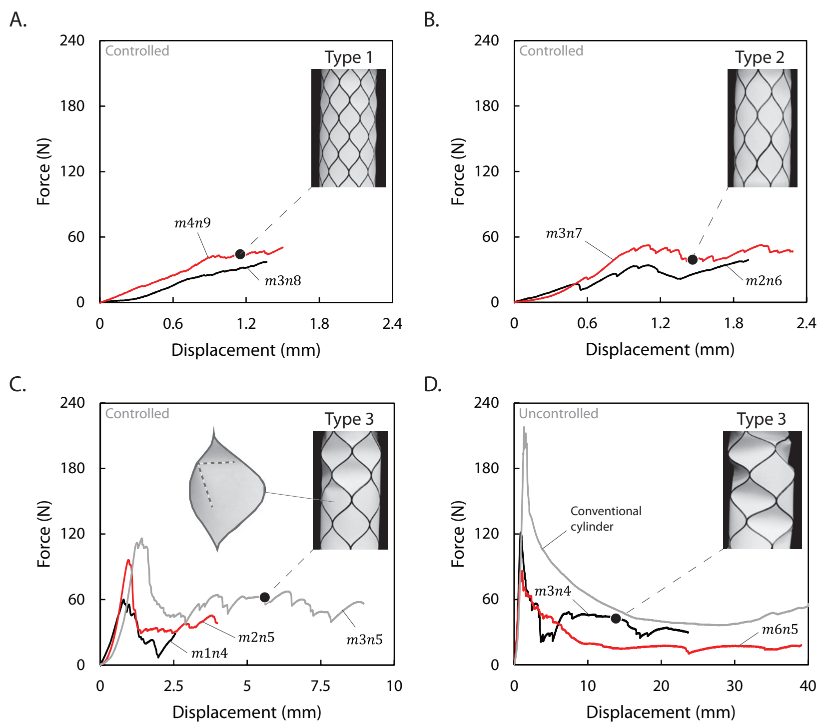

Fig. 5-8 Force-displacement comparisons for all curved-crease specimens. They are identified as (A) Type 1, (B) Type 2, (C-D) Type 3 buckling behaviour.

5.4.3 Lobe Transitional Energy Behaviour

By assessing the complete strain energy history of a lobe, the transition and hypothesised bifurcation behaviour can be more closely studied. The $m3n5$ CC/SC specimens shown in Fig. 5-4A were selected for the investigation, as they displayed the Type 3 classical non-linear buckling behaviour and so were judged likely to exhibit a clear bistability. Actual deformations were collected from the DIC system as discrete data points. These points were numerically reconstructed to a degree 5 polynomial surface, fitted with MATLAB Curve Fitting Tool, as shown in Fig. 5-9. Deformations were measured and surface-fitted at 100 frame intervals from 0 %(undeformed) to 100% (deformed) state. Equation 5-4 was used to obtaining the surface strain energy histories, with curvatures κ_x and κ_y measured at approximately 20,000 data extraction points across the surface. Remaining parameters values in Equation 5-4 were as described in Section 5.4.1.

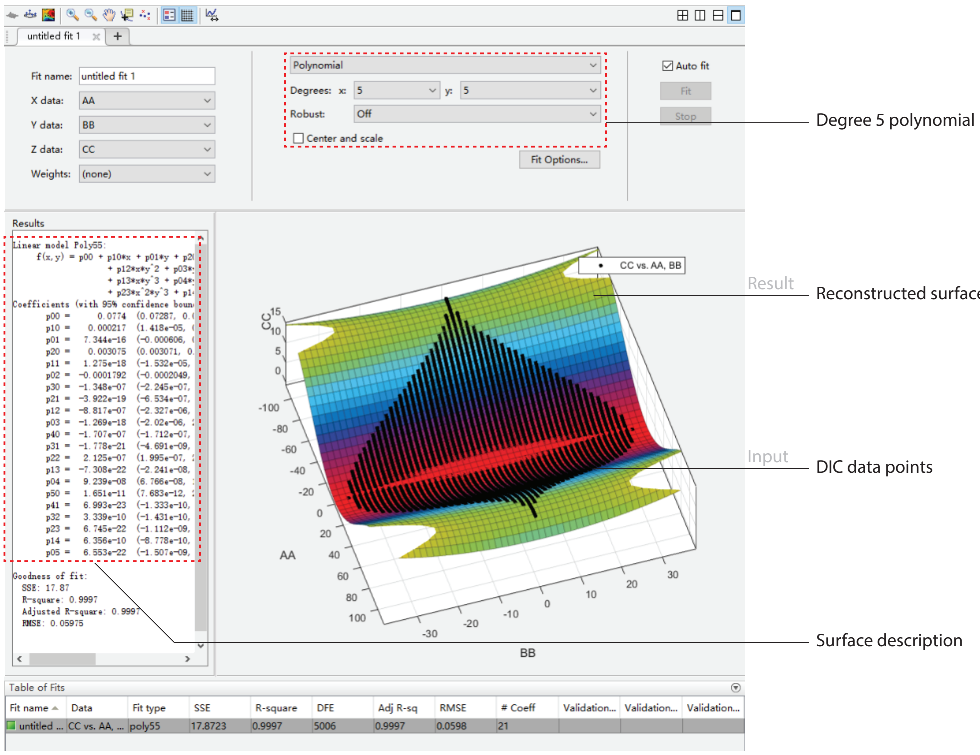

Fig. 5-9 Constructing surface from DIC data points using MATLAB Curve Fitting Tool.

The analysis results are shown in Fig. 5-10, plotted as strain energy frame interval measurements versus relative deformation. It can be seen that analytical predictions for U_1 and U_2 CC specimen strain energies have a good correspondence with the measured experimental (EXP) strain energy. This indicates the analysis and analytical methods are reliable. Both SC and CC specimens demonstrate a classic elastic snap-through behaviour at approximately 25-30% relative deformation. This is characterised by an initial stable state, here the tube energy state U_1, from which the strain energy increases as the tube is loaded. There is a sudden energy drop as the deformation snaps to a second stable state with a lower energy potential, here the curved-crease energy state U_2.

Prior to the snap-through, it can be noticed that the SC specimen has a higher energy barrier than the CC specimen, which is attributed to additional strain energy needed to deform the straight creases to allow a curved-lobe snap through. The bistability behaviour of the CC patterns is therefore relatively easier to trigger, which gives a reasonable explanation of the wider design range of curved-crease origami patterns which exhibited controlled buckling mode as highlighted in Section 5.3.2.

Following the snap-through, it can also be noticed that the strain energy histories of the CC and SC specimens are very different. Both specimens have reached the same lower energy bound. The strain energy for CC specimen remains stable afterwards, indicating the stabilised deformation was reached at a minimum of strain energy. The strain energy for SC specimens increased after the lower bound was reached, with the additional energy attributed again to straight crease lines deforming toward the curved lobe shape as shown in Fig. 5-10. The strain energy histories support the observations of Section 5.3.3, with the high surface accuracy of CC specimens arising from the stable minimum strain energy state, and the relatively low surface accuracy of SC specimens arising from the straight crease line interaction with the curved lobe shape.

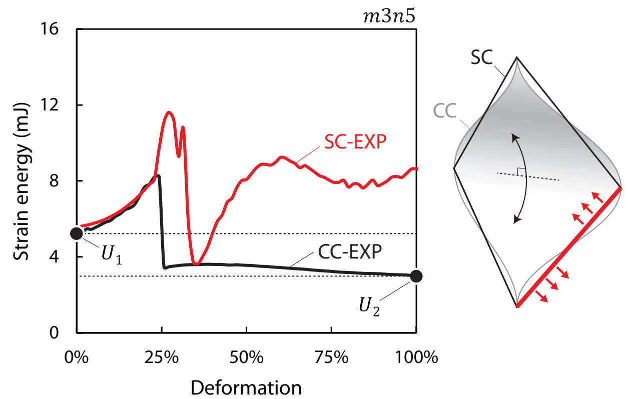

Fig. 5-10 Lobe transition behaviour during elastic buckling for CC and SC patterns.

5.4.4 Limitation in Numerical Modelling

Experimental results are commonly compared with FE (Finite Element) results to further explore the mechanics of a physical phenomenon. However, in the present study, the comparison was not made due to two reasons:

- The experimental results represent the real behaviour of the object and the presented results have clearly highlighted the corresponding key findings.
- The degree of complexity for simulating the patterned tubes is extremely high.

In general, origami structure behaviour is highly sensitive to rotational hinge line stiffness and curved-crease origami is additionally sensitive to panel thickness and material, due to its non-zero principal surface curvature. Numerical simulation would require a number of assumptions to be made about both of these items.

Ultimately, all numerical modelling assumptions have to be validated with experimental testing to ensure their accuracy. In the present case, crease properties of experimental models are complicated, where they were scored on the outer tube surface, giving a rotational stiffness is different in different (Mountain/Valley) folding directions and possibly causing a thickness interaction. This could not easily be represented in a shell-based FEM model. Another difficulty in simulating the buckling behaviours of the models is imparting imperfections, where the type of defects can largely influence the results. These include the boundary condition, surface, and crease defects. Again, they could not easily be represented in FEM models and ultimately, the experimental testing data would again be used to ensure their validity.

5.5 Conclusion

In this investigation, a new post-buckled shape control technique for thin walled cylinders has been created and validated. The technique allows for control over the buckled shape of a cylindrical tube, with the shapes shown in Fig. 5-11 all generated from the same tube by using different embedded curved-crease patterns. More significantly, the buckled shapes can be precisely described as an elastica minimum bending energy surface. A precise shape definition arose from the curved-crease geometry construction method, validated with 3D surface measurement of the deformed shape. A precise energy definition arose from a bending strain energy formulation based on undeformed and deformed surface curvature. The energy formulation was validated with the strain energy histories and this also showed the driving mechanics of the buckling process. Controlled buckling mode was seen to occur as a bistable transition from a higher strain energy tubular state to a lower strain energy curved-crease state.

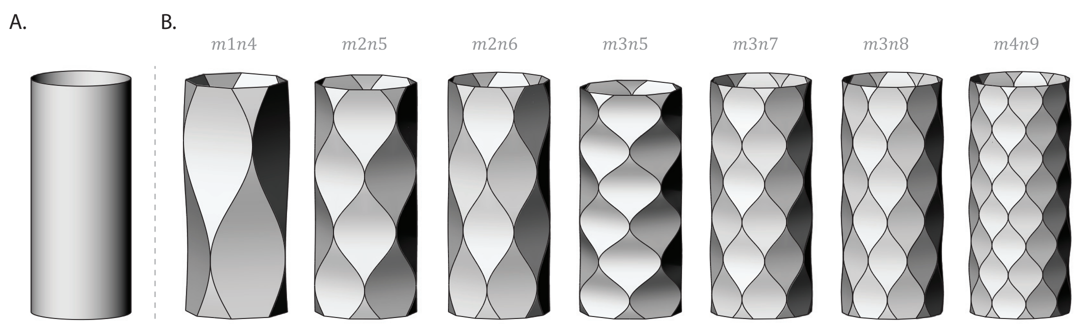

Fig. 5-11 Illustration of controllable buckling modes. (A) Undeformed cylindrical tube without pre-embedded patterns. (B) Pre-determined target folded shape for all controlled tubes.

Chapter 6 Conclusion

In this thesis, a set of curved-crease patterns were accurately modelled and analysed. This was achieved by adopting elastica curves, the deformed shapes of an elastically-deformed slender rod, as the generating curvatures for curved-crease pattern construction. This approach is shown to enable several key advancements in characterisation of pattern behaviour. Major findings and contributions of this thesis are briefly summarised and followed by future research implications which conclude the thesis.

6.1 Summary of Findings

6.1.1 Modelling of Curved-crease Origami using Elastica Curves

Chapter 3 developed a new analytical geometric construction method for modelling near-exact surface representation of folded curved-crease origami surfaces, termed *elastica surface generation of curved-crease origami*. This method allowed curved-crease origami to be designed for a specific form and target volume by transforming base straight-crease origami patterns into their curved-crease variants. A new compressibility limit of curved-crease surfaces was identified with an upper limit of $\Theta = \pi/2$. An experimental surface analysis showed that the design accuracy can be controlled within 50% of the 2mm sheet thickness with a range of elastica surface curved-crease origami. It was found that the proposed method is highly reliable if 3D curved-crease origami surfaces are elastically-bent and preserve boundary conditions as per the utilised elastica solution. It was also found that an unstable higher-order mode of elastica surface can be stabilised using a curved-crease constraint.

Extensions of the method were explored and included numerical folding motion simulation and an investigation of a free edge distortion behaviour which occurred in certain origami forms. The free edge effect was found to distort bending behaviour if the free edge was not parallel to the elastica construction plane. This was demonstrated for both linearly-extruded elastica surfaces and 3D reflected curved-crease origami surfaces. If the free edge inclination is small in comparison to the extruded surface length, it would be expected to have a minimal, localised impact. It was also found that developable tubular origami geometries, which effectively remove free edges, would avoid distortion completely.

6.1.2 Curved-crease Origami Folding Mechanics

Chapter 4 explored the folding mechanics of elastically-bent curved-crease origami by examining the intersection between surface's minimum bending behaviour and developability-constrained behaviour. It was shown that a curved-crease folding motion has a lower (U_{BEND}) and upper (U_{PRBM}) bound energy behaviour depending on the enforcement condition of surfaces. It was then shown that the actual model had an energy behaviour between U_{BEND} and U_{PRBM}, as the developability condition cannot be exactly enforced. By adopting the elastica curve as the non-zero principal curvature of curved-crease origami, it was found that the local cross section deformations with and without developability constraints are suitably close to each other during motion. This allowed the energy response of an *elastica surface origami* to be accurately predicted.

A new CCBT method for analytically translating a predictable energy response to a global force-displacement response was then developed. A range of non-linear force-displacement responses were shown to be accurately predicted using elastica surface origami with different origami design parameters. It was found that the edge angle determines the global force-displacement response type, where a hardening, plastic, and softening response was seen for η_A greater than, equals to, and smaller than 90 ^{o}, respectively. It was shown that the edge length determines the the displacement capacity of the force-displacement response. It was also shown that a series, parallel, or combined non-linear mechanical spring effect can be achieved through modular tessellation. These origami parameter effects were then demonstrated for designing an elastica surface origami with a customizable global force-displacement response.

6.1.3 Curved-crease Origami Applications in Elastic Buckling of Tubes

Chapter 5 presented a new shape control technique for post-buckled tubes by using *pre-embedded* curved-crease origami patterns. It was found that the buckled shapes can be precisely pre-determined as an elastica minimum bending energy surface. The pre-determined deformation was shown to be highly accurate within 50% of the 0.3mm material thickness. An energy definition for analysing the driving mechanics of the buckling process was formulated based on undeformed and deformed surface curvature. It was found that a controlled buckling mode had a bistable transition from a higher strain energy tubular state to a lower strain energy curved-crease state.

Results from this chapter have also built upon other recent findings in folded surface mechanics. First, the pre-embedded technique with straight-crease embedded patterns was seen in [129] to produce controlled diamond buckling over a finite parameter range for n and α. Results in this study show that this controlled buckling range arises as a function of bending strain energy and a bistable transition between tubular and deformed states. The straight-crease buckling mode was found to be similar to the curved-crease mode, but with additional strain energy from crease line deformation. Correspondingly, it was found that the deformed shape had a larger energy barrier and final strain energy as compared to the minimum-energy curved-crease shapes. Second, this study has demonstrated that curved folds provide a stabilising effect for the higher-degree elastica surface shapes. This was hypothesised in Chapter 3, however this earlier study was only able to validate a second-order elastica surface stabilised through pre-folding. The current study has validated up to an eighth-order elastica surface, stabilised through pre-embedding.

6.2 Summary of Contributions

The contributions of the thesis are briefly summarised as the following three conclusions:

- A new concise and accurate analytical description of manufactured curved-crease origami surface was presented by using a curvature representing surface elastic bending behaviours. This allows users to effectively design and pre-define the exact folded shape of a curved-crease pattern for a specific form and target volume.
- The first characterisation of elastic strain energy and folding motion in curved-crease compliant mechanisms was presented. By extension, a novel method was presented for preserving the surface minimum bending behaviour under a developability-constrained condition, which allows compliant folding behaviours of curved-crease origami to be concisely and precisely captured.
- A novel elastic buckling shape control method for thin-walled cylinder was presented. This allows elastic buckling of thin-walled cylinders to be accurately guided to a pre-determined shape by using an embedded elastica surface curved-crease origami pattern, which also offers a strong platform for new origami pattern applications.

6.3 Potential Applications

Curved-crease origami is a relatively new area of study and knowledge in critical areas is evolving quickly. This thesis has made a significant contribution particular in the field of accurately/analytically capturing large nonlinear deformation with developability constraint. However, this thesis does not go into depth about specific design and application examples. It is believed that existing curve-crease applications can be improved using the new knowledge. For example,

- Target state modelling: With reference to Fig. 1-1C, 1-1E, and 2-1I, the elastica surface technique can be applied on folded façade, thin-walled structure, and car shell, respectively, for pre-defining their exact shapes. This then allows engineers, architects, and designers to have an accurate digital model for ease of further analysis such as load-carrying behaviour, shading performance, and aesthetic judgement. It should be noted that there are many other curved-crease origami geometries which can be designed using the elastica surface and have a great potential for static applications.

- Compliant folding behaviour: With reference to Fig. 1-1A and 1-1D, the CCBT method can be applied on curved-crease deployable structures ranging from small-scale medical forceps to building-scale shelters for capturing their compliant folding behaviours. This method also allows the shape and folding behaviours of a curved-crease deployable structure to be pre-defined. That is to say, the CCBT method is suitable for applications where a desired shape or expected performance is specified.
- Elastic buckling shape control: Folding a complex origami pattern as the deployment methodology is labour-intensive, time-consuming and highly skill-demand. However, the new elastic buckling shape control method allows a patterned sheet to be easily deformed to a pre-defined shape, hence it can be considered as an advanced manufacturing method. With reference to Fig. 2-1E, there is a large potential that the origami tube can be assembled using the shape control method before its experimental testing. This method can also be applied on a range of curved-crease decorative components for reducing the manufacturing effort.

Above potential curved-crease applications with the new knowledge are all based on a common assumption, that is *panels are elastically-bent using isotropic materials and crease lines are acting as a zero rotational stiffness without thickness interaction*. A range of materials are suitable for realising this assumption and applications are not limited to scale according to the elastica theory. However, further investigation is needed to examine this. Finally, a brief summary of potential future work is discussed in the following section to conclude the thesis.

6.4 Future Work

This thesis has established results for a range of elastica surface origami with their shapes and folding behaviours to be accurately designed, and as such has suggest numerous avenues for future research.

First, this thesis has only utilised a pinned-pinned elastica curve with a constant flexural rigidity EI to construct various curved-crease surfaces. A range of elastica solutions exist for other boundary conditions, including (1) fixed-fixed, (2) fixed-pinned, and (3) fixed-free conditions and for incorporation of axial and shear deformation terms within the elliptic integral [158] or non-uniform flexural rigidity caused by cross section (I) or material (E) variation [159, 160]. These elastica curves can be adopted as the non-zero principal curvature, which can potentially further improve accuracy and extend the range of curved-crease origami geometries which can be specified analytically. Further study is needed to develop this.

Second, a substantial limitation of the curved-crease creation method proposed in Chapter 3 is that a straight-crease base pattern needs to be known *a priori* to generate the required reflection planes and elastica design parameters. Whilst extensive families of straight-crease patterns are known and accessible, the method is fundamentally unsuited to generative forms of origami-inspired engineering design where an approximate straight-crease origami geometry is as-yet unknown or where the precise final design state is unconstrained or not of primary interest. However, the method is highly suitable for parametric forms of origami-inspired engineering design, as an explicit relationship between crease pattern parameters (for example as required for manufacture) and volumetric parameters of the design state (for example as required for 3D surface modelling and engineering analysis) can be established relatively simply in a simplified straight-crease form and then ‘converted’ to an accurate curved-crease form which may have a higher performative capacity. The combination of generative and parametric design systems is an as-yet unexplored topic in origami-inspired design.

Third, this thesis has only considered tubular behaviours for elastic buckling up to the target deformation, as shown in Chapter 5. If deformed tubes are further compressed, the pre-embedded crease lines and generated modes are likely to have some impact on subsequent plastic deformation and energy absorption. This study also only considered pre-embedded creases with approximately zero rotational stiffness. This was necessary to isolate bending strain energy behaviours, but buckling control might be possible with higher-stiffness creases. This would likely impact the peak elastic buckling load with further study needed to understand, predict, and control the peak failure load. To this end, further research on the intermediate behaviours throughout the buckling process is required, which potentially involves a robust numerical simulation method.

Finally, the pre-embedded technique can potentially be applied to other types of developable tubes not just for cylindrical tubes, such as polygonal hollow sections, tapered tubes, and tubes with different lengths. Additional common features in deformable tubes are also likely to interact with potential pre-embedded patterns, for example slotted or windowed tubes. In each cash, a different pre-determined configuration would be needed to reach to a permissible minimum bending energy state. These permissible states may be attainable with elastica solutions for different boundary conditions.

References

[1] Schleicher S, Lienhard J, Poppinga S, *et al*. A methodology for transferring principles of plant movements to elastic systems in architecture [J]. Computer-Aided Design, 2015, 60: 105–117.

[2] Nelson T G, Lang R J, Magleby S P, *et al*. Curved-folding-inspired deployable compliant rolling-contact element (D-CORE) [J]. Mechanism and Machine Theory, 2016, 96: 225–238.

[3] Nelson T G, Lang R J, Pehrson N A, *et al*. Facilitating deployable mechanisms and structures via developable lamina emergent arrays [J]. Journal of Mechanisms and Robotics, 2016, 8 (3): 031006.

[4] Miyashita S, DiDio I, Ananthabhotla I, *et al*. Folding angle regulation by curved crease design for self-assembling origami propellers [J]. Journal of Mechanisms and Robotics, 2015, 7 (2): 021013.

[5] Gattas J, You Z. The behaviour of curved-crease foldcores under low-velocity impact loads [J]. International Journal of Solids and Structures, 2015, 53: 80–91.

[6] Garrett D, You Z, Gattas J M. Curved Crease Tube Structures as an Energy Absorbing Crash Box [C]. In ASME 2016 International Design Engineering Technical Conferences and Computers and Information in Engineering Conference, 2016: V05BT07A017–V05BT07A017.

[7] Vergauwen A, Alegria Mira L, Roovers K, *et al*. Parametric design of adaptive shading elements based on Curved-line Folding [C]. In Proceedings of the First Conference Transformables 2013, 2013.

[8] Epps G, Verma S. Curved Folding: Design to fabrication process of RoboFold [J]. Shape Modeling International 2013, 2013: 75.

[9] Lee T, Gattas J. Folded fabrication of composite curved-crease components [C]. In International Conference on Fibre-Reinforced Polymer (FRP) Composites in Civil Engineering, 2016: 1430–1435.

[10] Kilian M, Flöry S, Chen Z, *et al*. Curved folding [J]. ACM transactions on graphics (TOG), 2008, 27 (3): 75.

[11] Kilian M, Monszpart A, Mitra N J. String actuated curved folded surfaces [J]. ACM Transactions on Graphics (TOG), 2017, 36 (3): 25.

[12] Duncan J, Duncan J. Folded developables [C]. In Proc. R. Soc. Lond. A, 1982: 191–205.

[13] Tachi T. Composite rigid-foldable curved origami structure [C]. In 1st International Conference on Transformable Architecture (Transformables 2013), Seville, Spain, Sept, 2013: 18–20.

[14] Lienhard J. Bending-active structures: form-finding strategies using elastic deformation in static and kinetic systems and the structural potentials therein [M]. 2014.

[15] Hansen B, Tan J, Gattas J, *et al*. Folded fabrication of FRP-timber thin-walled beams with novel non-uniform cross-sections [C]. In World Conference on Timber Engineering, 2016.

[16] Bruton J T, Nelson T G, Zimmerman T K, *et al*. Packing and deploying Soft Origami to and from cylindrical volumes with application to automotive airbags [J]. Royal Society Open Science, 2016, 3 (9): 160429.

[17] Walker M G, Seffen K A. Bistable behaviour of creased thin metallic strips [C]. In Proceedings of the IASS Annual Symposium 2017 ”Interfaces: architecture, engineering, science”, 2017.

[18] Cui W, Gfeller T, Fernando D, *et al*. Folding Fabrication of Curved-Crease Origami Spindle Beams [C]. In Origami 7: Seventh International Meeting of Origami Science, Mathematics, and Education, 2018: 1329–934.

[19] Lienhard J, Schleicher S, Poppinga S, *et al*. Flectofin: a hingeless flapping mechanism inspired by nature [J]. Bioinspiration & biomimetics, 2011, 6 (4): 045001.

[20] Tachi T, Epps G. Designing One-DOF mechanisms for architecture by rationalizing curved folding [C]. In International Symposium on Algorithmic Design for Architecture and Urban Design (ALGODE-AIJ). Tokyo, 2011.

[21] Gattas J M, You Z. Miura-base rigid origami: parametrizations of curved-crease geometries [J]. Journal of Mechanical Design, 2014, 136 (12): 121404.

[22] Fleischmann M, Knippers J, Lienhard J, *et al*. Material behaviour: embedding physical properties in computational design processes [J]. Architectural Design, 2012, 82 (2): 44–51.

[23] Rothemund P W. Folding DNA to create nanoscale shapes and patterns [J]. Nature, 2006, 440 (7082): 297.

[24] Zirbel S A, Lang R J, Thomson M W, *et al*. Accommodating thickness in origami-based deployable arrays [J]. Journal of Mechanical Design, 2013, 135 (11): 111005.

[25] Quaglia C, Yu N, Thrall A, *et al*. Balancing energy efficiency and structural performance through multi-objective shape optimization: Case study of a rapidly deployable origami-inspired shelter [J]. Energy and Buildings, 2014, 82: 733–745.

[26] Thrall A, Quaglia C. Accordion shelters: A historical review of origami-like deployable shelters developed by the US military [J]. Engineering structures, 2014, 59: 686–692.

[27] Kuribayashi K, Tsuchiya K, You Z, *et al*. Self-deployable origami stent grafts as a biomedical application of Ni-rich TiNi shape memory alloy foil [J]. Materials Science and Engineering: A, 2006, 419 (1-2): 131–137.

[28] Edmondson B J, Bowen L A, Grames C L, *et al*. Oriceps: Origami-inspired forceps [C]. In ASME 2013 conference on smart materials, adaptive structures and intelligent systems, 2013: V001T01A027–V001T01A027.

[29] Johnson M, Chen Y, Hovet S, *et al*. Fabricating biomedical origami: a state-of-the-art review [J]. International journal of computer assisted radiology and surgery, 2017, 12 (11): 2023–2032.

[30] Wilson L, Pellegrino S, Danner R. Origami sunshield concepts for space telescopes [C]. In 54th AIAA/ASME/ASCE/AHS/ASC Structures, Structural Dynamics, and Materials Conference, 2013: 1594.

[31] Morgan J, Magleby S P, Howell L L. An approach to designing origami-adapted aerospace mechanisms [J]. Journal of Mechanical Design, 2016, 138 (5): 052301.

[32] Lee D-Y, Kim J-S, Kim S-R, *et al*. The deformable wheel robot using magic-ball origami structure [C]. In ASME 2013 international design engineering technical conferences and computers and information in engineering conference, 2013: V06BT07A040–V06BT07A040.

[33] Belke C H, Paik J. Mori: a modular origami robot [J]. IEEE/ASME Transactions on Mechatronics, 2017, 22 (5): 2153–2164.

[34] Schenk M, Guest S D. Geometry of Miura-folded metamaterials [J]. Proceedings of the National Academy of Sciences, 2013, 110 (9): 3276–3281.

[35] Overvelde J T, De Jong T A, Shevchenko Y, *et al*. A three-dimensional actuated origami-inspired transformable metamaterial with multiple degrees of freedom [J]. Nature communications, 2016, 7: 10929.

[36] Lang R J. Origami: Complexity in creases (again) [J]. Caltech/Engineering and Science magazine, 2004, 67 (1): 5–19.

[37] Lang R J. Origami design secrets: mathematical methods for an ancient art [M]. AK Peters/CRC Press, 2011.

[38] Mitani J. 3D origami art [M]. AK Peters/CRC Press, 2016.

[39] Sorguç A G, Hagiwara I, Selcuk S. Origamics in architecture: a medium of inquiry for design in architecture [J]. Metu Jfa, 2009, 2: 235–247.

[40] Reis P M, Jiménez F L, Marthelot J. Transforming architectures inspired by origami [J]. Proceedings of the National Academy of Sciences, 2015, 112 (40): 12234–12235.

[41] Chen Y, Peng R, You Z. Origami of thick panels [J]. Science, 2015, 349 (6246): 396–400.

[42] Liu X, Gattas J M, Chen Y. One-DOF superimposed rigid origami with multiple states [J]. Scientific reports, 2016, 6: 36883.

[43] Rejab M, Cantwell W. The mechanical behaviour of corrugated-core sandwich panels [J]. Composites Part B: Engineering, 2013, 47: 267–277.

[44] Shi Q, Shi X, Gattas J M, *et al*. Folded assembly methods for thin-walled steel structures [J]. Journal of Constructional Steel Research, 2017, 138: 235–245.

[45] Gattas J, You Z. Quasi-static impact response of alternative origami-core sandwich panels [J]. ASME Paper No. DETC2013-12681, 2013.

[46] Miura K. The science of Miura-ori: A review [J]. Origami, 2009, 4: 87–100.

[47] Seymour K, Burrow D, Avila A, *et al*. Origami-Based Deployable Ballistic Barrier [C]. 2018.

[48] Buri H, Weinand Y. ORIGAMI—Folded plate structures, architecture [C]. In 10th World Conference on Timber Engineering, 2008: 2–5.

[49] Yang K, Xu S, Shen J, *et al*. Energy absorption of thin-walled tubes with pre-folded origami patterns: Numerical simulation and experimental verification [J]. Thin-Walled Structures, 2016, 103: 33–44.

[50] Lee T, Gattas J. Geometric design and construction of structurally stabilized accordion shelters [J]. Journal of Mechanisms and Robotics, 2016, 8 (3): 031009.

[51] Demaine E D, Demaine M L, Koschitz D, *et al*. Curved crease folding: a review on art, design and mathematics [C]. In Proceedings of the IABSE-IASS Symposium: Taller, Longer, Lighter (IABSE-IASS2011), London, England, Sept, 2011: 20–23.

[52] Demaine E, Demaine M, Koschitz D. Reconstructing David Huffman’s legacy in curved-crease folding [J]. Origami, 2011, 5: 39–52.

[53] Weinand Y. Innovative timber constructions [J]. journal of the International Association for Shell and Spatial Structures, 2009, 50 (2): 111–120.

[54] Buri H U, Stotz I, Weinand Y. Curved folded plate timber structures [C]. In IABSE-IASS 2011 London Symposium, 2011.

[55] Schenk M, Allwood J, Guest S. Cold gas-pressure folding of Miura-ori sheets [C]. In Proceedings of International Conference on Technology of Plasticity (ICTP 2011), Sept, 2011: 25–30.

[56] Gattas J, Lv W, Chen Y. Rigid-foldable tubular arches [J]. Engineering Structures, 2017, 145: 246–253.

[57] Vergauwen A, De Laet L, De Temmerman N. Computational modelling methods for pliable structures based on curved-line folding [J]. Computer-Aided Design, 2017, 83: 51–63.

[58] Pellegrino S. New concepts for spacecraft antennas and radar structures based on ultra-thin composites [C]. In Department of Engineering, Noordjwick, Netherland, 28th ESA Antenna Workshop on space antenna system & technologies, 31May-3June, 2005.

[59] Heimbs S, Cichosz J, Klaus M, *et al*. Sandwich structures with textile-reinforced composite foldcores under impact loads [J]. Composite structures, 2010, 92 (6): 1485–1497.

[60] Lang R J. A computational algorithm for origami design [C]. In Proceedings of the twelfth annual symposium on Computational geometry, 1996: 98–105.

[61] Lang R J. Twists, tilings, and tessellations: mathematical methods for geometric origami [M]. AK Peters/CRC Press, 2017.

[62] Turner N, Goodwine B, Sen M. A review of origami applications in mechanical engineering [J]. Proceedings of the Institution of Mechanical Engineers, Part C: Journal of Mechanical Engineering Science, 2016, 230 (14): 2345–2362.

[63] Huffman D A. Curvature and creases: A primer on paper [J]. IEEE Trans. Computers, 1976, 25 (10): 1010–1019.

[64] Miura K. A note on intrinsic geometry of origami [J]. Research of Pattern Formation, 1989: 91–102.

[65] Watanabe N, Kawaguchi K-i. The method for judging rigid foldability [J]. Origami, 2009, 4: 165–174.

[66] Tachi T. Generalization of rigid-foldable quadrilateral-mesh origami [J]. Journal of the International Association for Shell and Spatial Structures, 2009, 50 (3): 173–179.

[67] Tachi T. Freeform rigid-foldable structure using bidirectionally flat-foldable planar quadrilateral mesh [J]. Advances in architectural geometry 2010, 2010: 87–102.

[68] Dai J S, Jones J R. Mobility in metamorphic mechanisms of foldable/erectable kinds [J]. Journal of Mechanical Design, 1999, 121 (3): 375–382.

[69] Liu S, Chen Y, Lu G. The rigid origami patterns for flat surface [J]. ASME Paper No. DETC2013-12947, 2013.

[70] Chen Y, Lv W, Li J, *et al*. An extended family of rigidly foldable origami tubes [J]. Journal of Mechanisms and Robotics, 2017, 9 (2): 021002.

[71] Miura K. Method of packaging and deployment of large membranes in space [J]. Title The Institute of Space and Astronautical Science Report, 1985, 618: 1.

[72] Wu W. Rigid origami: modelling, application in pre-folded cylinders and manufacturing [D]. [S. l.]: Oxford University, 2010.

[73] Gattas J M, Wu W, You Z. Miura-base rigid origami: parameterizations of first-level derivative and piecewise geometries [J]. Journal of mechanical design, 2013, 135 (11): 111011.

[74] Klett Y, Drechsler K. Designing technical tessellations [C]. In Origami 5: Fifth International Meeting of Origami Science, Mathematics, and Education, 2011: 305–322.

[75] Ma J, Song J, Chen Y. An origami-inspired structure with graded stiffness [J]. International Journal of Mechanical Sciences, 2018, 136: 134–142.

[76] Hanna B H, Lund J M, Lang R J, *et al*. Waterbomb base: a symmetric single-vertex bistable origami mechanism [J]. Smart Materials and Structures, 2014, 23 (9): 094009.

[77] Silverberg J L, Na J-H, Evans A A, *et al*. Origami structures with a critical transition to bistability arising from hidden degrees of freedom [J]. Nature materials, 2015, 14 (4): 389.

[78] Liu K, Paulino G. Nonlinear mechanics of non-rigid origami: an efficient computational approach [J]. Proc. R. Soc. A, 2017, 473 (2206): 20170348.

[79] Yoshimura Y. On the mechanism of buckling of a circular cylindrical shell under axial compression [J], 1955.

[80] Miura K. Proposition of pseudo-cylindrical concave polyhedral shells [M]. Institute of Space and Aeronautical Science, University of Tokyo, 1969.

[81] Seffen K, Stott S. Surface texturing through cylinder buckling [J]. Journal of Applied Mechanics, 2014, 81 (6): 061001.

[82] Kresling B. Natural Twist Buckling in Shells: From the Hawkmoth’s Bellows to the Deployable Kresling-Pattern and Cylindrical Miuraori [C]. In Proceedings of the 6th International Conference on Computation of Shell and Spatial Structures, John F. Abel and J. Robert Cooke, eds., Ithaca, 2008.

[83] Feng H. Kinematics of spatial linkages and its applications to rigid origami [D]. [S. l.]: Tianjin University, 2018.

[84] Koschitz D, Demaine E D, Demaine M L. Curved crease origami [J]. Advances in Architectural Geometry, 2008: 29–32.

[85] Dias M A, Dudte L H, Mahadevan L, *et al*. Geometric mechanics of curved crease origami [J]. Physical Review Letters, 2012, 109 (11): 114301.

[86] Fuchs D, Tabachnikov S. More on paperfolding [J]. The American Mathematical Monthly, 1999, 106 (1): 27–35.

[87] Mitani J, Igarashi T. Interactive design of planar curved folding by reflection [C]. In Pacific Conference on Computer Graphics and Applications-Short Papers, Kaohsiung, Taiwan, September, 2011: 21–23.

[88] Koschitz R D. Computational design with curved creases: David Huffman's approach to paperfolding [D]. [S. l.]: Massachusetts Institute of Technology, 2014.

[89] Gauss C F. Disquisitiones generales circa superficies curvas [M]. Typis Dieterichianis, 1828.

[90] Euler L. De solidis quorum superficiem in planum explicare licet [J]. Novi commentarii academiae scientiarum Petropolitanae, 1772: 3–34.

[91] Pressley A N. Elementary differential geometry [M]. Springer Science & Business Media, 2010.

[92] Lawrence S. Developable surfaces: their history and application [J]. Nexus Network Journal, 2011, 13 (3): 701–714.

[93] MacDonnell J. Ruled surfaces: The mathematics of three straight-line-generated constructions [J]. Leonardo, 1984, 17 (2): 104–107.

[94] Pottmann H, Wallner J. Computational line geometry [M]. Springer Science & Business Media, 2009.

[95] Dolgachev I V. Classical Algebraic Geometry: A Modern View [M]. Cambridge University Press, 2012.

[96] Bhooshan S. Interactive Design of Curved-Crease-Folding [D]. [S. l.]: University of Bath, 2016.

[97] Vergauwen A, Temmerman N D, Laet L D. Digital modelling of deployable structures based on curved-line folding [C]. In Proceedings of IASS Annual Symposia, 2014: 1–8.

[98] Mitani J. Column-shaped origami design based on mirror reflections [J]. Journal for Geometry and Graphics, 2012, 16 (2): 185–194.

[99] Chandra S, Körner A, Koronaki A, *et al*. Computing curved-folded tessellations through straight-folding approximation [C]. In Proceedings of the Symposium on Simulation for Architecture & Urban Design, 2015: 152–159.

[100] Demaine E D, Demaine M L, Huffman D A, *et al*. Conic Crease Patterns with Reflecting Rule Lines [J]. arXiv preprint arXiv:1812.01167, 2018.

[101] Weiss G, Furtner P. Computer-aided treatment of developable surfaces [J]. Computers & Graphics, 1988, 12 (1): 39–51.

[102] Liu Y, Pottmann H, Wallner J, *et al*. Geometric modeling with conical meshes and developable surfaces [C]. In ACM transactions on graphics (TOG), 2006: 681–689.

[103] Tang C, Bo P, Wallner J, *et al*. Interactive design of developable surfaces [J]. ACM Transactions on Graphics (TOG), 2016, 35 (2): 12.

[104] Lang R J, Nelson T, Magleby S, *et al*. Kinematics and Discretization of Curved-Fold Mechanisms [C]. In ASME 2017 International Design Engineering Technical Conferences and Computers and Information in Engineering Conference, 2017: V05BT08A042–V05BT08A042.

[105] Solomon J, Vouga E, Wardetzky M, *et al*. Flexible developable surfaces [C]. In Computer Graphics Forum, 2012: 1567–1576.

[106] Howell L L. Compliant mechanisms [M]. John Wiley & Sons, 2001.

[107] Howell L L, Magleby S P, Olsen B M. Handbook of compliant mechanisms [M]. John Wiley & Sons, 2013.

[108] Zhou X, Zang S, You Z. Origami mechanical metamaterials based on the Miura-derivative fold patterns [J]. Proc. R. Soc. A, 2016, 472 (2191): 20160361.

[109] Tolman S S, Magleby S P, Howell L L. Elastic Energy Absorption of Origami-Based Corrugations [C]. In ASME 2017 International Design Engineering Technical Conferences and Computers and Information in Engineering Conference, 2017: V05BT08A032–V05BT08A032.

[110] Tolman S S, Delimont I L, Howell L L, *et al*. Material selection for elastic energy absorption in origami-inspired compliant corrugations [J]. Smart Materials and Structures, 2014, 23 (9): 094010.

[111] Watanabe Y, Mitani J. Modelling the Folding Motions of a Curved Fold [C]. In Origami 7: Seventh International Meeting of Origami Science, Mathematics, and Education, 2018: 1135–1150.

[112] Euler L. Methodus inveniendi lineas curvas maxima minimive proprietate gaudentes Additamentum I [J]. De Curvis Elasticis, Lausanne and Geneva, 1774, 1744.

[113] Huddleston J V. Nonlinear buckling and snap-over of a two-member frame [J]. International Journal of Solids and Structures, 1967, 3 (6): 1023–1030.

[114] Horn B K. The curve of least energy [J]. ACM Transactions on Mathematical Software (TOMS), 1983, 9 (4): 441–460.

[115] Dym C L, Shames I H, *et al*. Solid mechanics [M]. Springer, 1973.

[116] Yang T. Matrix displacement solution to elastica problems of beams and frames [J]. International Journal of Solids and Structures, 1973, 9 (7): 829–842.

[117] Pacheco Q, Piña E. The elastic rod [J]. Revista mexicana de física E, 2007, 53 (2): 186–190.

[118] Valiente A. An experiment in nonlinear beam theory [J]. American journal of physics, 2004, 72 (8): 1008–1012.

[119] McElwain W. A script for elastic bending (aka the elastica curve) [J], 2014. `http://www.grasshopper3d.com/forum/topics/a-script-for-elastic-bending-aka-the-elastica-curve`.

[120] Byrd P F, Friedman M D. Handbook of Elliptic Integrals for Engineers and Physicists [M]. Springer, 2013.

[121] Taki T. Application of MS-Excel "Solver" to Non-linear Beam Analysis [J], 2007. `http://www.geocities.jp/toshimi_taki/structure/beam/beam.htm`.

[122] Edison C E. Compression and Rotational Limitations of Curved Corrugations [J]. Origami, 2011, 5: 69–79.

[123] Goss V G A. The history of the planar elastica: insights into mechanics and scientific method [J]. Science & Education, 2009, 18 (8): 1057–1082.

[124] Shield R, Im S. Small strain deformations of elastic beams and rods including large deflections [J]. Zeitschrift für angewandte Mathematik und Physik ZAMP, 1986, 37 (4): 491–513.

[125] González C, LLorca J. Stiffness of a curved beam subjected to axial load and large displacements [J]. International journal of solids and structures, 2005, 42 (5-6): 1537–1545.

[126] Du Bois P, Kolling S, Koesters M, *et al*. Material behaviour of polymers under impact loading [J]. International Journal of Impact Engineering, 2006, 32 (5): 725–740.

[127] Yue Y, Liu P, Zhang Z, *et al*. Approaching the theoretical elastic strain limit in copper nanowires [J]. Nano letters, 2011, 11 (8): 3151–3155.

[128] Wu F-F, Chan K, Jiang S-S, *et al*. Bulk metallic glass composite with good tensile ductility, high strength and large elastic strain limit [J]. Scientific reports, 2014, 4: 5302.

[129] Ma J, Yang X, Lee T-U J, *et al*. Elastic buckling control of cylindrical shells using origami patterns [J]. Bulletin of the American Physical Society, 2018.

[130] Yang X, Zang S, Ma J, *et al*. Elastic Buckling of Thin-walled Cylinders with Pre-embedded Diamond Patterns [C]. In Origami 7: 7th International Meeting on Origami in Science, Mathematics and Education, 2018.

[131] Gardner L, Nethercot D. Experiments on stainless steel hollow sections—Part 2: Member behaviour of columns and beams [J]. Journal of Constructional Steel Research, 2004, 60 (9): 1319–1332.

[132] Shaat A, Fam A. Axial loading tests on short and long hollow structural steel columns retrofitted using carbon fibre reinforced polymers [J]. Canadian Journal of Civil Engineering, 2006, 33 (4): 458–470.

[133] Khalilpasha H, Albermani F. Textured deep subsea pipelines [J]. International Journal of Mechanical Sciences, 2013, 68: 224–235.

[134] Karampour H, Albermani F. Experimental and numerical investigations of buckle interaction in subsea pipelines [J]. Engineering Structures, 2014, 66: 81–88.

[135] Airoldi A, Janszen G. A design solution for a crashworthy landing gear with a new trigger mechanism for the plastic collapse of metallic tubes [J], 2003.

[136] Krason W, Malachowski J. Effort analysis of the landing gear with possible flow during touchdown [J]. International Journal of Mechanics, 2008, 2: 16–23.

[137] Rusinek A, Zaera R, Forquin P, *et al*. Effect of plastic deformation and boundary conditions combined with elastic wave propagation on the collapse site of a crash box [J]. Thin-Walled Structures, 2008, 46 (10): 1143–1163.

[138] Bligh R, Arrington D, Sheikh N, *et al*. Low-Cost Median Barrier Gate [J]. Transportation Research Record: Journal of the Transportation Research Board, 2012 (2309): 105–113.

[139] Andrews K, England G, Ghani E. Classification of the axial collapse of cylindrical tubes under quasi-static loading [J]. International Journal of Mechanical Sciences, 1983, 25 (9-10): 687–696.

[140] Guillow S, Lu G, Grzebieta R. Quasi-static axial compression of thin-walled circular aluminium tubes [J]. International Journal of Mechanical Sciences, 2001, 43 (9): 2103–2123.

[141] Alhussainy F, Sheikh M N, Hadi M N. Behaviour of Small Diameter Steel Tubes Under Axial Compression [C]. In Structures, 2017: 155–163.

[142] Karagiozova D, Alves M. Transition from progressive buckling to global bending of circular shells under axial impact—-Part I: Experimental and numerical observations [J]. International Journal of Solids and Structures, 2004, 41 (5-6): 1565–1580.

[143] Teng J, Hu Y. Behaviour of FRP-jacketed circular steel tubes and cylindrical shells under axial compression [J]. Construction and Building Materials, 2007, 21 (4): 827–838.

[144] Bardi F, Yun H, Kyriakides S. On the axisymmetric progressive crushing of circular tubes under axial compression [J]. International Journal of Solids and Structures, 2003, 40 (12): 3137–3155.

[145] Allan T. Experimental and analytical investigation of the behaviour of cylindrical tubes subject to axial compressive forces [J]. Journal of Mechanical Engineering Science, 1968, 10 (2): 182–197.

[146] Xu X, Sun J, Lim C. An analytical symplecticity method for axial compression plastic buckling of cylindrical shells [J]. Journal of Pressure Vessel Technology, 2013, 135 (5): 051204.

[147] Calladine C. Understanding imperfection-sensitivity in the buckling of thin-walled shells [J]. Thin-Walled Structures, 1995, 23 (1-4): 215–235.

[148] Sun G, Xu F, Li G, *et al*. Crashing analysis and multiobjective optimization for thin-walled structures with functionally graded thickness [J]. International Journal of Impact Engineering, 2014, 64: 62–74.

[149] Zhang X, Zhang H, Wen Z. Axial crushing of tapered circular tubes with graded thickness [J]. International Journal of Mechanical Sciences, 2015, 92: 12–23.

[150] Lee S, Hahn C, Rhee M, *et al*. Effect of triggering on the energy absorption capacity of axially compressed aluminum tubes [J]. Materials & design, 1999, 20 (1): 31–40.

[151] Han H, Taheri F, Pegg N. Quasi-static and dynamic crushing behaviors of aluminum and steel tubes with a cutout [J]. Thin-walled structures, 2007, 45 (3): 283–300.

[152] Liu Z, Hao W, Qin Q. Buckling and energy absorption of novel pre-folded tubes under axial impacts [J]. Applied Physics A, 2017, 123 (5): 351.

[153] Song J, Chen Y, Lu G. Axial crushing of thin-walled structures with origami patterns [J]. Thin-Walled Structures, 2012, 54: 65–71.

[154] Cai J, Deng X, Feng J, *et al*. Geometric design and mechanical behavior of a deployable cylinder with Miura origami [J]. Smart Materials and Structures, 2015, 24 (12): 125031.

[155] Yang K. Design optimization of energy absorption structures with origami patterns [J], 2018.

[156] Ma J. Thin-walled tubes with pre-folded origami patterns as energy absorption devices [D]. [S. l.]: University of Oxford, 2011.

[157] Timoshenko S P, Woinowsky-Krieger S. Theory of plates and shells [M]. McGraw-hill, 1959.

[158] Yoshiaki G, Tomoo Y, Makoto O. Elliptic integral solutions of plane elastica with axial and shear deformations [J]. International Journal of Solids and Structures, 1990, 26 (4): 375–390.

[159] Lee B K, Wilson J F, Oh S J. Elastica of cantilevered beams with variable cross sections [J/OL]. International Journal of Non-Linear Mechanics, 1993, 28 (5): 579 – 589. http://www.sciencedirect.com/science/article/pii/002074629390049Q.

[160] Lee B K, Oh S-J. Elastica and buckling load of simple tapered columns with constant volume [J]. International Journal of Solids and Structures, 2000, 37 (18): 2507–2518.

[161] Rodriguez-Uicab O, May-Pat A, Aviles F, *et al*. Influence of processing method on the mechanical and electrical properties of MWCNT/PET composites [J]. Journal of Materials, 2013, 2013.

[162] Schein M. Applied Generative Procedures in Furniture Design [C]. In Proceedings of the Generative Art International Conference, 2002: 21–1.

[163] Sternberg S. Curves and Flats [C]. In 4th International Meeting of Origami. Natick, AK Peters Ltd, Robert J. Lang Editor, 2009.

[164] Schmidt P, Stattmann N. Unfolded: paper in design, art, architecture and industry [M]. Walter de Gruyter, 2012.

[165] Zhakypov Z, Paik J. Design methodology for constructing multimaterial origami robots and machines [J]. IEEE Transactions on Robotics, 2018, 34 (1): 151–165.

[166] Gauss K F, Pesic P. General investigations of curved surfaces [M]. Courier Corporation, 2005.

[167] McPharlin P. Paper sculpture: its construction & uses for display & decoration [M]. Marquardt, incorporated, 1944.

[168] Gattas J M. Quasi-static impact of foldcore sandwich panels [D]. [S. l.]: Oxford University, UK, 2013.

[169] Nangreave J, Han D, Liu Y, *et al*. DNA origami: a history and current perspective [J]. Current opinion in chemical biology, 2010, 14 (5): 608–615.

[170] Shigemune H, Maeda S, Hara Y, *et al*. Origami robot: A self-folding paper robot with an electrothermal actuator created by printing [J]. IEEE/ASME Transactions on Mechatronics, 2016, 21 (6): 2746–2754.

[171] Gattas J M, You Z. Geometric assembly of rigid-foldable morphing sandwich structures [J]. Engineering Structures, 2015, 94: 149–159.

[172] Mueller S, Kruck B, Baudisch P. LaserOrigami: laser-cutting 3D objects [C]. In Proceedings of the SIGCHI Conference on Human Factors in Computing Systems, 2013: 2585–2592.

[173] Lang R J. The science of origami [J]. Physics world, 2007, 20 (2): 30.

[174] Peraza-Hernandez E A, Hartl D J, Malak Jr R J, *et al*. Origami-inspired active structures: a synthesis and review [J]. Smart Materials and Structures, 2014, 23 (9): 094001.

[175] Lee T-U, Yang X, Ma J, *et al*. Elastic buckling shape control of thin-walled cylinder using pre-embedded curved-crease origami patterns [J]. International Journal of Mechanical Sciences, 2019, 151: 322–330.

[176] Tornabell P, Soriano E, Sastre R. Pliable structures with rigid couplings for parallel leaf-springs–Pliable timber torus pavilion [C]. In Mobile and rapidly assembled structures IV:[Fourth International Conference on Mobile and Rapid Assembly Structures, MARAS 2014, which took place in Ostend], 2014: 117–128.

[177] Nabaei S, Baverel O, Weinand Y. Form finding of twisted interlaced structures: a hybrid approach [M] // Nabaei S, Baverel O, Weinand Y. Advances in Architectural Geometry 2014. Springer, 2015: 2015: 127–143.

[178] Miyashita S, Onal C D, Rus D. Self-pop-up cylindrical structure by global heating [C]. In 2013 IEEE/RSJ International Conference on Intelligent Robots and Systems, 2013: 4065–4071.

[179] Whitney J, Sreetharan P, Ma K, *et al*. Pop-up book MEMS [J]. Journal of Micromechanics and Microengineering, 2011, 21 (11): 115021.

[180] Jacobsen J O, Winder B G, Howell L L, *et al*. Lamina emergent mechanisms and their basic elements [J]. Journal of Mechanisms and Robotics, 2010, 2 (1): 011003.

[181] Gafford J, Kesner S, Wood R, *et al*. Microsurgical devices by pop-up book mems [J]. ASME/IDETC: Robotics and Mechanisms in Medicine, 2013.

[182] Gollnick P S, Magleby S P, Howell L L. An introduction to multilayer lamina emergent mechanisms [J]. Journal of Mechanical Design, 2011, 133 (8): 081006.

[183] Zhang Z, Ma W, Wu H, *et al*. A rigid thick Miura-Ori structure driven by bistable carbon fibre-reinforced polymer cylindrical shell [J]. Composites Science and Technology, 2018, 167: 411–420.

[184] Greenberg H. The Application of Origami to the Design of Lamina Emergent Mechanisms (LEMs) with Extensions to Collapsible, Compliant and Flat-Folding Mechanisms [J], 2012.

[185] Wei G, Dai J S. Origami-inspired integrated planar-spherical overconstrained mechanisms [J]. Journal of Mechanical Design, 2014, 136 (5): 051003.

[186] Ge Q, Dunn C K, Qi H J, *et al*. Active origami by 4D printing [J]. Smart Materials and Structures, 2014, 23 (9): 094007.

[187] Gattas J, You Z. Design and digital fabrication of folded sandwich structures [J]. Automation in Construction, 2016, 63: 79–87.

[188] Tolley M T, Felton S M, Miyashita S, *et al*. Self-folding origami: shape memory composites activated by uniform heating [J]. Smart Materials and Structures, 2014, 23 (9): 094006.

[189] Martínez-Martín F, Thrall A. Honeycomb core sandwich panels for origami-inspired deployable shelters: multi-objective optimization for minimum weight and maximum energy efficiency [J]. Engineering Structures, 2014, 69: 158–167.

[190] Nojima T, Saito K. Development of newly designed ultra-light core structures [J]. JSME International Journal Series A Solid Mechanics and Material Engineering, 2006, 49 (1): 38–42.

[191] Debnath S, Fei L. Origami theory and its applications: A literature review [J]. World Academy of Science, Engineering and Technology, 2013: 1131–1135.

[192] Jianguo C, Xiaowei D, Ya Z, *et al*. Bistable behavior of the cylindrical origami structure with Kresling pattern [J]. Journal of Mechanical Design, 2015, 137 (6): 061406.

[193] Zhao X, Hu Y, Hagiwara I. Shape optimization to improve energy absorption ability of cylindrical thin-walled origami structure [J]. Journal of Computational Science and Technology, 2011, 5 (3): 148–162.

[194] Ma J, You Z. Energy absorption of thin-walled square tubes with a prefolded origami pattern—part I: geometry and numerical simulation [J]. Journal of Applied Mechanics, 2014, 81 (1): 011003.

[195] Onal C D, Wood R J, Rus D. An origami-inspired approach to worm robots [J]. IEEE/ASME Transactions on Mechatronics, 2013, 18 (2): 430–438.

[196] Miyashita S, Guitron S, Ludersdorfer M, *et al*. An untethered miniature origami robot that self-folds, walks, swims, and degrades [C]. In Robotics and Automation (ICRA), 2015 IEEE International Conference on, 2015: 1490–1496.

[197] Vander Hoff E, Jeong D, Lee K. OrigamiBot-I: A thread-actuated origami robot for manipulation and locomotion [C]. In Intelligent Robots and Systems (IROS 2014), 2014 IEEE/RSJ International Conference on, 2014: 1421–1426.

[198] Zirbel S A, Trease B P, Thomson M W, *et al*. HanaFlex: a large solar array for space applications [C]. In Micro-and Nanotechnology Sensors, Systems, and Applications VII, 2015: 94671C.

[199] Zirbel S A, Trease B P, Magleby S P, *et al*. Deployment methods for an origami-inspired rigid-foldable array [J], 2014.

[200] Zirbel S A, Wilson M E, Magleby S P, *et al*. An origami-inspired self-deployable array [C]. In ASME 2013 Conference on Smart Materials, Adaptive Structures and Intelligent Systems, 2013: V001T01A026–V001T01A026.

[201] Ge L, Wang S, Song X, *et al*. 3D Origami-based multifunction-integrated immunodevice: low-cost and multiplexed sandwich chemiluminescence immunoassay on microfluidic paper-based analytical device [J]. Lab on a Chip, 2012, 12 (17): 3150–3158.

[202] Cai J, Deng X, Xu Y, *et al*. Geometry and motion analysis of origami-based deployable shelter structures [J]. Journal of Structural Engineering, 2015, 141 (10): 06015001.

[203] Kuijvenhoven M. A design method for timber grid shells [J]. Delft University of Technology, 2009.

[204] Harding J, Pearson W, Lewis H, *et al*. The ongreening pavilion [M] // Harding J, Pearson W, Lewis H, *et al*. Advances in architectural geometry 2014. Springer, 2015: 2015: 295–308.

[205] Levien R L. From spiral to spline: Optimal techniques in interactive curve design [D]. [S. l.]: UC Berkeley, 2009.

[206] Baek C, Sageman-Furnas A O, Jawed M K, *et al*. Form finding in elastic gridshells [J]. Proceedings of the National Academy of Sciences, 2018, 115 (1): 75–80.

[207] Guang C, Yang Y. Single-Vertex Multicrease Rigid Origami With Nonzero Thickness and Its Transformation Into Deployable Mechanisms [J]. Journal of Mechanisms and Robotics, 2018, 10 (1): 011010.

[208] Kunori T, Geil P. Morphology-property relationships in polycarbonate-based blends. I. Modulus [J]. Journal of Macromolecular Science, Part B: Physics, 1980, 18 (1): 93–134.

[209] Sterman Y, Demaine E, Oxman N. PCB origami: A material-based design approach to computer-aided foldable electronic devices [J]. Journal of Mechanical Design, 2013, 135 (11): 114502.

[210] Hawkes E, An B, Benbernou N, *et al*. Programmable matter by folding [J]. Proceedings of the National Academy of Sciences, 2010, 107 (28): 12441–12445.

[211] Smith W, Dean R. Structural characteristics of fused deposition modeling polycarbonate material [J]. Polymer testing, 2013, 32 (8): 1306–1312.

[212] Lee T, You Z, Gattas J. Elastica surface generation of curved-crease origami [J]. International Journal of Solids and Structures, 2017.

[213] Rogers J, Huang Y, Schmidt O, *et al*. Origami mems and nems [J]. Mrs Bulletin, 2016, 41 (2): 123–129.

[214] Paik J, Byoungkwon A, Rus D, *et al*. Robotic Origamis: Self-Morphing Modular Robot [C]. In ICMC, 2012.

[215] Sreetharan P, Whitney J, Strauss M, *et al*. Monolithic fabrication of millimeter-scale machines [J]. Journal of Micromechanics and Microengineering, 2012, 22 (5): 055027.

[216] Suzuki K, Shimoyama I, Miura H, *et al*. Creation of an insect-based microrobot with an external skeleton and elastic joints [C]. In Micro Electro Mechanical Systems, 1992, MEMS'92, Proceedings. An Investigation of Micro Structures, Sensors, Actuators, Machines and Robot. IEEE, 1992: 190–195.

[217] Lee T, Gattas J. Experimental analysis of a reverse elastica pop-up geometry [C]. In 8th International Conference on Fibre-Reinforced Polymer (FRP) Composites in Civil Engineering (CICE 2016), 2016.

[218] Gattas J, O'Dwyer M, Heitzmann M, *et al*. Folded hybrid FRP-timber sections: concept, geometric design and experimental behaviour [J]. Thin-Walled Structures, 2018, 122: 182–192.

[219] Schenk M, Viquerat A, Seffen K, *et al*. Review of inflatable booms for deployable space structures: packing and rigidization [J]. Journal of Spacecraft and Rockets, 2014.

[220] Kim S, Lee D, Koh J, *et al*. Fast, compact, and lightweight shape-shifting system composed of distributed self-folding origami modules [C]. In Robotics and Automation (ICRA), 2016 IEEE International Conference on, 2016: 4969–4974.

[221] Saito K, Agnese F, Scarpa F. A cellular kirigami morphing wingbox concept [J]. Journal of intelligent material systems and structures, 2011, 22 (9): 935–944.

[222] Tachi T. Simulation of rigid origami [J]. Origami, 2009, 4: 175–187.

[223] Jianguo C, Yangqing L, Ruijun M, *et al*. Nonrigidly Foldability Analysis of Kresling Cylindrical Origami [J]. Journal of Mechanisms and Robotics, 2017, 9 (4): 041018.

[224] Schenk M, Guest S. Origami folding: A structural engineering approach [C]. In Origami 5: Fifth International Meeting of Origami Science, Mathematics, and Education, 2011: 291–304.

[225] Filipov E, Tachi T, Paulino G. Origami tubes assembled into stiff, yet reconfigurable structures and metamaterials [J]. Proceedings of the National Academy of Sciences, 2015, 112 (40): 12321–12326.

[226] Chen Y, Feng H, Ma J, *et al*. Symmetric waterbomb origami [C]. In Proc. R. Soc. A, 2016: 20150846.

[227] Liu S, Lv W, Chen Y, *et al*. Deployable Prismatic Structures With Rigid Origami Patterns [J]. Journal of Mechanisms and Robotics, 2016, 8 (3): 031002.

[228] Lee T-U, Chen Y, Gattas J M. Curved-Crease Origami with Multiple States [C]. In Origami 7: Seventh International Meeting of Origami Science, Mathematics, and Education, 2018: 0.

[229] Gattas J M, Baber K, Al-Qaryouti Y, *et al*. Rapid Assembly with Bending-Stabilised Structures [C]. In Fabricate 2017, 2017: 50–57.

[230] Kilian M, Flöry S, Chen Z, *et al*. Developable surfaces with curved creases [J]. Proc. AAG, 2008: 33–36.

[231] Guégan P, Lebreton D, Pasco F, *et al*. Metallic energy-absorbing inserts for Formula One tyre barriers [J]. Proceedings of the Institution of Mechanical Engineers, Part D: Journal of Automobile Engineering, 2008, 222 (5): 699–704.

[232] Alghamdi A. Collapsible impact energy absorbers: an overview [J]. Thin-walled structures, 2001, 39 (2): 189–213.

[233] de Vries J. Research on the Yoshimura buckling pattern of small cylindrical thin walled shells [C]. In Spacecraft Structures, Materials and Mechanical Testing 2005, 2005.

[234] Fan Z, Lu G, Liu K. Quasi-static axial compression of thin-walled tubes with different cross-sectional shapes [J]. Engineering Structures, 2013, 55: 80–89.

[235] Najafi A, Rais-Rohani M. Mechanics of axial plastic collapse in multi-cell, multi-corner crush tubes [J]. Thin-Walled Structures, 2011, 49 (1): 1–12.

[236] Guest S, Kebadze E, Pellegrino S. A zero-stiffness elastic shell structure [J]. Journal of Mechanics of Materials and Structures, 2011, 6 (1): 203–212.

[237] Guest S, Pellegrino S. Analytical models for bistable cylindrical shells [C]. In Proceedings of the Royal Society of London A: Mathematical, Physical and Engineering Sciences, 2006: 839–854.

[238] Wang B, Zhou C. The imperfection-sensitivity of origami crash boxes [J]. International Journal of Mechanical Sciences, 2017, 121: 58–66.

[239] Abramowicz W, Wierzbicki T. Axial crushing of foam-filled columns [J]. International Journal of Mechanical Sciences, 1988, 30 (3-4): 263–271.

[240] Salehghaffari S, Tajdari M, Panahi M, *et al*. Attempts to improve energy absorption characteristics of circular metal tubes subjected to axial loading [J]. Thin-Walled Structures, 2010, 48 (6): 379–390.

[241] Foster C. Some observations on the Yoshimura buckle pattern for thin-walled cylinders [J]. Journal of Applied Mechanics, 1979, 46 (2): 377–380.

[242] Singace A A. Axial crushing analysis of tubes deforming in the multi-lobe mode [J]. International Journal of Mechanical Sciences, 1999, 41 (7): 865–890.

[243] Robertson A. The strength of tubular struts [J]. Proc. R. Soc. Lond. A, 1928, 121 (788): 558–585.

[244] Grzebieta R. An alternative method for determining the behaviour of round stocky tubes subjected to an axial crush load [J]. Thin-walled structures, 1990, 9 (1-4): 61–89.

[245] Karagiozova D, Alves M. Transition from progressive buckling to global bending of circular shells under axial impact—-Part II: Theoretical analysis [J]. International journal of solids and structures, 2004, 41 (5-6): 1581–1604.

[246] Wierzbicki T, Abramowicz W. On the crushing mechanics of thin-walled structures [J]. Journal of Applied mechanics, 1983, 50 (4a): 727–734.

[247] Pugsley A. The large-scale crumpling of thin cylindrical columns [J]. The Quarterly Journal of Mechanics and Applied Mathematics, 1960, 13 (1): 1–9.

[248] Mallock H R A. Note on the instability of tubes subjected to end pressure, and on the folds in a flexible material [J]. Proc. R. Soc. Lond. A, 1908, 81 (549): 388–393.

[249] Alexander J. An approximate analysis of the collapse of thin cylindrical shells under axial loading [J]. The Quarterly Journal of Mechanics and Applied Mathematics, 1960, 13 (1): 10–15.

[250] Pugsley A G. On the crumpling of thin tubular struts [J]. The Quarterly Journal of Mechanics and Applied Mathematics, 1979, 32 (1): 1–7.

[251] Niezgodziński T, Kubiak T. The problem of stability of web sheets in box-girders of overhead cranes [J]. Thin-Walled Structures, 2005, 43 (12): 1913–1925.

[252] Wardenier J, Packer J, Zhao X, *et al*. Hollow sections in structural applications [M]. Bouwen met Staal Rotterdam,, The Netherlands, 2002.

[253] Kim H C, Shin D K, Lee J J, *et al*. Crashworthiness of aluminum/CFRP square hollow section beam under axial impact loading for crash box application [J]. Composite Structures, 2014, 112: 1–10.

[254] Rus D, Tolley M T. Design, fabrication and control of soft robots [J]. Nature, 2015, 521 (7553): 467.

[255] Polak M, Winter J, Schnabel U, *et al*. Innovative Plasma Generation in Flexible Biopsy Channels for Inner-Tube Decontamination and Medical Applications [J]. Plasma Processes and Polymers, 2012, 9 (1): 67–76.

[256] De Greef A, Lambert P, Delchambre A. Towards flexible medical instruments: Review of flexible fluidic actuators [J]. Precision engineering, 2009, 33 (4): 311–321.

[257] Martinez R V, Branch J L, Fish C R, *et al*. Robotic tentacles with three-dimensional mobility based on flexible elastomers [J]. Advanced materials, 2013, 25 (2): 205–212.

[258] Grotberg J B, Jensen O E. Biofluid mechanics in flexible tubes [J]. Annual review of fluid mechanics, 2004, 36.

[259] Lee T-U, You Z, Gattas J M. Elastica surface generation of curved-crease origami [J]. International Journal of Solids and Structures, 2018, 136: 13–27.

[260] Lang R. Tessellations and twists. 2001.

[261] Mackenzie I. A Strain Energy Function for Large Deformations of Curved Beams [D]. [S. l.]: University of Waterloo, 2008.

[262] Ghuku S, Saha K N. A theoretical and experimental study on geometric nonlinearity of initially curved cantilever beams [J]. Engineering Science and Technology, an International Journal, 2016, 19 (1): 135–146.

[263] Klett Y. Plastically Annealed Lamina Emergent Origami [C]. In ASME 2018 International Design Engineering Technical Conferences and Computers and Information in Engineering Conference, 2018.

[264] Delimont I L, Magleby S P, Howell L L. Evaluating compliant hinge geometries for origami-inspired mechanisms [J]. Journal of Mechanisms and Robotics, 2015, 7 (1): 011009.

[265] Koh J-s, Kim S-r, Cho K-j. Self-folding origami using torsion shape memory alloy wire actuators [C]. In ASME 2014 International Design Engineering Technical Conferences and Computers and Information in Engineering Conference, 2014: V05BT08A043–V05BT08A043.

[266] Li S, Wang K. Fluidic origami with embedded pressure dependent multi-stability: a plant inspired innovation [J]. Journal of The Royal Society Interface, 2015, 12 (111): 20150639.

[267] Yasuda H, Yang J. Reentrant origami-based metamaterials with negative Poisson’s ratio and bistability [J]. Physical review letters, 2015, 114 (18): 185502.

[268] Tachi T. Generalization of rigid foldable quadrilateral mesh origami [C]. In Symposium of the International Association for Shell and Spatial Structures (50th. 2009. Valencia). Evolution and Trends in Design, Analysis and Construction of Shell and Spatial Structures: Proceedings, 2009.

[269] Dudte L H, Vouga E, Tachi T, *et al*. Programming curvature using origami tessellations [J]. Nature materials, 2016, 15 (5): 583.

[270] Baek S-M, Lee D-Y, Cho K-J. Curved Compliant Facet Origami-Based Self-Deployable Gliding Wing Module for Jump-Gliding [C]. In ASME 2016 International Design Engineering Technical Conferences and Computers and Information in Engineering Conference, 2016: V05BT07A028–V05BT07A028.

[271] Wilding S E, Howell L L, Magleby S P. Introduction of planar compliant joints designed for combined bending and axial loading conditions in lamina emergent mechanisms [J]. Mechanism and Machine Theory, 2012, 56: 1–15.

[272] Greenberg H, Gong M L, Magleby S P, *et al*. Identifying links between origami and compliant mechanisms [J]. Mechanical Sciences, 2011, 2 (2): 217–225.

[273] Sofla A, Meguid S, Tan K, *et al*. Shape morphing of aircraft wing: Status and challenges [J]. Materials & Design, 2010, 31 (3): 1284–1292.

[274] Ramrakhyani D S, Lesieutre G A, Frecker M I, *et al*. Aircraft structural morphing using tendon-actuated compliant cellular trusses [J]. Journal of aircraft, 2005, 42 (6): 1614–1620.

[275] Conway N J, Traina Z J, Kim S-G. A strain amplifying piezoelectric MEMS actuator [J]. Journal of Micromechanics and Microengineering, 2007, 17 (4): 781.

[276] Okada M, Ban S, Nakamura Y. Skill of compliance with controlled charging/discharging of kinetic energy [C]. In Robotics and Automation, 2002. Proceedings. ICRA’02. IEEE International Conference on, 2002: 2455–2460.

[277] Kota S, Lu K-J, Kreiner Z, *et al*. Design and application of compliant mechanisms for surgical tools [J]. Journal of biomechanical engineering, 2005, 127 (6): 981–989.

[278] Kota S, Joo J, Li Z, *et al*. Design of compliant mechanisms: applications to MEMS [J]. Analog integrated circuits and signal processing, 2001, 29 (1-2): 7–15.

[279] Lu K-J, Kota S. Design of compliant mechanisms for morphing structural shapes [J]. Journal of intelligent material systems and structures, 2003, 14 (6): 379–391.

[280] Culpepper M L, Anderson G. Design of a low-cost nano-manipulator which utilizes a monolithic, spatial compliant mechanism [J]. Precision engineering, 2004, 28 (4): 469–482.

[281] Hernandez E A P, Hartl D J, Akleman E, *et al*. Modeling and analysis of origami structures with smooth folds [J]. Computer-Aided Design, 2016, 78: 93–106.

[282] Secheli G, Viquerat A, Aglietti G S. A Model of Packaging Folds in Thin Metal-Polymer Laminates [J]. Journal of Applied Mechanics, 2017, 84 (10): 101005.

[283] Kergosien Y L, Gotoda H, Kunii T L. Bending and creasing virtual paper [J]. IEEE Computer graphics and applications, 1994, 14 (1): 40–48.

[284] Kuijvenhoven M, Hoogenboom P. Particle-spring method for form finding grid shell structures consisting of flexible members [J]. Journal of the International Association for Shell and Spatial Structures, 53 (1), 2012, 2012.

[285] Vouga E. Discrete Differential Geometry of Thin Materials for Computational Mechanics [D]. [S. l.]: Columbia University, 2013.

[286] Hernandez E A P, Hartl D J, Lagoudas D C. Kinematics of Origami Structures With Smooth Folds [J]. Journal of Mechanisms and Robotics, 2016, 8 (6): 061019.

[287] Shen Z, Huang J, Chen W, *et al*. Geometrically Exact Simulation of Inextensible Ribbon [C]. In Computer Graphics Forum, 2015: 145–154.

[288] Hwang H-D, Yoon S-H. Constructing developable surfaces by wrapping cones and cylinders [J]. Computer-Aided Design, 2015, 58: 230–235.

[289] Feynman R, Leighton R. The Feynman Lectures on Physics, Vol. 2 [J], 1964.

中文大摘要

折纸是一项中国的传统艺术，其能够将平面材料通过折叠转换成三维结构。近年来折纸结构由于其特殊的形状和力学性能，得到了土木工程、生物医学工程、航空航天工程、机械工程、材料科学和建筑设计等各领域研究人员的广泛关注。

曲线折痕折纸是一种特殊类型的折纸，其使用曲线折痕图案通过非刚性折叠使平面材料折叠成不同的三维结构；由于曲痕折纸具有特殊的美学价值，其经常被用于装饰或艺术品组件上，如产品包装和雕塑等；由于具有特殊的结构以及力学性能，其在工程和建筑领域中也有广泛的应用，如柔顺机构、抗冲击设备、自折叠设备和薄壁建筑结构等。人们对曲痕折纸的研究工作主要集中在精确地模拟曲痕折纸的折叠形式上。然而在这项工作中存在较大的困难，即在进行曲痕折纸的模拟时，需要保持其表面的零高斯曲率以确保其可展开性(即是否能够展开成一个平面)，以及需要考虑折纸结构表面的弯曲响应。

一方面，现有的许多静态曲痕折纸的设计是通过数学分析、几何建模、数值模拟等方法完成的。在使用这些技术进行曲痕折纸的设计时，存在一系列的限制性因素。例如，通过数学分析计算虽然能够简单且快速的生成曲痕折纸图案，然而人们使用该方法时并不会考虑材料的弹性或塑性弯曲能量，因此得到的结果会与实际物理模型产生表面误差。在其他建模方法中，通常需要对目标曲面进行离散化处理，通过许多离散的平面来近似拟合曲面，虽然这样可以通过结构的最小的弯曲能量来近似拟合曲面，但是其在计算和运行上十分复杂并且从未有人对这些方法进行过验证，因此，方法的准确性目前尚不确定。因此精确模拟曲痕折纸对于研究人员来说依然是一个巨大的挑战，并且亟需开发一种新的建模方法以便简洁且准确地描述曲痕折纸表面的弯曲响应以及判定其是否平面可展。

另一方面，关于曲痕折纸的折叠运动变形的研究也有待开展。曲痕折纸之所以可以被应用于柔顺机构中，是因为它们具有相似的特性，即都可以进行复杂的折叠运动变形并且具备存储应变能的能力。然而，目前关于曲痕折纸折叠运动变形的相关研究较少，主要原因是在折叠运动过程中，难以准确描述其表面的可展性和板材弯曲响应。现有的方法都是利用伪刚体法来模拟曲痕折纸的折叠运动，随后结合材料特性以描述其力学特性。然而，在这类方法中，并不考虑表面最小能量弯曲响应，而且这类方法都假设伪刚体是刚性可折叠的，因此，曲痕折纸的实际运动，如材料弯曲与可展性约束之间的相互作用等，还有待进一步研究，以便验证伪刚体法的假设及准确性。

本文旨在通过探索曲痕折纸的几何形状和大弹性弯曲力学的关系，以材料最小能量弯曲响应作为基础，提出一种新的曲痕折纸设计方法。文章提出一维弹性曲线可以为曲痕折纸的设计提供更好的解决方案，通过考虑材料弹性弯曲能量响应和折纸可展性约束之间的相互作用，使用弹性曲线作为曲痕折纸结构表面的非零主曲率，得到了一系列曲痕折纸图案，并且系统性的研究了弹性弯曲曲痕折纸的设计和

应用。本文包含六章内容，下面对本文中所进行的研究的主要内容进行简单描述：

- **第一章：研究背景概述**
- **第二章：文献综述**

本文第二章通过概述关领域的研究来阐明本文的研究目的。此外，本章也简要概述了弹性曲线的相关理论：弹性曲线描述了细长梁处于最小弯曲能量状态时中心线的几何形状，从数学模型中可验证，弹性曲线的表达式与材料的属性无关，因此具有相同形状的不同弹性材料制成的细长梁的弹性曲线相同。

- **第三章：曲痕折纸的弹性表面生成法**

本文第三章首先对弹性曲线理论进行了扩展，本章提出弹性曲线可以作为特定类型的三维表面的主曲率，基于这个理论，遵循最小弯曲弹性能量原理，可以得到设计曲痕折纸结构的新方法，此方法被命名为曲痕折纸的弹性曲面生成法。弹性曲线沿着某一方向进行扫掠可以形成一个各向同性的三维曲面（即弹性曲面），其既可以平面展开又具有最小的弯曲能量，在扫掠的过程中使用镜像的方式可以获得简单的曲痕折纸。如果镜像得到的曲面具有与原始曲面相同的曲率，则生成的三维曲痕折纸既可平面展开又具有最小弯曲能量。如果将刚性折纸结构作为基础进行连续弹性曲线投射及镜像，则可以得到与原有刚性折纸图案的形状和体积相似的复杂曲痕折纸图案。为了验证这种方法的准确性，我们制作了一系列的实物模型，并通过三维扫描对其表面进行了测量，对于简单的曲痕折纸（单折痕反射型）来说，如果使用弹性曲线作为表面的主曲率，理论解与实物模型（厚度为2 mm）之间的表面误差小于实物模型厚度的50%（可视为高精度设计），这也证明了弹性表面并不会因为镜像而改变其最小能量弯曲响应。但是如果使用圆弧作为折纸结构表面的主曲率，实物模型与理论解之间则会产生明显的表面误差，并且可观察到部分区域产生了类似于弹性曲线的表面变形以达到其最小弯曲能量状态。对于更复杂的曲痕折纸（如弧形管状曲痕折纸图案），测量结果显示，不同的弹性曲线都可应用于高精度的表面设计，所有模型与理论解的表面误差均小于实物模型材料厚度的一半。此外，我们还发现曲痕折纸图案还具有稳定的二阶或更高阶模式的弹性曲面，这意味着高阶弹性曲线也可以作为曲痕折纸的主曲率，并且根据研究，镜像法可以使高阶的弹性曲面变得稳定。

弹性弯曲响应在特殊曲痕折纸图案中会因自由边缘效应而失真。本章还对一系列的曲痕折纸图案进行了探索，我们发现，如果曲痕折纸图案具有矩形边界，则不会发生上述失真现象；如果曲痕折纸图案具有由矩形边界转换而来的自由边界，则会发生局部失真；如果折纸图案的自由边界无法由矩形转化而成，则会发生整体失真。总之，本章中所提出的曲痕折纸建模方法虽然仅能应用于特定类型的折纸图案，但是能够精确地描述曲痕折纸的弹性弯曲响应。

- **第四章：曲痕折纸折叠过程中的力学分析**

本文第四章首先分析了曲痕折纸结构在折叠运动中的能量响应。文中假设其最低弯曲能量响应与相同材料制成的非折叠曲面相同（二者具有相同的非零主曲率、弯曲刚度和面积），我们使用非折叠曲面的二维横截面作为曲痕折纸表面的简化表示，并通过该曲率在初始状态和变形状态之间的变化来计算曲面在折叠运动中所储存的弯曲应变能；而曲痕折纸结构的最高弯曲能量响应则与其对应的伪刚体(PRBM)的能量响应相同，因此我们可以通过伪刚体在具有可展约束下的运动过程中的面角变化来计算曲面所储存的弯曲应变能。我们使用了具有均匀表面曲率的

弧面曲痕折纸图案（非弹性曲面）对上述方法进行了实验验证，可以观察到实物模型的实际能量响应确实位于最低以及最高能量响应之间，该实验可以证明通过添加曲线折痕可以导致非弹性曲面曲痕折纸结构的能量响应偏离原本的最小能量状态。对于弹性曲面曲痕折纸来说，其在折叠运动过程中的最低和最高弯曲能量响应是相似的，弹性曲面折纸的折痕对其折展运动过程中的表面最小弯曲能量只具有极小的影响，因此我们可以对弹性曲面曲痕折纸结构的实际能量响应进行精准的预测。

对于柔顺机构来说，沿着加载方向的整体力学性能通常比在横截面变形方向上测量的能量更有参考价值，柔顺机构的整体力学性能与其局部横截面在折叠过程中的弯曲响应相关，本章提出了一种曲线折痕弯曲转换（CCBT）法，在表面最小能量响应不失真的状况下，可将局部能量－位移响应转换为整体能量－位移响应，然后转换为整体力－位移响应。我们使用了弹性曲面折纸对上述方法进行了验证，理论解与实物模型以及数值模拟在整体力－位移响应方面都有较好的吻合。然而，当局部横截面接近于直线时，上述理论解与实物模型和数值模拟之间会产生误差，该误差的产生的主要原因是由于自由边缘效应所引起的折痕区域周围的应力集中。由于曲痕折纸的折叠过程已大致得到了精准的预测，因此本文中未对此误差进行详细研究，并且，根据CCBT法，我们可以对具有不同几何参数的曲痕折纸图案，进行整体力－位移响应的预测。

本章中，我们通过对不同几何参数的弹性表面折纸进行研究，还得到了一系列有意义的发现。首先，折纸边缘角的大小可以确定整体力－位移响应的类型，当角度大于、等于和小于90度时，则分别产生硬化、塑性和软化的响应。其次，折纸边缘的长度可以确定整体力－位移响应的周期，即周期长度随着边缘长度的增加而增加。最后，我们通过不同的排列方式，得到了可以实现串联、并联或串并联组合的非线性机械弹簧功能的曲痕折纸图案。综上所述，我们可以通过调节弹性表面折纸的几何参数，得到所需的整体力－位移响应。

- **第五章：基于高阶弹性曲面的薄壁圆筒失效模式的研究**

本文第五章介绍了一种新的薄壁管状结构屈曲形状控制技术，利用高阶弹性曲线作为曲痕折纸的非零主曲率，可以生成出具有最小弯曲能量表面的薄壁管结构。折纸工程和大变形非线性力学的研究存在一个交集，即薄壁管的屈曲响应研究。在薄壁管的某些屈曲模式中可以自然形成一些折纸图案，并且管的压缩屈曲响应可以通过折纸图案（直线折痕折纸和曲线折痕折纸）来控制。在薄壁管的局部屈曲中存在两种显著的失效模式，分别是管壁较厚时的圆环模式，以及管壁较薄时的钻石模式，其中后者是一种自然形成的折纸结构，可以展开成由平面三角形组成的折纸图案。我们可以利用薄壁管对缺陷敏感的特性来控制它们的屈曲响应，最新的研究已经证明，直线痕折纸图案可以预嵌在薄壁管的表面上，以改变其弹性屈曲响应，并产生类似于钻石模式的后屈曲变形。然而由于使用这种方法产生的变形包含复杂的变形区域，因此其确切的形状是未知的。对于大多数屈曲变形来说，都存在上述问题，因此如何描述其确切的屈曲变形也是以往科研工作的一个难点。

本章中得到的薄壁管状结构屈曲变形之后的形状类似于薄壁圆柱自然的屈曲变形形状，即钻石模式。通过将管状结构展开成平面，我们可以得到其二维折纸图案，该图案可以再次通过折痕被压缩回折叠状态，或者简单地卷成薄壁圆柱体，其中后者可被视为具有预先嵌入曲痕折纸图案的圆柱体。因此上述薄壁管状结构存在两种三维稳定状态，即曲痕折纸状态和圆柱管状态。该研究的一项关键假设是薄壁管最

终的的曲痕折纸状态是其圆柱管状态在轴向压缩载荷下产生变形得到的。我们设计了一系列具有曲痕折纸图案的管状结构，并且将其与对应的具有直痕折纸图案的管状结构进行了测试和对比。测试结果根据后屈曲变形形状分为两种屈曲模式，即受控模式和不受控模式。具有受控模式图案的管状结构在被完全压缩至目标位置时，会形成类似钻石模式的变形。可以观察到，对于曲痕折纸图案管状结构及其对应的直痕折纸图案管状结构，如果具有相同的屈曲模式，那么二者的力－位移响应也是相似的。我们对包含受控模式折纸图案的管状结构进行了表面测量，发现曲痕折纸的实际变形与理论值的误差可以控制在材料厚度（0.3 mm）的50%以内，这不仅表示通过这种方法生成的薄壁管状结构具有较高的精确性，还验证了前面提到的关键假设，即薄壁管状结构的曲痕折纸状态是圆柱管状态在轴向压缩载荷下产生变形得到的。此外，直痕折纸的屈曲变形虽然无法被精确预测，但实验结果显示其在与理论值表面误差较低的区域具有类似于弹性曲面的特性。

最后，我们对受控模式的曲痕折纸行了深入分析。归类出三种具有不同类型力－位移响应的曲痕折纸，我们对其中具有典型屈曲非线性反应的折纸图案进行了进一步的研究，通过表面曲率的变化发现了包含受控模式曲痕折纸的管状结构的变形过程具有从应变能较高的圆柱管状态到应变能较低曲痕折纸状态的双稳态转变。

- **第六章：结论与展望**

本文通过采用弹性曲线理论对一系列的曲痕折纸图案进行了精确建模和分析。本论文的主要贡献为以下三点。(1) 通过用曲率表示表面弯曲响应的方式，提出了一种新的设计曲线折痕折纸的方法。通过这种方法，人们可以根据需要的体积以及折叠方式对曲痕折纸的折叠形状进行预设。(2) 在曲痕柔顺机构的设计中，建立了一种基于弹性曲线理论的弹性弯曲应变能可编程的力-位移理论模型。提出了一种在可展约束的前提下保持表面最小弯曲响应的新方法，实现了对曲痕折纸的柔性折叠运动的精确预测。(3) 提出了一种通过预先嵌入曲痕折纸图案来控制薄壁圆筒弹性屈曲形状的方法，实现了对薄壁圆柱体的弹性屈曲形状的精确控制。

曲痕折纸是一个相对较新的研究领域，相关领域的研究正在迅速发展。本论文为非线性大变形的精确地分析做出了重要贡献，但是在未来依然有许多工作有待开展。首先，本文仅利用特定的弹性曲线来构造各种曲痕折纸的表面，仍然存在一系列其他类型的弹性曲线，这些曲线也可以作为曲痕折纸表面的非零主曲率，从而进一步扩展曲痕折纸的设计范围。在未来的工作中我们需要进一步研究才能对这类曲线有更深入的了解。其次，本文提出的曲痕折纸创建方法建立在已知的直痕折纸图案的基础上，进而得到所需的镜像平面和弹性曲线几何参数。虽然直痕折纸图案类型众多且易于获取，但该方法基本上不适用于复杂的折纸工程设计。但是我们发现通过建立折痕图案参数和所需折纸图案的体积参数之间的明确关系，可以相对简单地先建立直线折痕折纸图案，然后转换成精确的弯曲折痕形式。参数化设计系统的结合是折纸设计中尚未开发的主题，也是我们未来需要研究的一项重要内容。第三，本文中研究薄壁管状结构时，只考虑了弹性变形阶段，如果薄壁管被进一步压缩，预嵌入的折痕线和生成的屈曲模式可能对随后管状结构的塑性变形产生一些影响，为此需要进一步研究整个屈曲过程，这可能会涉及到数值模拟方法的开发。此外该研究仅考虑了具有近似零转动刚度的预嵌入折痕，虽然可以使用更高刚度的折痕对结构的屈曲变形进行控制，但是这可能会影响结构的负载性能，这有待进一步的研究。最后，预嵌入技术不仅适用于圆柱形薄壁管，也可能应用于其他类型的薄

壁管状结构，例如具有多边形截面的管状结构，锥形的和具有不同长度的管状结构等。在设计中需要考虑不同的预定形状以达到最小弯曲能量状态。这是一个全新的折纸工程研究领域，在以后的工作中，我们可能会对该领域进行探索。

关键词：弹性曲线理论，曲痕折纸，柔顺机构，弹性弯曲应变能，屈曲形状控制，薄壁圆管

Publications during Candidature

Journal papers

- **Lee, T.U.** and Gattas, J.M., 2016. Geometric design and construction of structurally stabilized accordion shelters. Journal of Mechanisms and Robotics 8, no. 3 (2016): 031009.
- **Lee, T.U.**, You, Z. and Gattas, J.M., 2017. Elastica surface generation of curved-crease origami. International Journal of Solids and Structures, 136, pp.13-27.
- **Lee, T.U.**, Yang, X., Ma, J. Chen, Y. and Gattas, J.M., 2018. Elastic buckling control of thin-walled cylinder using pre-embedded curved-crease origami patterns. International Journal of Mechanical Sciences, 151, pp.322-330.
- **Lee, T.U.**, Chen, Y., Heitzmann, M.T. and Gattas, J.M., 2019. Minimum elastic bending behaviours of curved-crease origami. (Paper in preparation)

Book chapters

- Gattas, J.M., Baber, K., Al-Qaryouti, Y. and **Lee, T.U.**, 2017, January. Rapid Assembly with Bending-Stabilised Structures. In Fabricate 2017 (pp. 50-57). UCL Press.
- **Lee, T.U.**, Chen, Y. and Gattas, J.M., 2018. Curved-Crease Origami with Multiple States, In Origami 7: Seventh International Meeting of Origami Science, Mathematics, and Education, Vol. 3, 2018, pp. 849-864.

Conference papers

- **Lee, T.U.** and Gattas, J., 2016, January. Folded fabrication of composite curved-crease components. In International Conference on Fibre-Reinforced Polymer (FRP) Composites in Civil Engineering (pp. 1430-1435).
- **Lee, T.U.** and Gattas, J., 2016, January. Experimental analysis of a reverse elastica pop-up geometry. In International Conference on Fibre-Reinforced Polymer (FRP) Composites in Civil Engineering (pp. 1448-1453).

Conference abstracts

- Ma, J., Yang, X., **Lee, T. U.** and Chen, Y., 2018. Elastic buckling control of cylindrical shells using origami patterns. Bulletin of the American Physical Society.
- **Lee, T. U.** and Gattas, J., 2019. Elastic energy behaviours of curved-crease origami: a summary of recent progress. Engineering Mechanics Institute Conference.

Patents

- 马家耀、杨晓辰、**Ting-Uei Lee**、陈焱、杨富富，一种可展曲面管状结构，申请号：201810276778.3，发明专利，2018.3.31.

Acknowledgements

The financial support of this research was provided by the Australian Postgraduate Award (APA) and Research Higher Degree Scholarship from the University of Queensland. The projects described in this thesis were supported by the Australian Research Council Discovery Project DP160103279, and National Natural Science Foundation of China (project numbers 51825503, 51721003 and 51575377).

This thesis would not have been possible without the technical and mental support provided by my colleagues, friends, and family.

First of all, I would like to express my deepest sense of gratitude to my principal supervisor, Dr Joseph Gattas from the University of Queensland (UQ), whose guidance and advice has led my work into interesting areas and trained my professional skills to a world-class standard. He is not only a role model to me, but also a very important person who has completely changed my life.

Special thanks also go to my supervision team members who I closely working with: Professor Yan Chen from Tianjin University (TJU), Dr Michael Heitzmann (UQ), Dr Dilum Fernando (UQ), and Dr Jiayao Ma (TJU), for their social and academic interest and support. I would also like to thank my review panel members from UQ, Dr Cristian Maluk, and Dr Vinh Dao, for their valuable advices from various perspectives.

I would also like to thank, Mr John Milne, Mr Stewart Matthews, Mr Fraser Reid, Mr Jason Van Der Gevel, Mr Shane Walker, Mr Sam Butler, and Mr John Stafford, for their support in UQ laboratory and workshop. I am also extremely grateful to my research group members from UQ Folded Structures Lab: Ms Ya Ou, Mr Quan Shi, Miss Weiqu Cui, Mr Harry Mills, and Mr Yousef Alqaryouti, for their precious supports. I thank my fellow colleagues from TJU Motion Structure Lab: Mr Xiao Zhang, Miss Shixi Zang, Miss Mengyan Shi, Mr Mingyuan Yang, Miss Xiaoyi Jiang, Mr Yuanqing Gu, Mr Xuesong Chen, Miss Xiaochen Yang, Dr Fufu Yang (former), Dr Huijuan Feng (former), and Mr Jichao Song (former), for their support during my China visit. I would also like to thank my scholar friends from UQ, Dr Da Chen, Mr Kim Baber, Dr Helong Wu, Dr Hong Zhang, Dr Hao Zhou, Mr Peter Turner, Mr Der-Shen Yang, and Miss Ezgi Kaya, for their professional advices.

Finally, I would like to extend my gratitude to my parents, Mr Ming-Kun Lee and Ms Mei-Hua Tsao, brother Mr Harry Lee, and partner Miss Miao Zhang, who have all provided their love and encouragement. Without them, I could never have completed this doctoral degree. I dedicate this thesis to them, and I hope I make them all proud.

This is a UQ-TJU joint PhD thesis.

THE UNIVERSITY OF QUEENSLAND

AUSTRALIA

Elastic Energy Behaviours of Curved-crease Origami

Ting-Uei Lee

B.E.

A thesis submitted for the degree of Doctor of Philosophy at The University of Queensland in 2019

School of Civil Engineering